ELASTIC PROPERTIES OF POLYMERISED AND FLUID MEMBRANES UNDER STRESS

by

Julian Charles Shillcock

B.Sc. King's College London, 1982

M.Sc. Simon Fraser University, 1985

THESIS SUBMITTED IN PARTIAL FULFILLMENT OF

THE REQUIREMENTS FOR THE DEGREE OF

DOCTOR OF PHILOSOPHY

in the Department

of

Physics

Simon Fraser University

July 1995

APPROVAL

Name: Julian Charles Shillcock

Degree: Doctor of Philosophy

Title of Thesis: Elastic Properties of Polymerised and Fluid Membranes under Stress

Examining Committee: Prof. J. Dahn
Chair

Prof. David Boal
Senior Supervisor

Prof. Michael Plischke

Prof. Michael Wortis

Prof. Barbara Frisken
Internal Examiner

Prof. Béla Joós
External Examiner
Department of Physics
University of Ottawa, Ontario

Date Approved: 5 July 1995

PARTIAL COPYRIGHT LICENSE

I hereby grant to Simon Fraser University the right to lend my thesis, project or extended essay (the title of which is shown below) to users of the Simon Fraser University Library, and to make partial or single copies only for such users or in response to a request from the library of any other university, or other educational institution, on its own behalf or for one of its users. I further agree that permission for multiple copying of this work for scholarly purposes may be granted by me or the Dean of Graduate Studies. It is understood that copying or publication of this work for financial gain shall not be allowed without my written permission.

Title of Thesis/Project/Extended Essay

Elastic Properties of Polymerised and Fluid Membranes under Stress.

Author:_____
(signature)

_____
(name)

4-August-'95
(date)

ABSTRACT

The stability of a living cell relies on the properties and interrelations of its constituent parts. The fluid bilayer surrounding the cell separates the cytoplasm inside the cell from the extracellular environment. A cross-linked network of proteins within the cytoplasm supports the fluid bilayer and contributes to the cell's elasticity. Three properties relating to the behaviour of a model fluid bilayer and polymerised network are investigated by Monte Carlo simulation: the phase behaviour of a system of discotic liquid crystal molecules, the elastic properties of a model polymerised network, and the stability and rupture of a model fluid membrane.

The isotropic to nematic transition induced by hydrostatic pressure in a system of discotic liquid crystal molecules in three dimensions is presented. The study concentrates on the phase behaviour resulting from the anisotropy of the disks. The transition is present for disks whose thickness to radius ratio is less than 40%, but is absent for thicker disks. A more specialised model of disks restricted to intersect a planar interface between two immiscible fluids is investigated, but has no isotropic-nematic phase transition at finite temperature.

The elastic properties of a two-dimensional, triangulated network of Hookean springs are investigated as a function of temperature and applied tension. The compression modulus decreases, and the shear modulus increases, as the tension on the network is increased. The elastic properties of self-avoiding networks at low temperature are well described by a mean field theory. When the self-avoidance constraint is removed, the network undergoes a phase transition to a collapsed state of small area as the tension is reduced to zero. Both types of network show an unstable expansion of their area when the stretching tension exceeds a specified value. Both networks also have the unusual property

(referred to as a negative Poisson ratio) of expanding transversely when stretched longitudinally for a large range of applied tension.

The stability and rupture of a model fluid membrane at finite temperature is also investigated. The model membrane includes a single hole subject to a line tension, or energy cost per unit length of its perimeter. In the absence of applied pressure, thermal fluctuations are sufficient to rupture the membrane unless the line tension exceeds a minimum value. This value corresponds to 2.5×10^{-21} J/nm, and is an order of magnitude below some experimental estimates. Our results agree with a finite temperature calculation that predicts a transition from an unbroken membrane to a ruptured state at zero pressure. The transition is controlled by the branched polymer scaling behaviour of fluid membranes. At the transition, however, the hole scales as a closed self-avoiding walk. At positive pressure (i.e., compression) the hole scaling behaviour changes to that of a branched polymer. When the membrane is subject to a stretching pressure it becomes metastable to rupture. The free energy barrier height is found to be much smaller in finite temperature simulations than predicted by a zero temperature calculation. A phase diagram for the model membrane as a function of the line tension and pressure is presented.

I dedicate this work to my Father, who never saw me pass an examination, and to my Mother, who has seen them all.

I have of late, but wherefore I know not, lost all my mirth, forgone all custom of exercises; and indeed it goes so heavily with my disposition, that this goodly frame the earth seems to me a sterile promontory; this most excellent canopy the air, look you, this brave o'er-hanging firmament, this majestical roof fretted with golden fire, why it appeareth nothing to me but a foul and pestilent congregation of vapours. What a piece of work is a man! How noble in reason! How infinite in faculties! In form and moving how express and admirable! In action how like an angel! In apprehension, how like a god! The beauty of the world, the paragon of animals; and yet to me what is this quintessence of dust? Man delights not me.

Hamlet Prince of Denmark, Act 2, Scene 1. William Shakespeare.

ACKNOWLEDGEMENTS

I wish to thank first my supervisor David Boal for his insight and ideas, and generous donation of time and financial support that went into the work presented here. I also want to thank the Physics Department, and Simon Fraser University, for the financial support of Graduate Fellowships, the President's Research Stipend and Graduate Teaching Assistant award, as well as the more arduous, but rewarding, experience of being a teaching assistant. It has been a pleasure to work with students and faculty in the Physics Department, and I especially want to thank Sada Rangnekar for all his support throughout my time in the department. I am grateful to Jennifer C. Taylor for the faithful rendering of the computer images of model systems shown in Figs. 2.17, 2.18, 2.19, 4.1, 4.19, 5.3, 5.4 and 5.5.

Unfortunately there is not space enough to name all the friends and associates who have encouraged me during this degree, but I must mention Ms. Sandra Barsky, Ms. Sandi Millar and Ms. Alexandra Richmond *sine quem non*. Finally, I want to thank Mike Plischke, Zoltan Racz and Mike Wortis, for their guidance and patient explanations, and Margot Moore and Tom Richardson for their fascinating introduction to biology and physiology that may yet prove irresistibly alluring.

CONTENTS

LIST OF TABLES

LIST OF FIGURES

CHAPTER 1

INTRODUCTION

1.1 Overview of thesis

The cell is the basic unit of structure of all living things (Alberts et al., 1989). In recent years much attention has been directed towards trying to understand the basic physical properties of a cell. The red blood cell (RBC), the simplest cell in the human body, has proven to be a popular system for study (Bretscher, 1973; Leibler, 1989; Sackmann, 1990). It displays both simple and complex behaviour in response to changing external conditions, behaviour that is mediated by the exquisitely arranged structure of its surface and the underlying structural components that give the cell its stability.

The interactions between a cell's components can range over many different length and time scales. The RBC, for example, is surrounded by a plasma membrane (PM) composed of over 400 different kinds of lipid molecule. The lipids form a dense fluid bilayer held together by the repulsion of the lipids from the surrounding aqueous environment (Israelachvilli, 1992). The bilayer separates a cell's interior, called the cytoplasm, from the exterior, the extracellular space. Embedded in this fluid bilayer are proteins that mediate the cell's interactions with the outside world. Other transmembrane proteins connect the bilayer to structural components of the cell within the cytoplasm. On the cytoplasmic side of the bilayer is a crosslinked structure of filamentous proteins providing structural stability to the cell.

In the RBC this network is closely bound to the bilayer and forms an approximately hexagonally connected mesh. It is referred to as the membrane-associated cytoskeleton to distinguish it from the three-dimensional filamentous cytoskeleton that pervades the whole

cytoplasm in nucleated cells. The RBC cytoskeleton is attached to the bilayer by transmembrane proteins, and provides strength and shear resistance to the fluid membrane above it. The lipid molecules in the PM can diffuse freely in the plane of the bilayer but motion between the two monolayers in the PM (flip-flop) is approximately 10^{13} times slower (Alberts, 1989, p 278). The radius of the cell is about a factor of 10^3 times the size of a lipid molecule (ibid., p 275).

The lipid molecules that make up the PM contribute another level of structure to the cell. Lipids are derived from glycerol and contain two distinct parts. One part is a hydrophilic (water-loving) head group, that is usually polar, attached via a phosphate group to one carbon in the glycerol, and the other part consists of two long hydrophobic (water-hating) hydrocarbon tails attached to the two other carbons in the glycerol. The length of the hydrocarbon tails may vary but is usually between 14 and 24 carbon atoms long (Alberts et al., 1989, p 276). It is the hydrophobic repulsion of the hydrocarbon tails from water that causes the lipids to aggregate spontaneously in aqueous solution, while the repulsion between their headgroups contributes to the optimal membrane size. The repulsive forces between the head groups are complex and made up of several effects. In particular, steric repulsion, electrostatic and dispersion forces contribute (Israelachvilli, 1992, p 368).

Although the interactions between the individual parts of lipid molecules are complicated, experimental means have been found to separate several different structural components of a cell so that their functions can be individually analysed (Evans et al., 1976; Evans and Waugh, 1977). Other systems that are simpler than living cells have also been extensively studied in laboratories. These include vesicles extracted from the brush border of living cells (Miyamoto et al., 1988) and artificial vesicles (Evans and Needham, 1987; Evans and Rawicz, 1990; Rutkowski et al., 1991). The fluid bilayer of artificial

vesicles is generally composed of only one, or at most a few, types of lipids. This makes them more suitable than a living cell for analysis as a homogeneous membrane.

A wide range of properties of cells and vesicles has been analysed. These include shape transformations of vesicles (Kas and Sackmann, 1991), structural properties of vesicles (Sackmann, 1990) and the elastic properties of the cytoskeleton of RBCs (Evans et al., 1976; Evans and Waugh, 1977; Vertessy and Steck, 1989). The differences in the physics of these components of the cell can be illustrated by considering just two aspects: the fluid nature of the lipids in the PM, and the contribution of geometry to the behaviour of the PM and cytoskeleton.

The lipid molecules in the PM form a dense fluid. It is not an isotropic fluid however. The bilayer organisation of the PM restricts the motion of the hydrocarbon chains of the lipid molecules. The chains are constrained to lie nearly parallel to the bilayer normal. Such a phase of matter is an example of a liquid crystal (de Gennes and Prost, 1993). It has properties intermediate between those of an isotropic fluid and a crystalline material. The possibility of crystalline order occurring in the lipid bilayer of living cells is prevented by the structure of the hydrocarbon chains. These invariably contain one saturated chain and one unsaturated chain. The kinks due to the double bond prevent the lipids packing close enough together to freeze at physiological temperatures. The temperature at which the lipids make a transition to a crystalline phase is well below room temperature for RBC membranes[1]. Table 1.1 shows the chain melting temperatures for three of the major lipid components of the human RBC. They contain one chain with a carbon-carbon double bond. These can be compared with distearoyl phosphatidylcholine

[1]The normal physiological phase of the lipids is called the L_α phase and corresponds to a fluid. The phases that appear on cooling depend on quantities such as chain tilt and surface topography. Such phases may be intermediate between the fluid and the solid. These have been named gel phases. See Evans and Needham (1987).

which is saturated but has the same chain length (18 carbon atoms). The double bond is seen to lower the chain melting temperature well below physiological temperatures.

Lipid	Chain melting temperature /deg C
Dioleoyl PC	-22
Dioleoyl PE	-16
Dioleoyl PS	-7
Distearoyl PC (sat.)	55

Table 1.1 Comparison of chain melting temperatures for three major unsaturated RBC lipids with a saturated lipid (PC-phosphatidtylcholine, PE-phosphatidylethanolamine, PS-phosphatidylserine). From Israelachvilli, 1992, Table 17.1, p 378.

The geometry of the cytoskeleton influences the shape and elastic properties of a cell. In the RBC the cytoskeleton is composed of filamentous proteins connected at junctions with approximate sixfold coordination into a network. The spectrin tetramers that make up the network are joined at junctional complexes by short lengths of actin filaments, and stabilised by protein Band 4.1. The spectrin tetramers are bound at their midpoint to the PM by other proteins. The RBC cytoskeleton gives shear rigidity to the otherwise fluid PM and allows the cell to deform elastically under stress.

In living cells the PM is subject to stress in the form of osmotic pressure differences and density fluctuations of the lipids. Sometimes these stresses result in the opening up of pores in the PM and rupture (or lysis) of the cell. When a cell lyses, some of its contents are ejected into the extracellular environment. Cell lysis has been investigated in the context of artificial vesicles by several groups (Taupin et al., 1975; Ertel et al., 1993; Hallett et al., 1993). It is still imperfectly understood even for the simplest homogeneous vesicles. However, theoretical models have been developed that describe in some detail possible paths for cell lysis (Kashchiev and Exerowa, 1983; Fromherz, 1983). A

prerequisite for a cell to be stable against rupture is that any hole that forms in the fluid bilayer should reseal immediately before allowing leakage of cell contents.

The scope of this thesis is restricted to some of the physical properties of a cell that can be captured in simple model systems. I have investigated three such systems which are described briefly in the remainder of this chapter and more fully in the bulk of the thesis. Chapter 2 describes the liquid crystal simulations performed. The polymerised membrane simulations are presented in Chapters 3 and 4, and Chapter 5 describes the fluid membrane simulations. The conclusions to my work are given in Chapter 6 together with ideas for further investigation. The thesis has been organized so that a reader interested in only part of the work can move straight from the appropriate introduction in this chapter to the relevant chapters in the bulk of the thesis. An exception to this rule is that some of the analysis of polymerised membranes presented in Chapter 3 is used again in the fluid membrane analysis in Chapter 5. Technical details about the Monte Carlo (MC) simulation method, and the error analysis, are collected in Appendices A and B.

1.2 Liquid crystals

Liquid crystals (LC) are fluids whose constituent molecules are highly anisotropic (de Gennes and Prost, 1993). This makes an analytic treatment of their bulk behaviour difficult. Much effort has been devoted to studying the phases of LCs and the transitions between them because they are of great commercial value (Kaneko, 1987; Bahadur, 1991). It has been known since Onsager predicted, in the 1940s, a first-order, orientational phase transition in a gas of long, thin rods (Onsager, 1949) that LCs exhibit complex phase transitions. One of the crucial elements in understanding such transitions is the influence of molecular shape on the intermolecular interactions.

Prior to the mid 1970s it was accepted that thermotropic[2] LCs could only be formed from molecules that were shaped like long, thin rods. However, in 1977 the first LCs composed of disks were prepared and identified by Chandrasekhar et al. (1977). These systems have since been extensively investigated both experimentally (Tinh et al., 1979; Destrade et al., 1984) and theoretically (Veerman and Frenkel, 1992 and references therein).

In Chapter 2 we present our investigation of the isotropic-nematic (I-N) transition in a system of thin, hard disks in two and three dimensions. This work extends earlier studies by Eppenga and Frenkel (1984), who found a first-order orientational phase transition in a system of infinitely thin hard disks or platelets. There is no such transition in a gas of hard spheres because of the molecular symmetry. We have located the I-N transition region for disks of varying thickness in three dimensions subject to a hydrostatic pressure. The transition disappears as the thickness of the disks increases and is at most weakly first-order. These results agree with simulations performed independently by Veerman and Frenkel (1992).

The more restricted geometry of disks confined to a two dimensional interface is also considered because of interest in MoS_2 flakes at an oil-water interface (Divigalpitiya, et al., 1989) and Langmuir-Blodgett films (Josefowicz et al., 1993). The MoS_2 flakes form disk-like objects that are preferentially constrained to the interface because of their differential attraction to the water and solvent. The faces of a disk are non-polar while the edge is polar. At low density the disks lie flat at the interface. When a surface pressure is applied to the disks, they are forced closer together until their shape anisotropy causes them to orient themselves in parallel to accomodate the increased density. Similar systems studied by computer simulation include hard oblate spheroids (Wesemann, Qin and Siders,

[2]Thermotropic refers to the appearance of new phases as the temperature is varied. There is another class of LCs referred to as lyotropic that undergo phase transitions as the density is varied. This distinction is not important for our work.

1989) and spheroid-like shapes (He and Siders, 1990). We have extended previous work (Boal and Blair, 1991) to simulate a system of hard disks with complete rotational freedom constrained to intersect a planar interface between two immiscible fluids. The disks are subject to an applied surface pressure to see whether they undergo an orientational phase transition as the pressure is increased. This would be the two dimensional analogue of the I-N transition found in three dimensions (Veerman and Frenkel, 1992). We have found no evidence of such a transition. Nor is there evidence of a finite-temperature transition from a state with all the disks flat at the interface to one with them upright.

1.3 Polymerised membranes

One of the most obvious properties of a cell is its shape, and the effects of shape on behaviour may be profound. The behaviour of a cell is also strongly influenced by the material properties of its PM. Measuring the elastic properties of cells and artificial vesicles has been the goal of much recent experimental work (Evans and Needham, 1987; Evans and Rawicz, 1990; Rutkowski et al., 1991; Hallett et al., 1993). A zero-temperature description of the elastic properties of lipid bilayers was produced by Helfrich in the early 1970s (Helfrich, 1973). The bilayer deformation energy is expressed in terms of the elastic constants for the material: the compression, shear and bending moduli. Because the PM of a cell is a fluid the shear modulus vanishes. The cytoskeleton underlying the fluid bilayer in the RBC has a non-zero shear modulus due to the fixed connectivity of its constituent spectrin molecules and the two-dimensional surface to which it is bound (Nelson and Peliti, 1985; Barsky et al., 1994).

Recently materials have been constructed that show unusual elastic properties (Evans, 1991; Evans et al., 1991; Evans and Alderson, 1992). When they are stretched in one direction they expand in the the transverse direction. They have been given the name

of auxetic materials (auxetos being Greek for "that which may be increased"). Normal elastic materials such as rubber or steel always contract tranversely when stretched longitudinally. The quantity that describes the transverse strain resulting from a given longitudinal stress is called the Poisson ratio. It is defined to be positive for normal elastic materials. Auxetic materials have a negative Poisson ratio. The possibility of auxetic materials has been known theoretically for some time (Landau and Lifshitz, 1959, p 14) but no materials exhibiting such properties had been known. The auxetic materials recently fabricated are mainly foams and plastics such as high density polyethylene (Evans and Alderson, 1992).

We have performed simulations of a model of a polymerised membrane in two dimensions subject to an applied stress (Boal, Seifert, Shillcock, 1993). The model has an energy density that varies quadratically with the strain, a so-called Hooke's law network. We find that under certain conditions the network exhibits a negative Poisson ratio. This unusual behaviour results from an interplay of the network stress and entropy, and thus has an entropic origin. By contrast the negative Poisson ratio of the foams and plastics recently fabricated (Evans, 1991) results from their geometrical structure.

At zero surface stress, the area of self-avoiding networks is proportional to the membrane mass. However, we find that a non self-avoiding network exhibits a transition to a collapsed state at zero stress. This collapsed state disappears in a first-order transition at finite surface stress, as a result of a competition between the stress and entropy of the network. The Hooke's law network undergoes an unstable increase in area when the applied stress exceeds a certain limit. The analysis of the model network is developed in Chapter 3, and the results are presented in Chapter 4.

1.4 Stability of fluid membranes

The plasma membrane mentioned in Section 1.1 is a fluid. Unlike the cytoskeleton that has a fixed connectivity, the lipids that make up the PM are free to diffuse within their monolayer. The physical behaviour of the fluid lipid bilayer surrounding both real and artifical vesicles is essentially the same. An example of such similarity is the formation of pores in the lipid bilayer. Many significant cellular processes involve pores in vesicles or the PM that allow the transfer of molecules across the lipid bilayer (Alberts et al., 1989, p324). These pores occur during exocytosis (Nanavati et al., 1992) when a secretory vesicle fuses with the PM to release its contents to the exterior of a cell. They also appear if the cell is subject to osmotic stress caused by a decrease in the osmolarity of the extracellular medium (Taupin et al., 1975; Mui et al., 1993), or the application of an electromagnetic field to the PM (Zhelev and Needham, 1993; Freeman et al., 1994).

When the bilayer is stable, open pores reseal as the hydrophobic force on the lipids pulls them together. This stability has been interpreted in terms of an edge energy around a pore that acts to reseal it (Litster, 1975; Fromherz, 1983). The edge energy tends to decrease the size of a spontaneously created pore in competition with, for example, an osmotic pressure tending to swell, and burst, the cell. On physiological time scales the fluid bilayer is stable against small stretching pressures. However, given sufficient stress the membrane is unstable to forming a large pore allowing leakage of the cell contents and possible rupture of the membrane. In the last system studied in this thesis we discuss the stability of a model fluid membrane against spontaneous hole formation.

We allow a single hole to develop in a model fluid membrane subject to a line tension (energy per unit length) around the hole's perimeter. If the hole grows, it increases the energy of the system but the system may gain entropy due to the perimeter of a large hole having greater configurational freedom than a small one. The resulting change in the

free energy at finite temperature may be positive, in which case the hole will shrink and disappear, or negative, in which case the hole will continue to grow.

The competition between the energy of the hole and the entropy of the boundary leads to a transition from a stable state of the membrane with no hole at high line tension to another stable state with a large hole in the membrane at a finite value of the line tension. The predicted value of this line tension is $2.5x10^{-21}$ J/nm for a biological membrane and is an order of magnitude below some experimental values (Hallett et al., 1993; Needham and Hochmuth, 1989). Membranes in which the line tension is below this value are unstable to disintegration into a ruptured state. The shape and stability of the hole in a disintegrating membrane are described. We also investigate the behaviour of the transition when a pressure is applied to the membrane. This pressure may be positive, when it compresses the membrane, or negative, when it stretches the membrane. The investigation of the stability of the model fluid membrane to hole formation is presented in Chapter 5.

1.5 Summary

The physical properties of the cell plasma membrane and the underlying structural components are crucial to the stability and function of a cell. In this chapter we isolate several aspects of the cell for study: a liquid crystalline phase transition analogous to that of the molecular components of the plasma membrane, the stability of the fluid bilayer to hole formation, and the elastic properties of the network that underlies the red blood cell plasma membrane.

The first system we study is an anisotropic fluid of disk-shaped molecules in three dimensions under an applied hydrostatic pressure. As the pressure is increased the system undergoes an orientational phase transition to a nematic phase. The transition disappears as the thickness of the disks is increased. When the disks are constrained to intersect a

planar interface betwen two immiscible fluids and given a differential attraction to the fluids, the transition also disappears.

The next system we study is a network model of a polymerised membrane in two dimensions under an applied stress. The network is composed of vertices connected by Hookean springs. As the tension is reduced, the network changes from being highly ordered to being increasingly disordered. The model shows the unusual property of becoming auxetic as the tension is reduced: it expands transversely when stretched longitudinally. When the elements of the network are allowed to intersect one another, the network undergoes a collapse transition at a finite value of the stretching tension. The Hookean network also undergoes a transition to an unstable state of infinite size when the stretching tension exceeds a critical value.

Finally, we investigate the thermodynamic stability of a model fluid membrane to the process of opening a single hole. In real lipid bilayers transient pores are resealed by an effective line tension around the boundary of the pore. We have found that the model membrane becomes unstable to opening up a hole once the line tension is reduced below a critical value. We investigate the scaling behaviour of the hole boundary at the transition point and the effect on the transition of a non-zero pressure on the membrane.

CHAPTER 2

LIQUID CRYSTAL SIMULATIONS

2.1 Introduction

Liquid crystals are fluids whose properties are intermediate between those of crystalline solids and ordinary liquids (Brock et al., 1989). They have unusual optical properties and are extensively used in display technology (Kaneko, 1987). They have been known to experimentalists for over a hundred years (Kelker, 1973 and references therein). However, their structure and behaviour are complicated. In particular, they can possess several phases with properties intermediate between the solid and liquid phases (de Gennes and Prost, 1993). This behaviour is believed to result from the highly anisotropic shape of the constituent molecules that make up the liquid crystal, although there is some question about the relative influence of the hard-core repulsion and the long-range attraction between molecules[1] (Frenkel, 1987).

The most common LCs have a long, rigid, rod-like structure. One example is 8OSI, shown below in Fig. 2.1:

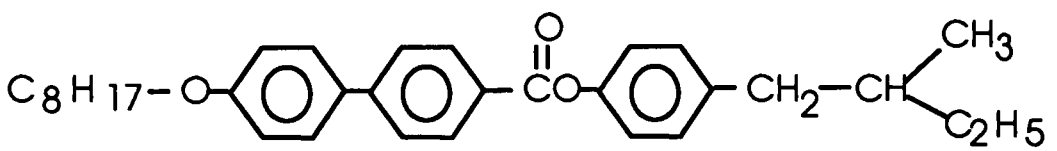

Figure 2.1 Molecular structure of 8OSI

[1]The extreme examples are the simulations of the Maier-Saupe model which has only long-range, anisotropic, attractive forces (Lebwohl and Lasher, 1972) and hard rod simulations (Zwanzig, 1963) which have only hard-core repulsive forces. Both models show an orientational phase transition.

Another example is the tobacco mosaic virus, which has a hollow, rod-like structure. These structures can take up several phases depending on their density, and the non-crystalline phases may possess long-range orientational order.

It was predicted by Onsager in the 1940s that a system of long, thin rods should have a strong first-order phase transition from a low-density isotropic phase to a nematic phase at higher density (Onsager, 1949). The prediction was based on a second-order virial expansion and was subsequently supported by a calculation of Zwanzig (1963), who used a virial expansion up to 7th order.

Several models attempting to capture the thermodynamic properties of rod-like molecules have been produced. In the 1970s Viellard-Baron (1974) determined the equation of state of a system of hard spherocylinders from MC simulations. A spherocylinder consists of a cylindrical rod capped with a hemisphere at each end. Several groups have studied the orientational phase behaviour of the hard spherocylinder system from theory (Cotter, 1977; Somoza and Tarazona, 1990) and MC simulations (Stroobants et al., 1987; Frenkel, 1988; Frenkel, Lekkerkerker and Stroobants, 1988; Veerman and Frenkel, 1990). Other workers have studied ellipsoids (Frenkel, Mulder and McTague, 1984; Frenkel and Mulder, 1985) as well as cylinders themselves (Duro et al., 1988).

As a result of these simulations the essential features of the phase transitions present in model liquids of rod-like molecules are known. At low densities the molecules are free to translate and rotate independently of each other. They have neither positional nor orientational order. Under increasing pressure the molecules start to interact via their anisotropic shape. A phase transition occurs to a more ordered phase (the nematic phase) in which the molecules still lack positional order but are orientationally ordered. At higher densities other LC phases may occur, such as Smectic A, where some positional order is

also gained. The I-N phase transition is found to be weakly first-order in the simulations (Frenkel and Mulder, 1985).

In 1979 the first examples of disk-like, or discotic, liquid crystals exhibiting a nematic phase were made by Hguyen Huu Tinh et al. (1979). Their compounds are based on hexasubstituted triphenylenes. An example is shown below in Fig. 2.2, where R is either a long-chain ether, $R = C_nH_{2n+1}O$, $n = 1...13$, or an ester, $R = C_nH_{2n+1}CO_2$, $n = 1...15$.

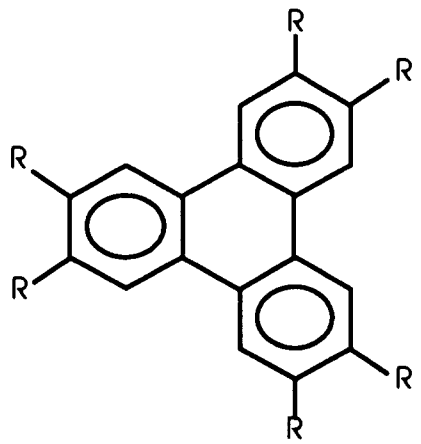

Figure 2.2 Molecular structure of a typical discotic liquid crystal that exhibits a nematic mesophase.

These substances are found to exhibit several highly viscous thermotropic mesophases with diverse optical textures. X-ray diffraction measurements of the compounds (Chandrasekhar, 1977; Levelut, 1979) show that the mesophases are made up of regular or irregular stacks of disks. Since then many examples of discotic liquid crystals have been found (Destrade et al., 1984). Correspondingly, simulations of the equation of state of models of discotic LCs have been performed (Wojcik and Gubbins, 1984). However, there are significant differences between the model systems simulated and real LCs. In a recent review of the properties of discotic liquid crystals, Chandrasekhar (1990) states that the presence of flexible side-chains on the disk-shaped cores is essential to the formation of

the mesophases. The long hydrocarbon chains contribute to the entropy in the liquid phase but are frozen out in the solid. This molecular characteristic has not been included in simulation models and yet the models show several distinct phases of discotic LCs. These include a nematic phase in a system of infinitely thin disks (Eppenga and Frenkel, 1984), and nematic and columnar phases in a system of cut-spheres (Veerman and Frenkel, 1992) and dipolar cut-spheres (Zarragoicoechea, Levesque and Weis, 1993).

A detailed simulation of infinitely thin disks, called platelets, was carried out in 1984 by Eppenga and Frenkel. They concluded that for a phase intermediate between the isotropic liquid and crystalline solid to exist, the hard disks must have two properties:

- they must be sufficiently anisotropic to favour orientational order, and
- at the temperature and density of the I-N transition, the solid phase must be thermodynamically unstable.

The simulations discussed so far have been for three-dimensional systems. Some work on two-dimensional systems has also been performed (Fraser et al., 1990; He and Siders, 1990). Hard spherocylinders with their centres confined to a plane exhibit a first-order I-N transition (Coldwell et al., 1974). Wesemann, Qin and Siders (1989) study a monolayer of hard, oblate spheroids, with their centres confined to a plane, using Onsager's theory and Monte Carlo simulation. They point out that the system of spheroids confined to a plane is isotropic only at zero pressure. As the pressure is increased, the spheroids' short axes tip into the plane. Next, the long axes of the spheroids gradually align in a continuous transition to a nematic phase. Wesemann et al. also find that the transition density decreases as the eccentricity of the spheroids increases.

While the LC molecules of biological importance are mainly rod-like in their geometry, the behaviour of discotic molecules is of importance in understanding the nature

of liquid crystals. Several experimental realisations of disk-shaped objects confined to a plane are known (Divigalpitiya et al., 1989; Josefowicz et al., 1993) and the effect of dimensionality on the behaviour of a system of anisotropic disks is unclear. Wesemann et al. (1989) study hard spheroids confined to a plane and comment that the extrapolation to hard disks is unknown. In this chapter we use computer simulations to investigate the behaviour of discotic molecules, both in three dimensions and when confined to a two-dimensional interface.

2.2 Simulation of isotropic/nematic transition for hard disks in 3D

We simulate a system of N disks of varying thickness confined to a cubical box in 3D. The disks have a radius R, and we express their thickness T in units of the radius. Because the disks interact only via their hard-core repulsion, the temperature only appears in combination with the hydrostatic pressure as the parameter βp. We use the Metropolis Monte Carlo technique in the constant pressure, constant temperature (NPT) ensemble. Details of this technique are given in Appendix A.

These simulations provide a model for investigating the isotropic to nematic phase transition of discotic liquid crystals in 3D. If the disks are infinitely thin, there is a sharp I-N transition as found by Eppenga and Frenkel (1984). By contrast, isotropic objects, such as hard spheres, can have no such transition. We expect the behaviour of the disks to approach that of hard spheres as their thickness increases and they lose most of their geometrical anisotropy. We aim to find the dependence of the transition on disk thickness.

The isotropic phase of a liquid has spherical symmetry: the orientational distribution of the molecules is random. We may express this mathematically by defining the single-particle orientational distribution function $f(\theta,\phi)$. The fraction of molecules whose symmetry axes have spherical polar angles in the range θ to $\theta+d\theta$, ϕ to $\phi+d\phi$ with respect to a fixed axis is $f(\theta,\phi)\sin\theta d\theta\, d\phi$. The polar angle is restricted to the range 0 to

$\pi/2$, because the molecules are taken to be up-down symmetric. The azimuthal angle has the usual range of 0 to 2π. The isotropic state corresponds to

$$f(\theta,\phi)=\frac{1}{2\pi}. \tag{2.1}$$

In ordered LC phases the molecules tend to align themselves in some way. For example, a nematic LC phase has cylindrical symmetry with the molecular axes approximately parallel. The deviation of the orientational distribution function from spherical symmetry is measured by a set of order parameters. For an axially symmetric distribution, the most general form of this function is:

$$f(\theta)=\sum_{l\ even}^{\infty} a_l P_l(\cos\theta) \tag{2.2}$$

where θ is the angle of the molecular orientation with the axis of symmetry (called the nematic director), $P_l(\cos\theta)$ are the Legrendre polynomials, and a_l are the expansion coefficients. Note that we assume the molecules have cylindrical symmetry and are up-down symmetric, so that a_l with odd l vanish. The values of the coefficients are related to the values of the Legendre polynomials averaged with respect to the distribution function $f(\theta)$:

$$\langle P_l(\cos\theta)\rangle=\left(\frac{1}{2l+1}\right)a_l. \tag{2.3}$$

The quantities $\langle P_l(\cos\theta)\rangle$, with l even, are the order parameters of the system. For an isotropic liquid all the coefficients with $l\neq 0$ are zero. The first non-trivial average, $\langle P_2(\cos\theta)\rangle$, is often used as the nematic order parameter.

Our investigation of the I-N transition proceeds as follows. Consider a system of disks with fixed T/R placed in a cubical box which has periodic boundary conditions to minimise the effects of the boundaries. The initial configuration is defined by giving each

disk a random position and orientation in the box. The simulation is run to remove the influence of the initial conditions and then the disk positions and orientations are stored at fixed intervals throughout the remainder of the simulation for analysis. Each step in the simulation consists of an attempt to move and rotate each disk by a random amount chosen from a fixed range. An attempt to move every disk is called a *sweep* through the system. After a fixed number of sweeps, an attempt is made to rescale the volume of the simulation box. A small random change is made in each of the box side lengths and all the disk coordinates are rescaled by the new lengths. In these simulations the box is cubical so all the sides are rescaled by the same factor. The simulation is run until enough configurations have been collected to allow extraction of the nematic order parameter. Technical details of the simulation method are given in Appendix B, where we also discuss the error analysis for the simulations.

The nematic order parameter, defined by Eq. (2.3) with $l = 2$, can be obtained from an ensemble average over the configurations of a simulation using:

$$S = \left\langle \frac{1}{N} \sum_{i=1}^{N} \left(\tfrac{3}{2} \cos^2 \theta_i - \tfrac{1}{2} \right) \right\rangle, \tag{2.4}$$

where the sum is over all the molecules and θ_i is the angle of the ith molecular axis with the nematic director. Since the orientation of the nematic director is not known *a priori*, the calculational procedure is to evaluate

$$\begin{aligned} S' &= \left\langle \frac{1}{N} \sum_{i=1}^{N} \left(\tfrac{3}{2} (\underline{n}.\underline{u}_i)^2 - \tfrac{1}{2} \right) \right\rangle \\ &= \left\langle \frac{1}{N} \sum_{i=1}^{N} \underline{n}.\underline{\underline{Q}}_i.\underline{n} \right\rangle, \end{aligned} \tag{2.5}$$

where $\underline{n}$ is an arbitrary unit vector and $\underline{u}_i$ is the normal vector to the ith disk. The tensor $\underline{\underline{Q}}_i$ is defined in terms of the normal vector $\underline{u}_i$ by

$$\underline{\underline{Q}}_i = \tfrac{3}{2}\underline{u}_i \cdot \underline{u}_i - \tfrac{1}{2}\underline{\underline{I}}, \qquad (2.6)$$

where the outer product of the normal vector is taken with itself, and $\underline{\underline{I}}$ is the 3D unit matrix.

Obviously, $\underline{\underline{Q}}_i$ is a symmetric, traceless tensor. It may be averaged over all N disks in a single configuration to get

$$\underline{\underline{Q}} = \frac{1}{N}\sum_{i=1}^{N} \underline{\underline{Q}}_i, \qquad (2.7)$$

where $\underline{\underline{Q}}_i$ is the tensor for the ith disk. The eigenvalues of $\underline{\underline{Q}}$ for each configuration are extracted and then averaged over all configurations in the simulation to give the nematic order parameter. Let the average values of these eigenvalues be $\langle\lambda_1\rangle, \langle\lambda_0\rangle, \langle\lambda_{-1}\rangle$ ordered from the largest to the smallest. Notice that λ_1 is constrained to be non-negative by the fact that $\underline{\underline{Q}}$ is traceless. Either $\langle\lambda_1\rangle$ or $\langle -2\lambda_0\rangle$ may be taken as the order parameter: both give comparable results to within the accuracy of the simulations. The advantage of the middle eigenvalue is that the amplitude of its fluctuations in the isotropic phase is smaller than that of the largest eigenvalue. In the nematic phase the eigenvalues are related by $\lambda_0 = \lambda_{-1} = -\tfrac{1}{2}\lambda_1$, while in the isotropic phase they are all zero.

2.3 Results of 3D simulations

We have simulated a system of 100 disks of radius R and thickness $T/R = 0.02, 0.2, 0.4, 1.0$. The first of these may be compared with the infinitely thin platelet results of Eppenga and Frenkel (1984).

The density of the system is apparently a smooth function of the applied pressure for all thicknesses to the accuracy of our results. That is, any discontinuous change in the density due to molecular ordering is small. The average volume per disk normalised to the single disk volume, $v_0 = \pi R^2 T$, is shown in Fig. 2.3. This figure shows that the thick disks

(with T/R of 0.4 and 1) become close-packed at pressures above $\beta pR^3 = 4$ and behave essentially like an incompressible fluid. The thin-disk fluid is not yet incompressible at the highest pressures we could simulate. Figure 2.4 compares the equations of state for the hard disk systems. At high densities, which depend on the disk thickness, the thin disks behave like a highly compressible fluid (with $p\langle V\rangle/NkT = 4$ for $T/R = 0.02$). This is substantially larger than the ideal gas value of $p\langle V\rangle/NkT = 1$.

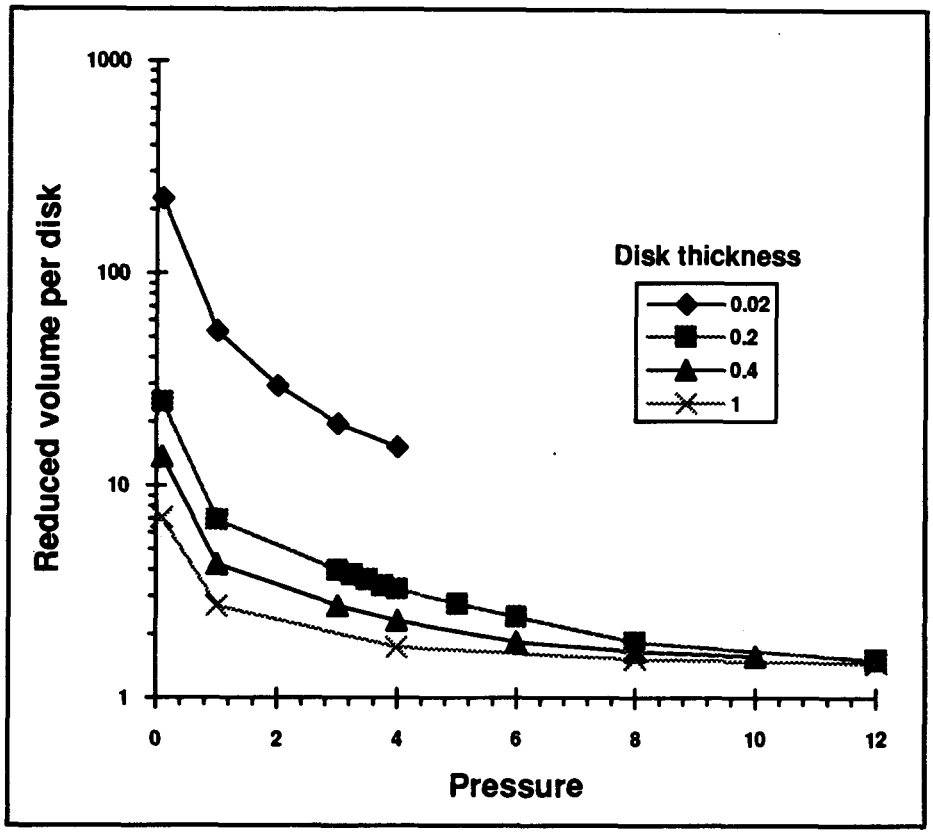

Figure 2.3 Reduced volume per disk $\langle V\rangle/Nv_0$ against pressure βpR^3 for disk thicknesses $T/R = 0.02, 0.2, 0.4, 1.0$.

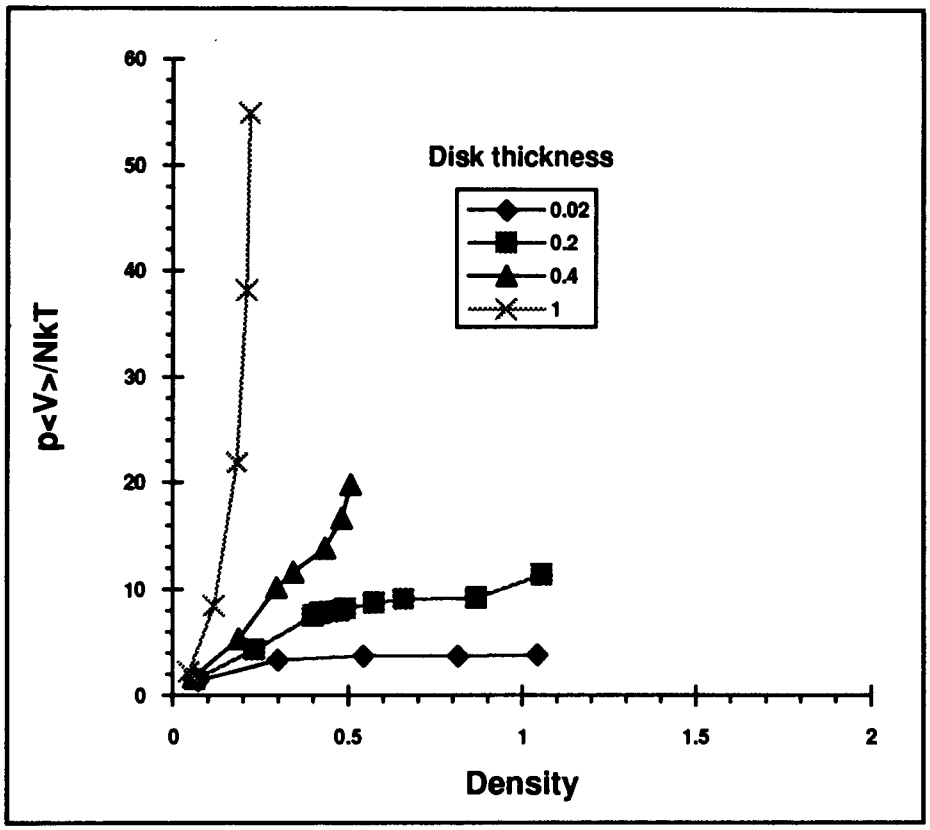

Figure 2.4 Equation of state for hard disks with thickness $T/R = 0.02, 0.2, 0.4, 1.0$ in a cubical box. The density is $NR^3/\langle V \rangle$.

Next consider the behaviour of the deviation in the mean polar angle as a function of pressure. The mean polar angle is measured with respect to one of the axes of the simulation box. The standard deviation in the polar angle indicates the degree of alignment of all the disks within a configuration. It is defined by

$$\sigma^2(\theta) = \langle \theta^2 \rangle - \langle \theta \rangle^2 \qquad (2.8)$$

where $\langle \theta \rangle = 1$ radian, $\langle \theta^2 \rangle = \pi - 2$ square radians in the isotropic phase, so $\sigma(\theta) = 0.376$ radians or 21.5°.

Figure 2.5. shows that the deviation in the mean polar angle for disks of all thicknessess has the purely random value of 21.5 degrees at low pressure, $\beta p R^3 < 1$. There is a marked increase in alignment observed with increasing pressure for disks with $T/R = 0.02, 0.2, 0.4$. The pressure at which the disks start to align increases with the thickness of the disks. The disks with $T/R = 1$ show little tendency to align at the pressures considered.

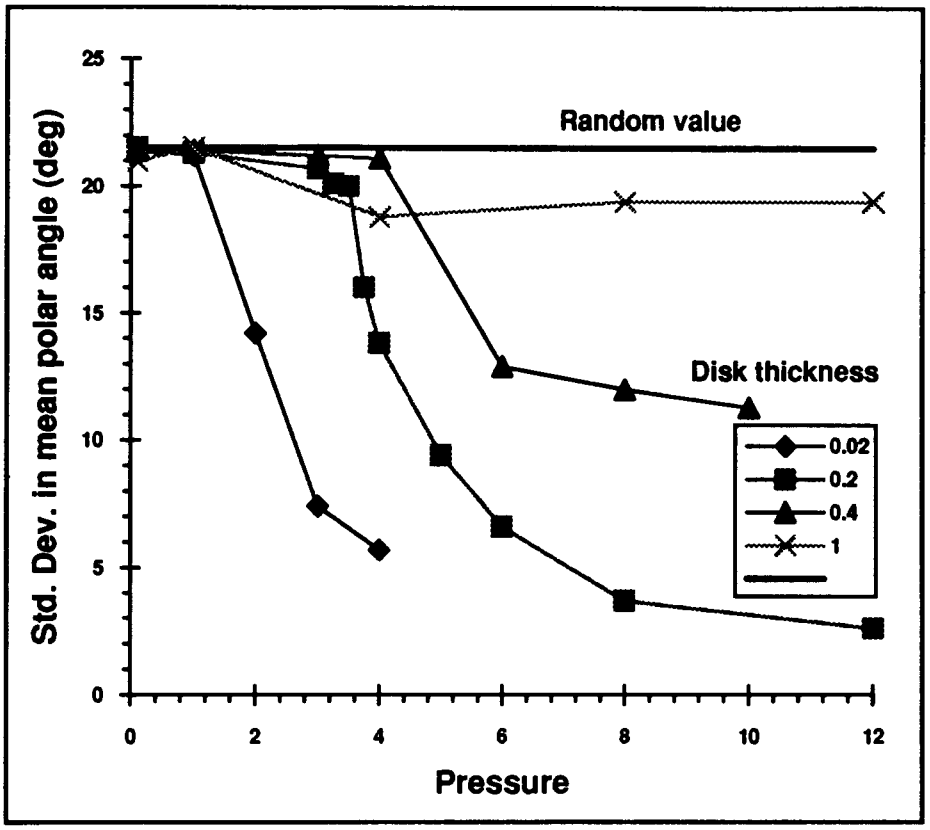

Figure 2.5 Standard deviation of the mean polar angle $\langle\theta\rangle$ against pressure βpR^3 for disk thicknesses $T/R = 0.02, 0.2, 0.4, 1.0$.

Next we analyse the largest and the middle eigenvalues of the orientational order parameter derived from the $\underline{\underline{Q}}$-tensor of the platelets as described in Section 2.2. The results are shown in Figures 2.6 and 2.7. It is clear that the disks with $T/R < 0.2$ undergo a sharp orientational transition as their density increases, while the thicker disks with $T/R \geq 0.4$ show no such transition over the pressure range investigated. By comparing Figures 2.6 and 2.7 one can see that there is no noticeable difference between the behaviour of the largest and middle eigenvalues in the nematic phase, although the fluctuations in the middle eigenvalue are closer to zero in the isotropic phase. To show that the transition occurs at a fixed density, independent of disk thickness, we show the data for the middle eigenvalue plotted against density in Figure 2.8. The transition occurs at a reduced density of $NR^3/\langle V \rangle = 0.50 \pm 0.05$. We have indicated the close packed density for the disks with $T/R = 0.4,\ 1.0$ by arrows. These disk systems approach but are obviously less than the close-packed density. It should be noted that the rounding of the curve for disks with $T/R = 0.02$ is an artifact of the drawing and does not reflect the finite system size.

Eppenga and Frenkel (1984) also find that the transition occurs at a reduced density of $NR^3/V = 0.5$. However, their results and those of Veerman and Frenkel(1992) are in the NVT ensemble and our work is in the NPT ensemble. The agreement between the results shows that the transition is not ensemble dependent to the accuracy of the simulations.

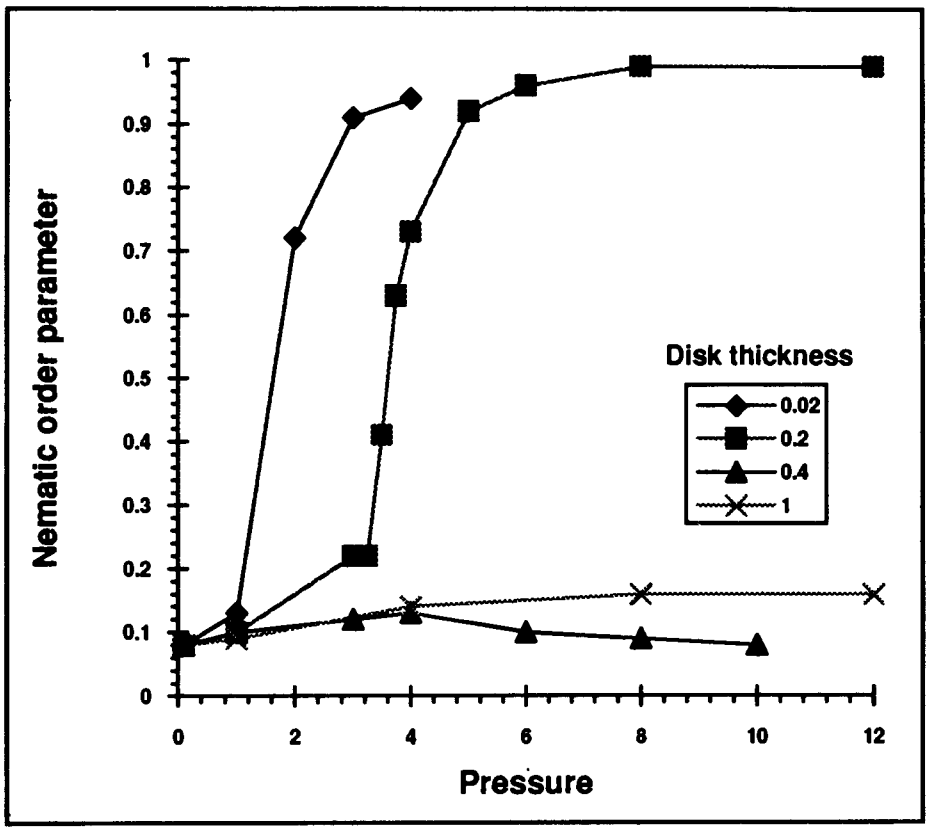

Figure 2.6 Nematic order parameter $\langle \lambda_1 \rangle$ against pressure $\beta p R^3$ for disk thicknesses $T/R = 0.02, 0.2, 0.4, 1.0$.

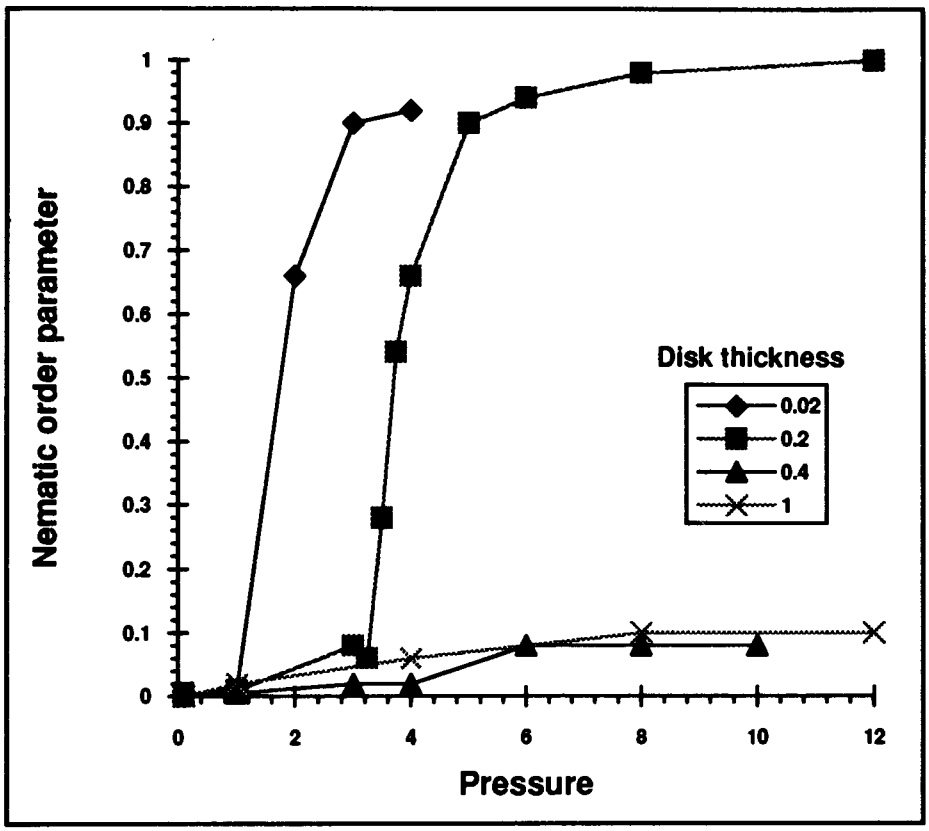

Figure 2.7 Nematic order parameter $\langle -2\lambda_0 \rangle$ against pressure βpR^3 for disk thicknesses $T/R = 0.02, 0.2, 0.4, 1.0$.

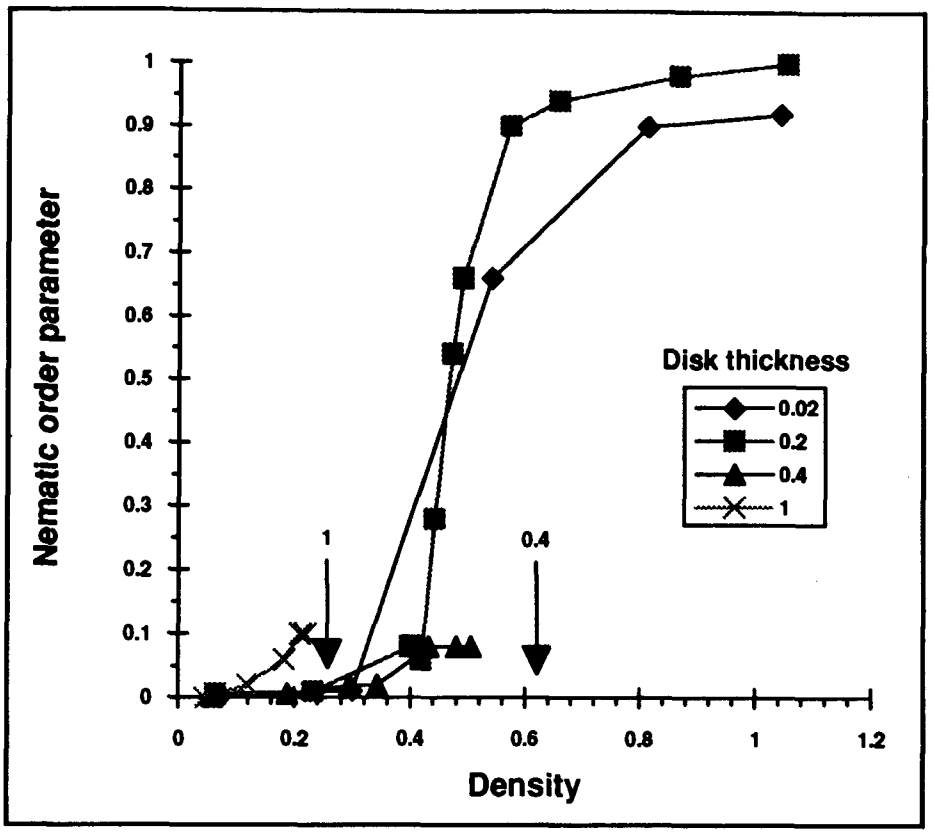

Figure 2.8 Nematic order parameter $\langle -2\lambda_0 \rangle$ against density $NR^3/\langle V \rangle$ for disk thicknesses $T/R = 0.02, 0.2, 0.4, 1.0$. Arrows indicate the close-packed density for the disks with $T/R = 0.4$ and 1.0 as mentioned in the text.

We have taken the system with $T/R = 0.2$ through the transition in both directions of increasing and decreasing pressure. The results are shown in Fig. 2.9. In both directions each run is started using an initial configuration from the run at the preceeding pressure. This ensures that the system is started near equilibrium at the higher pressures investigated. It is seen that there is no significant dependence of the order parameter on the direction in which the transition is approached. This lack of hysteresis suggests that the transition is at most weakly first-order. Most of the simulations used 100 disks and the accuracy of the numerical results is limited to 10% by statistical error. Figure 2.9 shows, for disks of thickness $T/R = 0.2$, that the change in the order parameter on going through the transition in opposite directions is less than 7%.

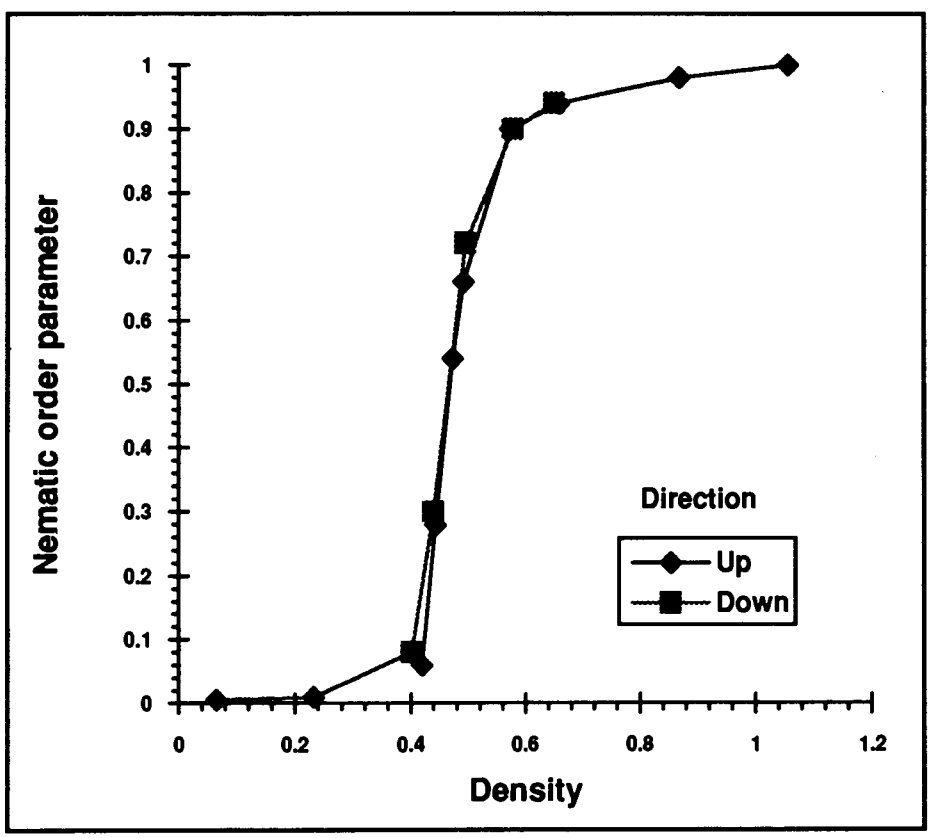

Figure 2.9 Nematic order parameter $\langle -2\lambda_0 \rangle$ against density $NR^3/\langle V \rangle$ for disk thickness $T/R = 0.2$ traversing the transition in both directions.

Figure 2.10 shows, for disks with $T/R = 0.2$, the nematic order parameter for two systems with 64 and 100 disks respectively. The difference in the order parameter of the two systems is very slight, and does not affect the conclusion that the isotropic-nematic transition occurs at a reduced density of approximately $NR^3/\langle V \rangle = 0.5$.

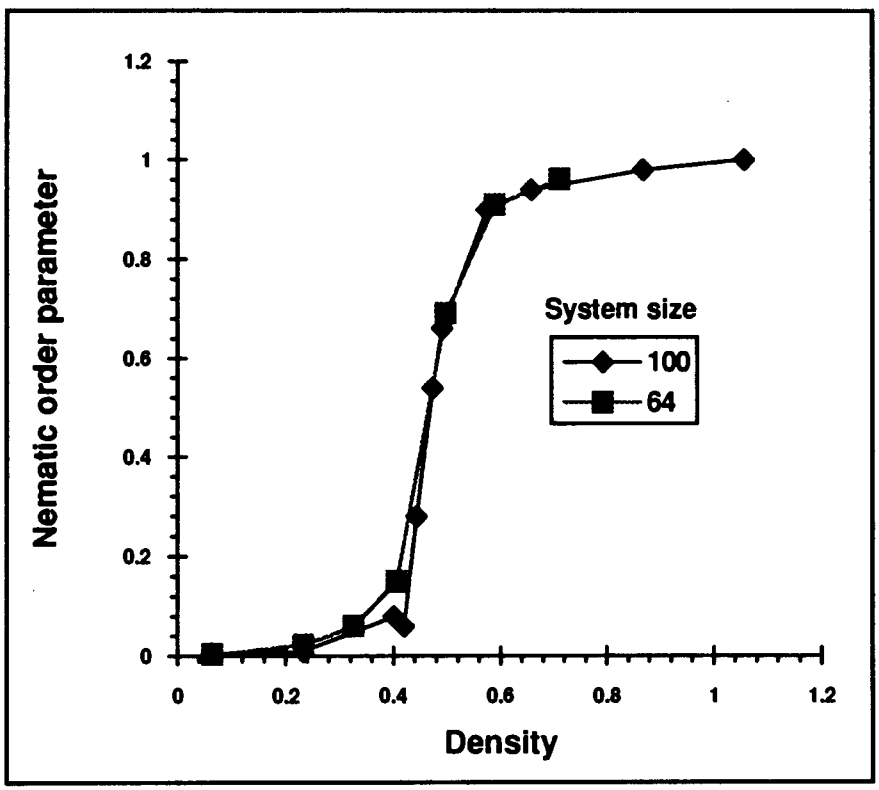

Figure 2.10 Nematic order parameter $(-2\lambda_0)$ against density $NR^3/\langle V \rangle$ for disk thickness $T/R = 0.2$ and system sizes of 64 and 100 disks.

We use the disk coordinates (X, Y, Z, θ, ϕ) averaged over all disks in a configuration to measure positional and orientational correlations between the disks. Near the transition, the collective correlation functions of the disk coordinates require many Monte Carlo steps to decay. However, independent runs of a system at a given pressure showed that the differences between the order parameters for the two runs were less than the statistical errors. Further, the correlation times for the coordinates of a single disk are at least an order of magnitude smaller than the collective correlation times (see Appendix B). The single-particle orientational correlation times for the disks are of the order of 50,000 sweeps for all pressures for thick disks, rising to 400,000 sweeps at the transition point for the thinnest disks. We run the systems for 1,000,000 sweeps prior to collecting data to allow them to equilibrate and then allow 50,000 sweeps between sample configurations. This ensures that the configurations are substantially independent at low density and thus represent a reasonable average over the accessible phase space of the system. At high density, the disks are prevented from moving far by their neighbours and the large collective correlation time in the polar coordinate reflects the correlations between the disks and not insufficient simulation time.

2.4 Simulation of isotropic/nematic transition for hard disks at an interface

2.4.1 Restricted orientation model of disks at an interface

In a previous paper Boal and Blair (1991) investigated the phase behaviour of a set of platelets restricted to an interface between two immiscible fluids. The platelets were representative of MoS_2 monolayer segments at an oil/water interface, a system of some interest experimentally (Divigalpitiya, Frindt and Morrison, 1989). We now describe their simulations and show how we have extended this work to give a more complete picture of platelets confined to an interface.

The model platelets interact with each other via their geometrical hard-core repulsion. They also have an attraction for the two liquids that define the interface. Let liquid 1 (usually an organic solvent in experiments) be above the interface, and liquid 2 (usually water) be below, and let $k_{f1}, k_{e1}, k_{f2}, k_{e2}$ be the interaction energy per unit area of the platelet face (f) and edge (e) exposed to liquids 1 and 2. We assume that the energy of attraction is simply given by the amount of area exposed to the given liquid. The Hamiltonian for a single platelet is then

$$H = g_f A_{f2} - g_e A_{e2} - S_{12} A_{12} - \left(k_{f1} A_{ft} + k_{e1} A_{et}\right) \qquad (2.9)$$

where A_{f2}, A_{e2} are the areas of the faces and edge exposed to liquid 2 and A_{ft}, A_{et} are the total areas of the faces and edge respectively. The constants $g_f = k_{f1} - k_{f2}, g_e = k_{e2} - k_{e1}$ are the differential attraction energies per unit area of the face and edge for the liquids. The signs are chosen so that positive values of g_f and g_e correspond to the face being more attracted to liquid 1 and the edge being more attracted to liquid 2, similar to the presumed experimental situation for MoS_2 at an oil-water interface. Finally, S_{12}, A_{12} are the surface tension and area of liquid-liquid interface excluded by the platelet respectively. The term in brackets in Eq. (2.9) is the energy of a platelet totally immersed in liquid 1.

A single platelet has its minimum energy state when it intersects the interface. This result is unaltered by the presence of surface tension, so the work here was carried out at zero surface tension. The extension of this model to a system of platelets at finite temperature requires several independent parameters to define the thermodynamic state of the system. These parameters occur in the four dimensionless combinations $T/R, \beta g_f R^2, \beta g_e R^2$ and $\beta p R^2$.

An interesting situation arises if a flat disk has a lower energy than an upright one. If a surface pressure is applied to a system of such disks at the interface there will be a competition between the interaction energy of the disks and the interface, and the pressure

attempting to force the disks upright so as to reduce the overall surface area of the system. It was conjectured (Boal and Blair, 1991) that this might lead to a sharp transition at a finite temperature from a low-density flat phase to a high-density upright phase. The upright disks may then order in a nematic phase at high pressure. A Monte Carlo simulation using a restricted set of disk configurations showed a flat-to-upright phase transition only at zero temperature. Here we study the same system with full orientational freedom of the disks.

2.4.2 Full orientational model of disks at an interface

We consider a set of platelets with radius R and thickness T at an interface which are allowed to translate and rotate freely subject to their body intersecting the interface. This restriction is necessary to ensure that raising the surface pressure in the simulation does not simply result in disks being squeezed away from the interface. As for the three-dimensional simulations we again work in the NPT ensemble.

The energy of each disk is given by Eq. (2.9) and the appropriate free energy is the Gibbs potential where the energy and entropy of the system are functions of the positions and orientations of all the disks. A total of 144 disks with $T/R = 0.2$ are randomly placed in a rectangular box so that each one intersects the interface. The ratio $g_e/g_f = 5$ so that the minimum energy state of a single platelet has it lying flat at the interface. The derivation of the ground state of a single platelet as a function of the ratios T/R and g_e/g_f is given in Boal and Blair (1991). The plane of the interface is continued using periodic boundary conditions in the x and y directions. After allowing the initial configuration to relax to equilibrium, data are collected at intervals. The technical details of the simulation are given in Appendix B.

2.5 Results of 2D simulations

The aim of the simulations is two-fold: to see if there is a flat-to-upright transition in a system of platelets confined to an interface, and to see if an isotropic to nematic transition exists as the temperature and pressure are varied. It is clear from Boal and Blair (1991) that the change in the orientation of the disks with lateral pressure is smooth when the disks have only two orientations, flat and upright. It was suggested that this behaviour might change when the disks are given full orientational freedom.

The interfacial area per disk in Fig. 2.11 decreases with increasing pressure at all the temperatures we have simulated, and shows no sign of a discontinuity.

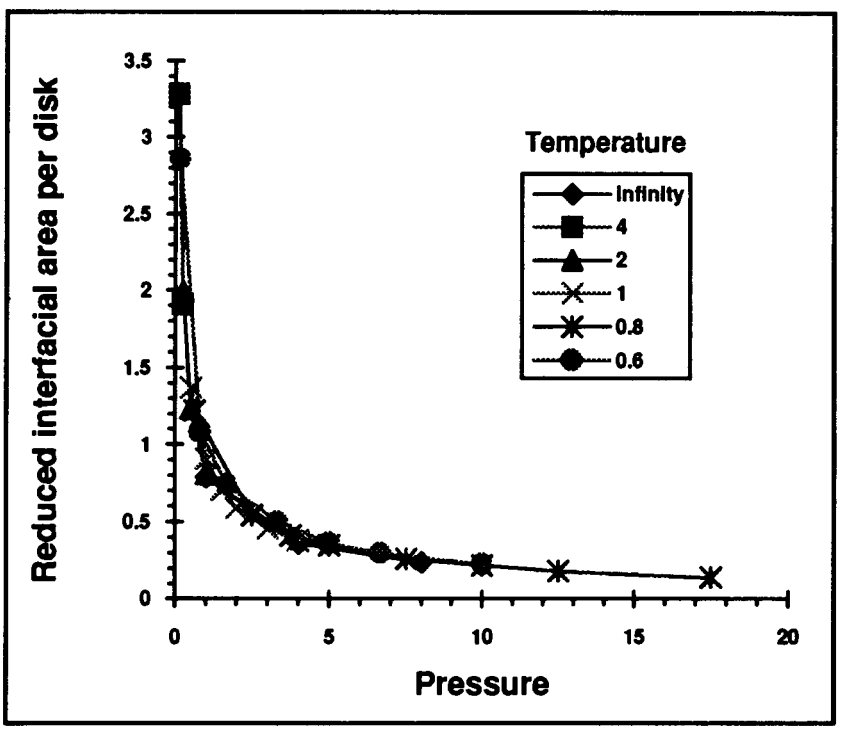

Figure 2.11 Reduced interfacial area per disk $\langle A \rangle / N\pi R^2$ against pressure $\beta p R^2$ at all temperatures $(\beta g_f R^2)^{-1}$ investigated in the simulation. The disks have $T/R = 0.2$ and $g_e/g_f = 5$.

The behaviour of the compressibility factor $p\langle A\rangle/NkT$ is shown as a function of density in Fig. 2.12. This quantity is unity for an ideal gas. There is a slight dependence on temperature, the system being more incompressible at low temperatures, but overall the behaviour is that of a dense gas. In the low density regime $\left(NR^2/\langle A\rangle < 0.7\right)$ the compressibility factor agrees with the second-order virial equation for a fluid of hard disks in two dimensions.

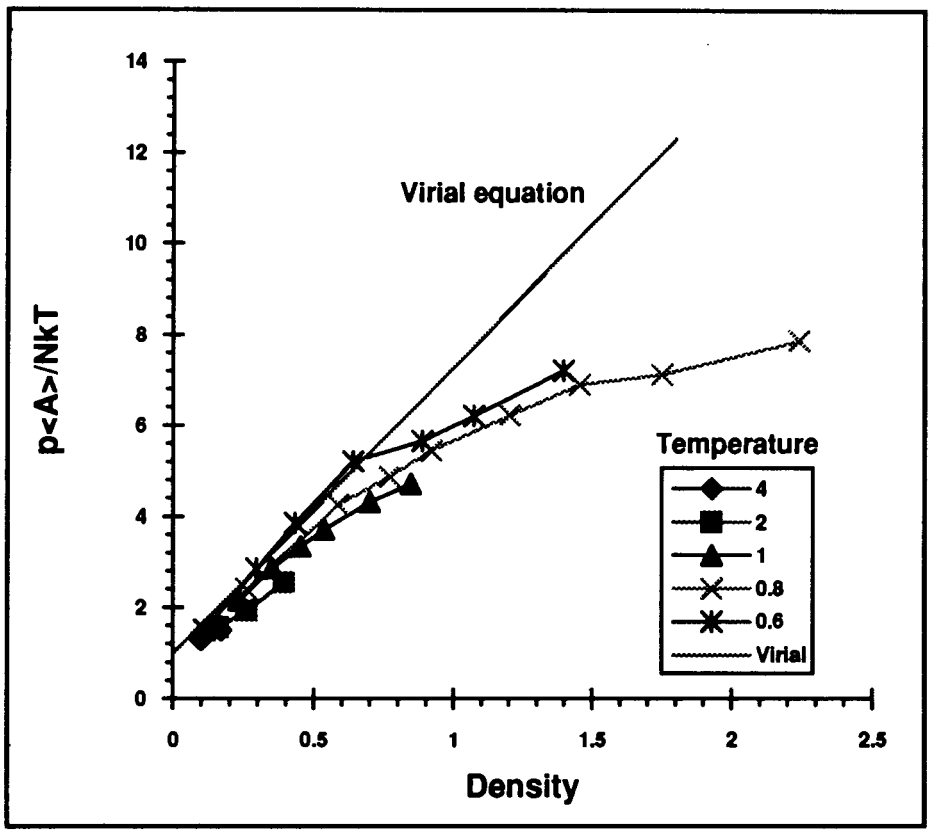

Figure 2.12 Equation of state for hard disks with rotational freedom, restricted to lie at the interface, at all temperatures $\left(\beta g_f R^2\right)^{-1}$ investigated in the simulations. The density is $NR^2/\langle A\rangle$, and the remaining parameters are as for Fig. 2.11. The 2D virial equation is shown for comparison.

We show the mean polar angle and its standard deviation in Figs. 2.13 and 2.14. At the lowest temperature we simulate, $\left(\beta g_f R^2\right)^{-1} = 0.6$, and a pressure of $\beta pR^2 = 0.1$, the mean polar angle falls below the random value, indicating that the disks are starting to lie flat at the interface. There is evidence for an increase in the average polar angle, and a narrowing in the distribution, as the pressure rises. This suggests that the disks are turning from lying in the plane of the interface to being normal to it. The change in the mean polar angle is almost independent of temperature, although the narrowing in the distribution of the polar angle is steeper at temperatures $\left(\beta g_f R^2\right)^{-1} < 1.0$ compared to the infinite temperature simulation. Note that the infinite temperature curve is one for which the interaction energy of the platelets with the interface is zero while the pressure is non-zero.

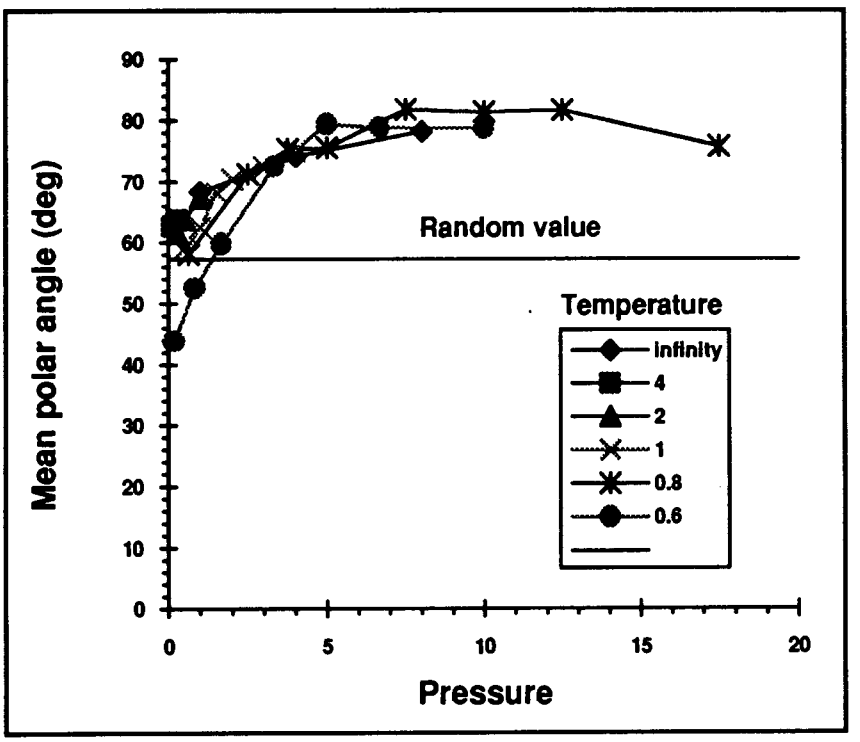

Figure 2.13 Mean polar angle (θ) of disks against pressure βpR^2 at all temperatures $\left(\beta g_f R^2\right)^{-1}$ considered. The remaining parameters are as for Fig. 2.11.

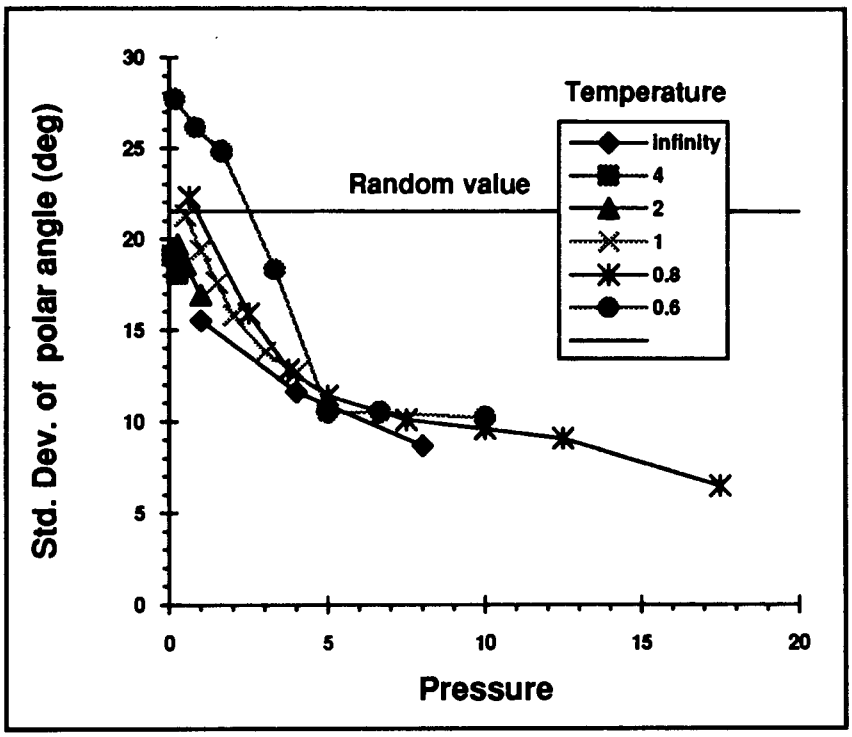

Figure 2.14 Standard deviation of the mean polar angle $\langle\theta\rangle$ of disks against pressure βpR^2 at all temperatures $\left(\beta g_f R^2\right)^{-1}$ considered. The remaining parameters are as for Fig. 2.11.

The above measures show no clear sign of an orientational phase transition. This is supported by the tensor order parameter (defined in Section 2.2) which shows, in Figs. 2.15 and 2.16, that there is no sharp transition from an isotropic to a nematic phase for the upright disks as the pressure is raised. Instead there is a smooth change in alignment with pressure, and this behaviour is not affected by the temperatures we can simulate. The fluctuations in the middle eigenvalue, $\langle -2\lambda_0 \rangle$, are smaller than those of the largest eigenvalue, $\langle \lambda_1 \rangle$, and, given the statistics of the simulations, indicate that the order parameter is indistinguishable from zero.

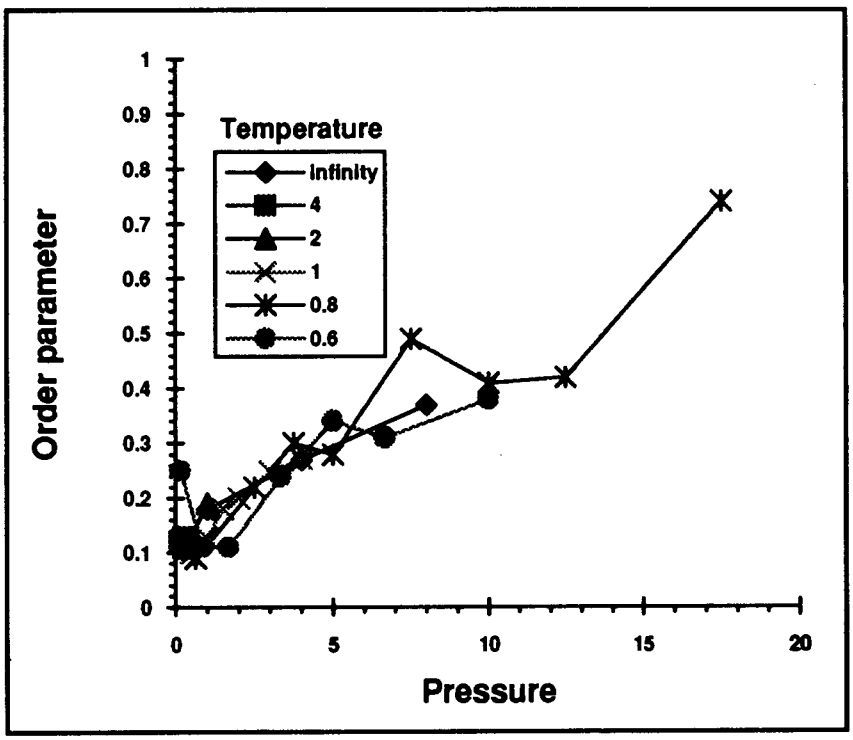

Figure 2.15 Nematic order parameter $\langle \lambda_1 \rangle$ of the disks against pressure $\beta p R^2$ at all temperatures $\left(\beta g_f R^2\right)^{-1}$ considered. The remaining parameters are as for Fig. 2.11.

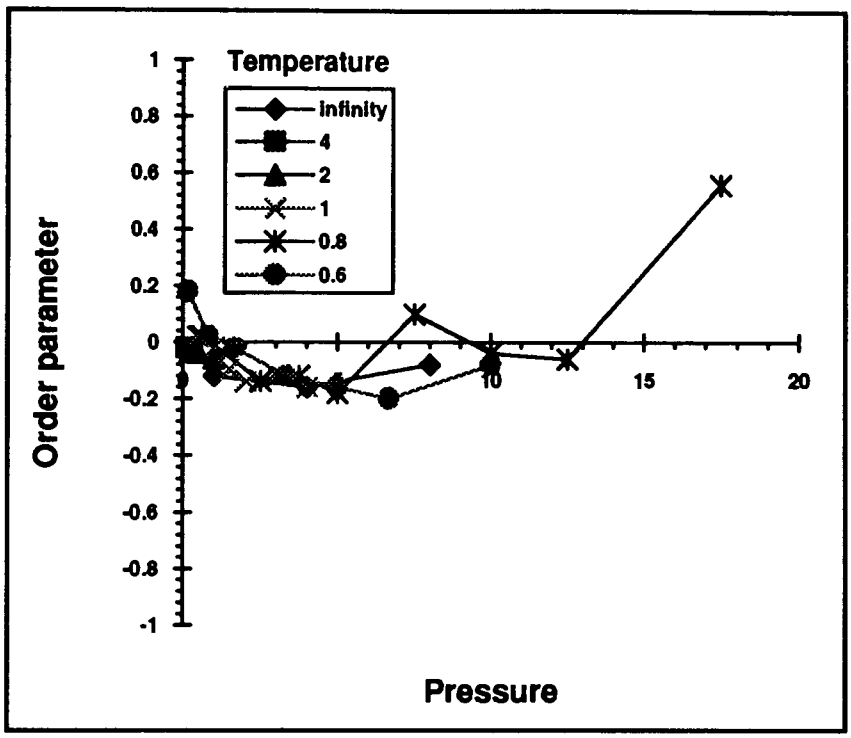

Figure 2.16 Nematic order parameter $\langle -2\lambda_0 \rangle$ of the disks against pressure $\beta p R^2$ at all temperatures $(\beta g_f R^2)^{-1}$ considered. The remaining parameters are as for Fig. 2.11.

2.6 Discussion

2.6.1 Isotropic/Nematic transition in 3D

We have used various definitions of a nematic order parameter to investigate the phase behaviour of a set of disks interacting only through hard-core repulsion in three dimensions. The results show that hard-core repulsion is sufficient to cause an I-N transition in a system of discotic particles if they are sufficiently thin, that is, anisotropic. The I-N transition exists for disks whose thickness to radius ratio lies between 0.02 and 0.2. If the ratio exceeds 0.4 the transition is absent. The difference between systems of disks with $T/R = 0.2, 0.4$ is seen in the snapshots shown in Figures 2.17 and 2.18. These figures show a system of disks at a density just above the I-N transition density. The disks with $T/R = 0.2$ are clearly in a nematic phase. The disks with $T/R = 0.4$ seem to stack in

misaligned columns that are very resistant to breaking up on the timescale of our simulations. The reduced density at the I-N transition is $NR^3/V = 0.5$ and does not change with disk thickness from $T/R = 0.02$ to 0.2. This transition density is the same as that found by Eppenga and Frenkel (1984) for infinitely thin disks. After this work was completed, quantitatively similar results were obtained by Veerman and Frenkel (1992) on a system of cut spheres: the transition is present at a thickness to radius ratio of 0.2 but is absent at a ratio of 0.4.

Summarising the available experimental results, Chandrasekhar (1990) concluded that the presence of long, flexible hydrocarbon chains attached to the solid core of discotic molecules is necessary for the molecules to form a mesophase between the isotropic liquid and solid phases. The results of our simulations show that geometric anisotropy alone is sufficient to produce an I-N transition for rigid disks.

Previous simulations of hard disks in two (Boal and Blair, 1991) and three dimensions (Eppenga and Frenkel, 1984) have employed square and cubic periodic boundary conditions (pbc) respectively. However, it has been shown by Veerman and Frenkel (1991) that pbcs can lead to spurious stability of columnar order in a system of hard, parallel spherocylinders. Each spherocylinder is a cylindrical segment of length L and diameter D capped at each end by a hemisphere of the same diameter. The spherocylinders are restricted to remain parallel at all times but their centres of mass may translate freely in the three-dimensional simulation box. The original work by Stroobants et al. (1987) found a columnar phase for $L/D > 4$ and densities greater than 60% of the close-packed density for a system of 90 spherocylinders. Later work by Veerman and Frenkel (1991) showed that the columnar phase is only metastable for $L/D = 5$, and that it is

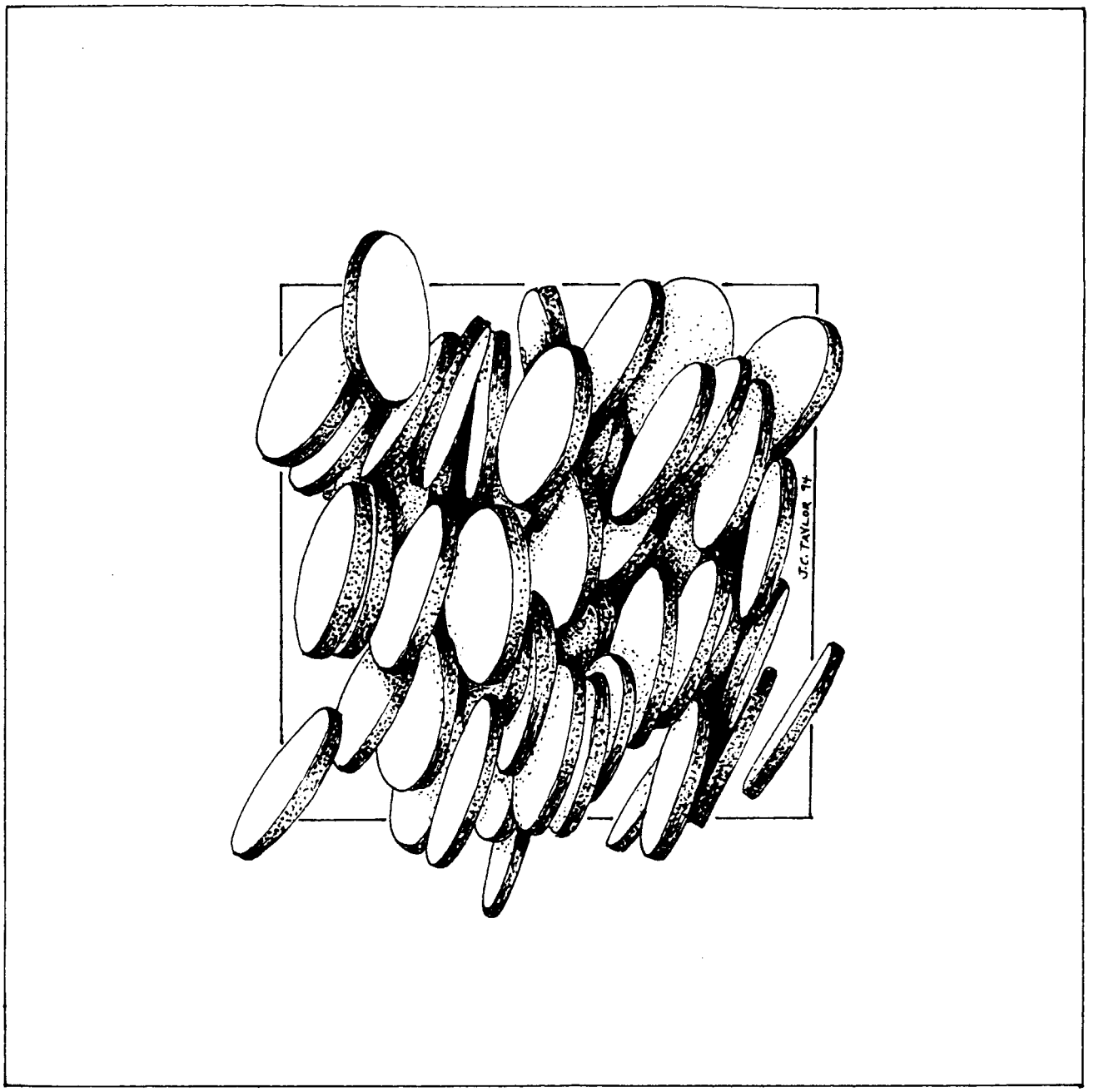

Figure 2.17 Snapshot of 100 disk system with $T/R = 0.2$ at a density of $NR^3/\langle V \rangle = 0.57$, just above the isotropic-nematic transition.

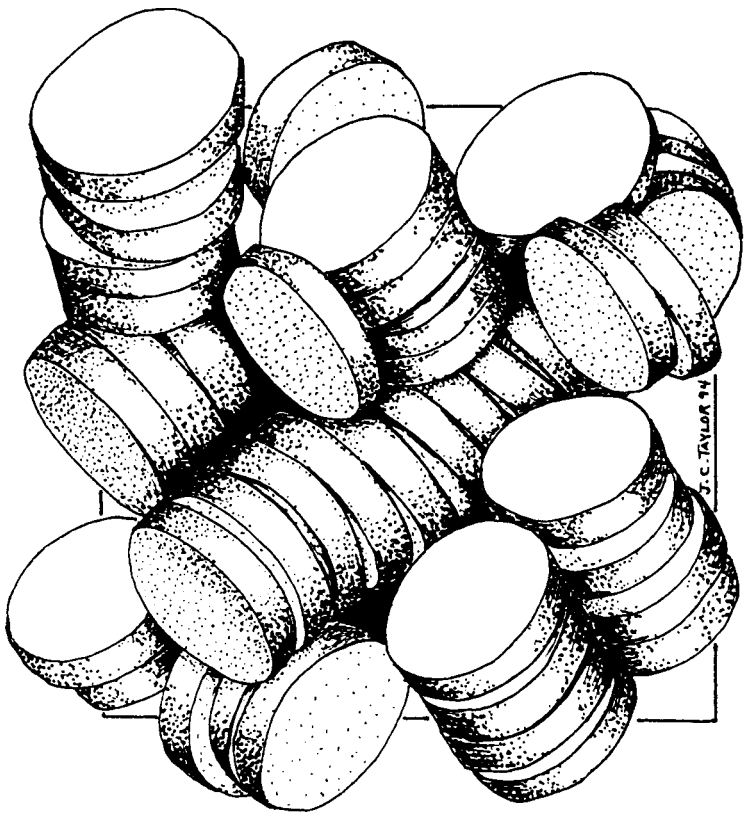

Figure 2.18 Snapshot of 100 disk system with $T/R = 0.4$ at a density of $NR^3/\langle V \rangle = 0.51$, showing the absence of nematic order.

replaced by a hexagonal crystalline phase when the system size is increased to 1080 spherocylinders. It is the combination of high density and pbcs that stabilise the columnar phase in the small system. Following Eppenga and Frenkel (1984) we have used cubic periodic boundary conditions for our study of the I-N transition in three dimensions. The density we find for the I-N transition $\left(NR^3/V = 0.5\right)$ is considerably smaller than the hexagonal-close-packed densities of 12.5 and 1.25 for disks with $T/R = 0.02, 0.2$ respectively. Because the transition density is at least a factor of three smaller than the close-packed density, we feel that the transition is not induced by the shape of the simulation cell.

2.6.2 *Isotropic/Nematic transition at an interface*

We have simulated a system of platelets each restricted to intersect a planar interface between two immiscible liquids. The platelets are differentially attracted by their faces and edge to the two liquids. They are allowed to rotate and translate in all three dimensions subject only to the restriction of intersecting the interface. The disks are defined by their thickness to radius ratio $T/R = 0.2$, and the energy scale of their interactions with the two liquids $g_e/g_f = 5$. The ground state of a single platelet with these parameters is for it to be flat at the interface.

The platelets' equation of state does not show any indication of a discontinuity in the density regime where the platelets are in close proximity. At low pressure and high temperature the mean polar angle of the disks takes the purely random value, and drops below the random value at the lowest temperature we could simulate $\left(\beta g_f R^2\right)^{-1} = 0.6$. The hard-core repulsion between the platelets causes them to align at high density with their symmetry axes in the plane of the interface. This change occurs smoothly as a function of pressure and is not indicative of a phase transition except at zero temperature.

The fraction of platelets in an upright position at a given pressure is not greatly influenced by the temperature within the range studied.

Upright disks have the possibility of ordering in a nematic phase. However, we find little evidence of a sharp onset of such ordering at finite temperature, as measured by the tensor order parameter that was useful in the three-dimensional simulations. Boal and Blair (1991) found that the upright disks became aligned in a nematic phase, but we do not see this effect. The upright disks in their simulations are effectively hard rods of equal length confined to a plane, and as such, can undergo an I-N transition. In our simulations the disks can occupy many different orientations at the interface, with some disks underlying others and preventing them from turning completely upright. This extra orientational freedom appears to prevent them from aligning in a nematic phase. Figure 2.19 shows a typical configuration of disks at the interface, and the absence of nematic order is apparent.

Finally, we mention two problems that limit the accuracy of the simulations of the platelets at an interface. The first is the fact that the free energy of a system of platelets at an interface has very narrow minima, as a function of temperature and pressure, which are difficult to sample without averaging over an impractically large number of configurations. The second problem is the long relaxation time for moving the tightly packed groups of platelets that form at high pressure and low temperature. Several platelets may be forced into a configuration with their faces parallel that is prevented from breaking up by the presence of other platelets. This configuration may be thermodynamically unstable, but still require a long simulation time before it breaks up and the platelets can move into a more stable orientation.

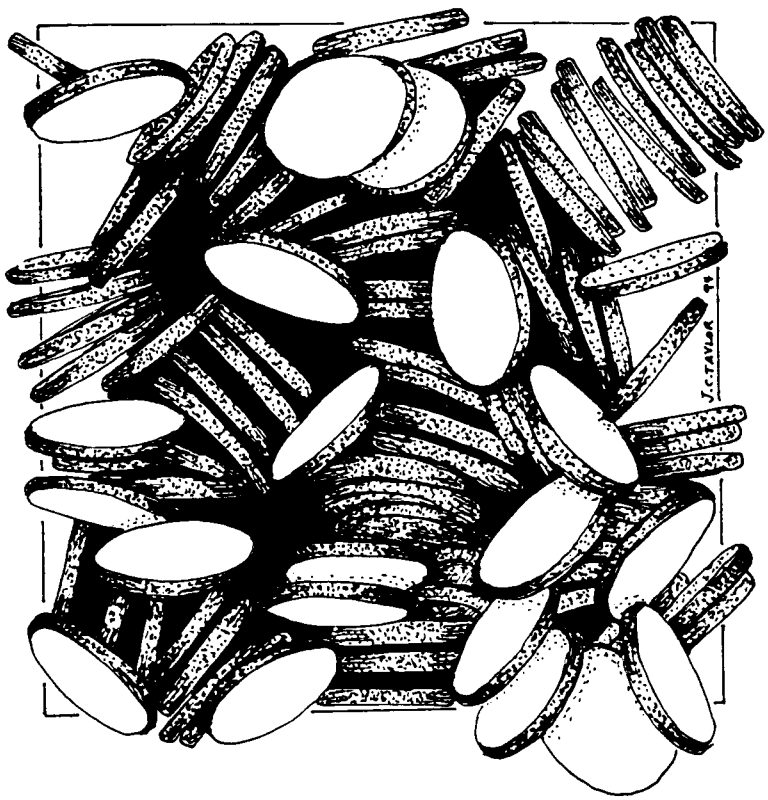

Figure 2.19 Snapshot of 100 disk system at an interface with $T/R = 0.2$ and a density of $NR^2/\langle A \rangle = 1.75$, showing the absence of nematic order.

2.7 Summary

In this chapter we have described a study of a system of hard disks in three dimensions subject to a hydrostatic pressure, and a more specialised model of hard disks constrained to intersect a flat, two-dimensional interface between two immiscible liquids.

In the 3D simulations there is no energy scale in the problem, only the effects of the anisotropic geometry of the disks and the applied pressure. Increasing the pressure on the system causes it to undergo an isotropic to nematic transition in which the disks align their symmetry axes. This transition is absent if the thickness of a disk exceeds 40% of its radius. The transition is at most weakly first-order.

In the second set of simulations the disks are constrained to intersect an interface between two immiscible fluids. The faces and edge of a disk have distinct interactions with the two fluids. This introduces an energy scale into the problem and leads to minima in the energy functional of a disk. In our model there are two such minima for a single disk: one has the disk lying in the plane of the interface, the other has it lying perpendicular to the interface.

At low temperature and zero pressure, the disks congregate in the flat state because this state has the lowest free energy for disk parameters $T/R = 0.2$ and $g_e/g_f = 5$. At low temperature and high pressure however, the disks orient themselves with their symmetry axes in the plane of the interface. The transition between the flat and upright states does not appear to be a phase transition except at zero temperature. Disks with their symmetry axes in the plane of the interface have the possibility of aligning in a nematic phase. However, we see no evidence that they form such a phase.

CHAPTER 3

POLYMERISED MEMBRANE SIMULATIONS: THEORY

3.1 Introduction

Two-dimensional surfaces occur in physical systems as diverse as biological membranes (Nelson et al. 1989; Lipowsky, 1991) and polymerised sheets of graphite oxide (Hwa et al., 1991). Fluid membranes may show large thermal undulations; solid or polymerised membranes are constrained by their connectivity to be flat. The protein skeleton attached to the cytoplasmic side of the plasma membrane in a human RBC forms a natural example of a polymerised network. The long persistence length of the fluid component of the plasma membrane restricts its out-of-plane fluctuations on length scales of a micron or less. The spectrin network has approximately two-dimensional behaviour as a result of being anchored to the fluid bilayer. The interplay of the two components gives the red cell unusual mechanical properties (Sackmann, 1990) and helps it to maintain its integrity in spite of considerable stresses that distort its shape in its passage through the capillaries of the body. In Chapters 3 and 4 we investigate the mechanical properties of polymerised sheets, such as the spectrin network confined to two dimensions.

The mechanical response of an object to external forces is embodied in a set of elastic constants or moduli (for an introduction see Landau and Lifshitz, 1959). The elastic moduli of a material are required to be positive for mechanical stability. Isotropic materials have only two independent moduli. The bulk modulus describes the object's resistance to changing its volume in response to an applied hydrostatic pressure, and the shear modulus describes its resistance to two opposing, non-collinear surface forces. An important quantity derived from the bulk and shear moduli is the Poisson ratio. It too is positive in almost all known elastic materials, although this is not required for mechanical stability.

The Poisson ratio relates the strain in a transverse direction to a stress applied longitudinally. A positive value means that the material contracts transversely when stretched longitudinally; a material with a negative Poisson ratio expands transversely when stretched longitudinally.

Recently, materials with negative Poisson ratios have been fabricated in laboratories (Evans and Caddock, 1989; Evans and Alderson, 1992). These materials, mainly foams and low density plastics, have been labelled auxetics. Although auxetic materials currently have low density and small elastic moduli (compared to rubber, for example), Evans has postulated (1991) that materials can be produced with the shear modulus much larger than the bulk modulus. One of the techniques used to produce plastics with a negative Poisson ratio, and a consequent increase in shear modulus at fixed compression modulus, is to process the material so that it has a microstructure which causes it to expand transversely when stretched (Caddock and Evans, 1989). Evans proposes (1991) that changing the molecular structure of an auxetic material or changing its microstructure on the scale of microns will produce materials with large negative Poisson ratios.

The cytoskeleton that underlies the plasma membrane in a human RBC has the form of an approximately hexagonally-connected polymerised network of proteins (Steck, 1989; Alberts et al., 1989). An RBC has a small (bulk) shear modulus (Evans et al., 1976) that is probably due to the cytoskeleton. A recent MC investigation of a model of the RBC bilayer with its associated spectrin network (Boal et al., 1992) confirmed an earlier proposal by Evans (1973) that the structural properties of the cell are determined by an interplay of the fluid bilayer and the spectrin network. This work also showed that the spectrin network under tension can exhibit a negative Poisson ratio.

The statistical mechanics of two-dimensional surfaces has been investigated for some time (see Frölich, 1985, for references). A simple model of a surface with fixed

connectivity, called the tethered net model, was introduced by Kantor, Kardar and Nelson (1986). A 2D tethered network without self-avoidance (or phantom network) embedded in three dimensions shows a phase transition from a low temperature flat phase to a high temperature crumpled phase (Kantor and Nelson, 1987). A self-avoiding tethered network shows no such transition (Plischke and Boal, 1988; Lipowsky and Girardet, 1990).

Here we investigate a triangulated, tethered network of Hooke's law springs, with and without the self-avoidance constraint, subject to an applied stress. We determine the temperature and stress dependence of the model's elastic properties. In the remainder of this chapter we derive results from elasticity theory for the elastic moduli of two-dimensional sheets. We then present a mean-field-theory calculation of the elastic moduli of a triangulated network of Hooke's law springs. This theory allows us to understand some of the behaviour of the network, although, as we shall see in Chapter 4, both self-avoiding and phantom networks have features that cannot be explained within mean field theory.

3.2 Elasticity in two dimensions

3.2.1 Elastic constants and stress-strain relations

Suppose, in the absence of external forces, a body is in a state of mechanical equilibrium. Under the action of an applied force, stresses are set up within the body that try to return it to its equilibrium state. We describe the deformation of a body under stress, using the approach and notation of Landau and Lifshitz (1959), and initially work in three dimensions before deriving the results needed for tethered networks in two dimensions. Consider an arbitrary body embedded in 3D. Let the coordinates of a point in the body be x_i, i=1,2,3. When forces are applied to the body they result in a strain and each point of the body moves to a new equilibrium position x_i'. Consider also another point close to x_i, $x_i + dx_i$, which is shifted to $x_i' + dx_i'$. The displacement field is defined by

$$u_i = x_i' - x_i, \tag{3.1}$$

and obviously $dx_i' = dx_i + du_i$, where $du_i = \frac{\partial u_i}{\partial x_k} dx_k$. We employ the summation convention that repeated indices are summed over the number of space dimensions. The distances between the two points before and after the stress is applied are

$$\begin{aligned} dl^2 &= dx_i^2, \\ dl'^2 &= dx_i'^2 = (dx_i + du_i)^2. \end{aligned} \tag{3.2}$$

Expanding Eq.(3.2) gives

$$dl'^2 = dl^2 + 2\left(\frac{\partial u_i}{\partial x_k}\right) dx_i dx_k + \left(\frac{\partial u_i}{\partial x_k}\right)\left(\frac{\partial u_i}{\partial x_l}\right) dx_k dx_l, \tag{3.3}$$

which can be rewritten as

$$dl'^2 = dl^2 + 2u_{ik} dx_i dx_k, \tag{3.4}$$

where $u_{ik} = \frac{1}{2}\left(\frac{\partial u_i}{\partial x_k} + \frac{\partial u_k}{\partial x_i} + \frac{\partial u_l}{\partial x_i}\frac{\partial u_l}{\partial x_k}\right)$ is the strain tensor. It is clear that the strain tensor is a symmetric second-rank tensor.

Consider an homogeneous body in equilibrium at a given temperature. We can expand its free energy as a series of positive powers of the strain tensor u_{ik}. To avoid spontaneous deformations there can be no term linear in u_{ik}. The free energy is a scalar and we have to build it out of the second-rank tensor u_{ik}. There are only two independent second-order invariants that can be constructed for an isotropic material, so the free energy must have the form

$$F - F_0 = \tfrac{1}{2}\lambda u_{ii}^2 + \mu u_{ik}^2, \tag{3.5}$$

where $u_{ii}^2 = \left(\sum_i u_{ii} \right)^2$ and $u_{ik}^2 = \sum_{ik} u_{ik}^2$. The two constants λ, μ are called Lamé coefficients. The free energy density in the unstrained state is F_0. It may be shown that μ is the shear modulus of the body.

The stress tensor is defined as the derivative of the free energy of the body with respect to the strain tensor, and has the units of energy density,

$$\sigma_{ik} = \frac{\partial F}{\partial u_{ik}}. \tag{3.6}$$

If there are no external forces on the body the stress tensor is zero, and the strain tensor is likewise zero. An alternative definition of the stress tensor that is useful is the following. Consider a small element of surface on a body. Let the normal to this area element be n_j. The stress tensor σ_{ij} is the ith component of the force per unit area acting in the jth direction of the normal to the surface, so the force on the area element is $\sigma_{ij} n_j$. For example, a hydrostatic compression exerts the same pressure on all surface elements of a body. Hence, $\sigma_{ik} dA_k$ is the force on area element dA_k. But by definition this must equal $-p dA_i$. Thus, in this case,

$$\sigma_{ik} = -p\delta_{ik}. \tag{3.7}$$

We want to find relations among the elastic constants using the stress and strain tensors. Later we will use a microscopic model to predict the values of the elastic constants. In two dimensions we can rewrite Eq. (3.5) as

$$F - F_0 = \tfrac{1}{2} K u_{ll}^2 + \mu \left(u_{ik} - \tfrac{1}{2} u_{ll} \delta_{ik} \right)^2. \tag{3.8}$$

where the area compression modulus $K = \lambda + \mu$. Taking the total differential of this equation and comparing this with Eq. (3.6), we obtain the stress tensor in terms of the strain tensor

$$\sigma_{ik} = K u_{ll}\delta_{ik} + 2\mu\left(u_{ik} - \tfrac{1}{2} u_{ll}\delta_{ik}\right). \tag{3.9}$$

Equation (3.9) may be inverted to give the components of the strain tensor in terms of the stress tensor. We find

$$u_{ik} = \frac{1}{2\mu}\left[\sigma_{ik} - \tfrac{1}{2}\sigma_{ll}\delta_{ik}\right] + \frac{\sigma_{ll}\delta_{ik}}{4K}. \tag{3.10}$$

We can derive relationships among the various elastic constants using Eqs. (3.9) and (3.10). The Young's modulus is defined as the longitudinal stress over the longitudinal strain which, in two dimensions, becomes

$$Y = \frac{\sigma_{11}}{u_{11}} = \frac{4K\mu}{K+\mu}, \tag{3.11}$$

and the Poisson ratio is the transverse strain divided by the longitudinal strain,

$$\sigma = -\frac{u_{22}}{u_{11}} = \frac{K-\mu}{K+\mu}. \tag{3.12}$$

3.2.2 Elastic constants and thermal fluctuations

An MC simulation allows us to calculate ensemble averages and fluctuations of observables. An ensemble average calculated from the exact partition function is approximated by a finite weighted sum over the sample configurations generated by the simulation (see Appendix A for details of the MC procedure). The observables we are interested in are the length and breadth of the Hooke's law spring network. The fluctuations in these quantities are a measure of the response of the network to an applied stress. In the next chapter we extract the network's elastic moduli from the fluctuations of observables, instead of using numerical derivatives, for reasons of simplicity. Our derivation of the elastic constants from the fluctuations in the box shape at constant pressure follows that of Lipowsky and Girardet (1990).

Let L_x, L_y be the equilibrium values of the box lengths in the x and y directions. We define a small change in the lengths by

$$\begin{aligned} L_x' &= L_x(1+\Delta L_x), \\ L_y' &= L_y(1+\Delta L_y). \end{aligned} \tag{3.13}$$

The strain tensor, in this case a two-dimensional matrix, has the simple form,

$$u = \begin{pmatrix} \Delta L_x & 0 \\ 0 & \Delta L_y \end{pmatrix}, \tag{3.14}$$

and the free energy density, Eq. (3.5), is given by

$$\Delta F = \frac{1}{2}\lambda\left(\Delta L_x + \Delta L_y\right)^2 + \mu\left(\Delta L_x{}^2 + \Delta L_y{}^2\right). \tag{3.15}$$

The partition function and the results of the relevant averages of the fluctuations in the box sides are:

$$\begin{aligned} Z &= \frac{C\,\pi}{\beta\langle A\rangle\sqrt{\mu(\lambda+\mu)}}, \\ \langle \Delta L_x\rangle &= \langle \Delta L_y\rangle = 0, \\ \langle \Delta L_x{}^2\rangle &= \langle \Delta L_y{}^2\rangle = \frac{K+\mu}{4\beta\langle A\rangle K\mu}, \\ \langle \Delta L_x \Delta L_y\rangle &= \frac{\mu - K}{4\beta\langle A\rangle \mu K}, \end{aligned} \tag{3.16}$$

where $\beta = 1/k_B T$, k_B is Boltzmann's constant, T is the temperature, and C is a normalisation constant. The Young's modulus and shear modulus may be found from these equations and Eq. (3.11):

$$Y = \frac{4K\mu}{K+\mu} = \frac{1}{\beta\langle A\rangle\langle \Delta L_x{}^2\rangle} = \frac{1}{\beta\langle A\rangle\langle \Delta L_y{}^2\rangle}, \tag{3.17}$$

$$\mu = \frac{K\overline{Y}}{4K - \overline{Y}}. \tag{3.18}$$

Note that we have used the average $(\overline{Y})$ of the Young's modulus in the x and y directions in the calculation of the shear modulus.

The bulk modulus is obtained by considering fluctuations of the box sides about their equilibrium values. The average area of the box is

$$\begin{aligned} \langle A \rangle &= \langle L_x L_y (1+\Delta L_x)(1+\Delta L_y) \rangle \\ &= A_0 (1+\langle \Delta L_x \Delta L_y \rangle), \end{aligned} \tag{3.19}$$

where the quantity A_0 differs from $\langle A \rangle$ by a term that decreases with $\langle A \rangle$. Similarly the average square of the area is given by

$$\langle A^2 \rangle = A_0^2 (1+4\langle \Delta L_x \Delta L_y \rangle + \langle \Delta L_x{}^2 \rangle + \langle \Delta L_y{}^2 \rangle), \tag{3.20}$$

where we have ignored terms higher than second-order. Hence we obtain

$$\langle A^2 \rangle - \langle A \rangle^2 = A_0^2 [2\langle \Delta L_x \Delta L_y \rangle + \langle \Delta L_x{}^2 \rangle + \langle \Delta L_y{}^2 \rangle]. \tag{3.21}$$

The bulk modulus is obtained from Eqs. (3.16) and (3.21), replacing A_0 by $\langle A \rangle$:

$$\beta K = \frac{\langle A \rangle}{\langle A^2 \rangle - \langle A \rangle^2}. \tag{3.22}$$

The Poisson ratio is determined from the bulk and shear moduli using Eq. (3.12). The bulk modulus may alternatively be obtained from the relation, $K^{-1} = \frac{-1}{\langle A \rangle} \frac{\partial \langle A \rangle}{\partial P}$, via a numerical derivative of the equation of state obtained from the simulation.

3.3 Mean field theory calculation of elastic properties

We now use a mean-field approach to gain insight into the behaviour of an hexagonally-connected, tethered network of Hooke's law springs subject to an external stress. Let there be N vertices in the network and let the unstretched length of the springs be s_h. The energy contained in a single spring is given by Hooke's law

$$V(s_{ij}) = \frac{1}{2}k\left|s_{ij} - s_h\right|^2, \qquad 0 < \left|s_{ij}\right| < \infty, \tag{3.23}$$

where k is the spring constant and s_{ij} is the length of the spring connecting vertices i and j. In mean field theory we assume that all springs have the same length s, so that the energy per vertex of the network is $E_V = \frac{3}{2}k(s - s_h)^2$, and the area per vertex is $A_V = \frac{\sqrt{3}}{2}s^2$. The network can then be tiled by plaquettes, each containing a single vertex. The plaquettes have the shape of a rhombus with side length s and interior angles of 60° or 120°.

We calculate the thermodynamic properties of the network by considering a single plaquette (or parallelogram) described by the mean energy and area E_V and A_V. A plaquette with area A_V has a Boltzmann weight $\exp(-\beta E_V)$. But the plaquettes can take on all positive values of A_V, so the partition function for the ensemble of plaquettes is

$$Z = C\int_0^\infty e^{-\beta p A_V} . e^{-\beta E_V}\, dA_V, \tag{3.24}$$

where C is a normalisation constant. This may be rewritten as

$$Z = C\int_0^\infty e^{-\beta H}\, dA_V, \tag{3.25}$$

where the enthalpy per plaquette is

$$\beta H = \frac{3}{2}\beta k\left[(s - s_h)^2 + \frac{p}{\sqrt{3}k}s^2\right]. \tag{3.26}$$

The area element dA can be replaced by an integral over the length $\sqrt{3}sds$. The result for the partition function of the plaquettes is

$$Z = \sqrt{3}C\, e^{-\frac{3}{2}\beta k\bar{p}(1+\bar{p})\bar{s}^2}\left[\bar{s}\sqrt{\frac{2\pi}{3\beta k(1+\bar{p})}} + \frac{2}{3\beta k(1+\bar{p})}e^{-\frac{3}{2}\beta k(1+\bar{p})\bar{s}^2} + 2\bar{s}\int_0^{\bar{s}} e^{-\frac{3}{2}\beta k(1+\bar{p})y^2}dy\right], \tag{3.27}$$

where $\bar{p} = \frac{p}{\sqrt{3}k}$, and $\bar{s} = \frac{s_h}{1+\bar{p}}$. We may also calculate expressions for the mean spring length s_p and its dispersion Δs_p^2. These are complicated functions of the unstretched spring length and pressure; but in the limit of low temperature or large stretching pressure, they reduce to the following simple forms:

$$\begin{aligned} s_p &= \langle s\rangle = \frac{s_h}{1+\bar{p}} + \frac{1}{3\beta k s_h} + \cdots, \\ \Delta s_p^2 &= \langle s^2\rangle - \langle s\rangle^2 = \frac{1}{3\beta k(1+\bar{p})} + \cdots. \end{aligned} \tag{3.28}$$

Equation (3.28) shows that the network has an instability for a finite, negative value of the pressure. When $p/k = -\sqrt{3}$ the network expands without limit. The higher order terms in Eq. (3.28) contain exponentials of the form $\exp\left(-\frac{3}{2}\beta k(1+\bar{p})\bar{s}^2\right)$ and cannot remove the singularity at $p/k = -\sqrt{3}$.

We can now derive a criterion for the applicability of the mean field theory (MFT hereafter) in describing the network's behaviour. The derivation leading up to Eq. (3.28) assumes that all springs in the network have the same length. We expect this approximation to be accurate when the dispersion in the spring length is small compared to the stretched equilibrium value. This condition is

$$\frac{\Delta s_p^2}{s_p^2} << 1,$$

or

$$\frac{1}{3}\left(1+\frac{p}{\sqrt{3}k}\right)\frac{k_BT}{ks_h^2}<<1. \tag{3.29}$$

This shows that the MFT is accurate at low temperatures, $k_BT/ks_h^2 << 1$, or in the limit $p/\sqrt{3}k \to -1$.

Next we calculate the enthalpy of deformation of a network composed of equal length springs and extract the elastic moduli for the network. We consider two deformations: a pure compression and a simple (area-preserving) shear. In this way both moduli are derived using similar procedures.

Compression Modulus

Consider a network of equilateral triangles with the length of side of each triangle stretched by a uniform amount, $s_p \to (1+\varepsilon)s_p$. The enthalpy per vertex of the network initially is

$$\beta H=\frac{3}{2}\beta k\left[\left(s_p-s_h\right)^2+\frac{p}{\sqrt{3}k}s_p^2\right], \tag{3.30}$$

and the enthalpy change of the deformation is

$$\Delta H = H(\varepsilon)-H(0)=\tfrac{3}{2}k\varepsilon^2\left(1+\frac{p}{\sqrt{3}k}\right)s_p^2.$$

The area per vertex of the network is $\frac{\sqrt{3}}{2}s_p^2$, so the enthalpy density Δh for the deformation is

$$\Delta h=\sqrt{3}k\varepsilon^2\left(1+\frac{p}{\sqrt{3}k}\right).$$

This may be compared with the general result from Eq. (3.8), $\Delta F = 2K\varepsilon^2$, obtained by setting $u_{11} = u_{22} = \varepsilon$, and $u_{12} = u_{21} = 0$. Hence the compression modulus is

$$K = \tfrac{\sqrt{3}}{2} k\left(1 + \frac{p}{\sqrt{3}k}\right). \tag{3.31}$$

Shear Modulus

Consider a small, area-preserving shear of a triangle with $\varepsilon << s_p$, as shown in Fig 3.1 below.

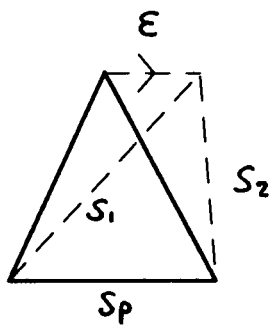

Figure 3.1 Simple shear for an equilateral triangle. One vertex is moved parallel to the opposite side by an amount that is small compared to the original side length.

The enthalpy per vertex of the network before the shear is again given by Eq. (3.30) and after the shear it is

$$H(\varepsilon) = \tfrac{1}{2}k(s_p - s_h)^2 + \tfrac{1}{2}k(s_1 - s_h)^2 + \tfrac{1}{2}k(s_2 - s_h)^2 + \frac{\sqrt{3}p}{2k}s_p^2,$$

where

$$s_1^2 = s_p^2 + \varepsilon^2 s_p^2 - 2\varepsilon s_p^2 \cos 120,$$
$$s_2^2 = s_p^2 + \varepsilon^2 s_p^2 - 2\varepsilon s_p^2 \cos 60.$$

This corresponds to an enthalpy change

$$\Delta H = H(\varepsilon) - H(0) = \frac{1}{4} k\varepsilon^2 s_p^2 \left(1 - \frac{\sqrt{3}p}{k}\right).$$

The enthalpy density per vertex is then

$$\Delta h = \tfrac{1}{2\sqrt{3}} k\varepsilon^2 \left(1 - \frac{\sqrt{3}p}{k}\right),$$

and, comparing this with the general form, $\Delta F = \frac{2}{3}\mu\varepsilon^2$, obtained from Eq. (3.8) by setting $u_{12} = u_{21} = \varepsilon/\sqrt{3}$, and $u_{11} = u_{22} = 0$, gives the result,

$$\mu = \frac{\sqrt{3}k}{4}\left(1 - \frac{\sqrt{3}p}{k}\right). \qquad (3.32)$$

Poisson Ratio

Finally we calculate the Poisson ratio from the two moduli just derived. It is defined in terms of K, μ in Eq. (3.12). Substituting the expressions above gives

$$\sigma = \frac{1 + 5\frac{p}{\sqrt{3}k}}{3 - \frac{p}{\sqrt{3}k}}. \qquad (3.33)$$

We show the behaviour of the elastic constants and Poisson ratio as a function of pressure in Figure 3.2. For later reference we also show how they vary with the area per vertex in Figure 3.3.

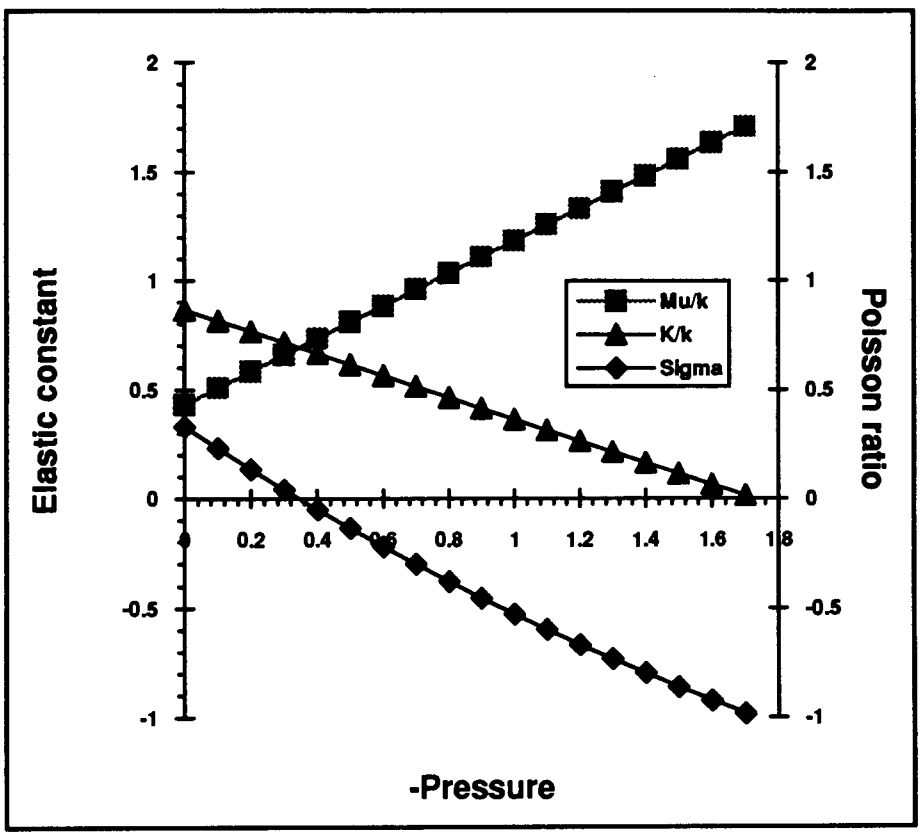

Figure 3.2 MFT predictions for compression modulus K/k, shear modulus μ/k, and Poisson ratio σ of a 2D network of Hooke's law springs as a function of the pressure p/k on the network. Note that a negative pressure stretches the network, and the network expands without limit at a pressure of $p/k = -\sqrt{3}$.

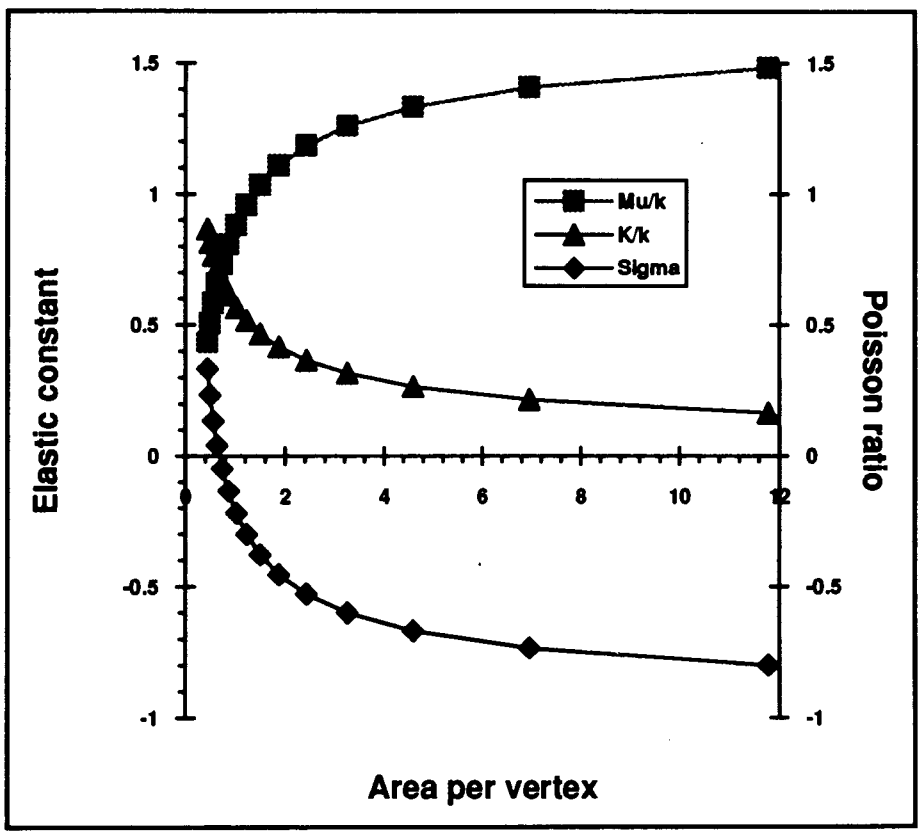

Figure 3.3 MFT predictions for compression modulus K/k, shear modulus μ/k, and Poisson ratio σ of a 2D network of Hooke's law springs as a function of the normalised area per vertex A/Ns_h^2.

3.4 Summary

In this chapter we have investigated a network of Hookean springs confined to two dimensions. We have derived results for the elastic constants of the network from elasticity theory and from the fluctuations of observables that can be obtained from a Monte Carlo simulation.

The network has a temperature scale set by the combination ks_h^2/k_B, where k is the Hooke's law spring constant and s_h is the unstretched spring length. The network is subject to an applied pressure p/k. We have shown how the bulk and shear moduli of the network may be calculated from fluctuations in its size. The Poisson ratio for the network is derived from these two moduli and relates the transverse strain to a stress applied longitudinally. The Poisson ratio of a material is usually positive, although this is not required for stability. Materials have recently been produced that have negative Poisson ratios. This means that they expand transversely when stretched longitudinally.

We have introduced a mean field theory of a network of Hookean springs that allows us to calculate the network's behaviour, and its elastic constants, as a function of the temperature and pressure. The mean field theory predicts that the network expands without limit when the applied pressure satisfies $p/k \le -\sqrt{3}$. In the limit of low temperature, $k_BT/ks_h^2 << 1$, or as the pressure $p/\sqrt{3}k \to -1$, the average spring length and its dispersion take on simple forms. It is only in these limits that the mean field theory is accurate. The elastic moduli are calculated from small deformations of the network and show that the bulk modulus vanishes at the singular pressure $p/\sqrt{3}k = -1$. The Poisson ratio is predicted to be negative for all pressures below $p/k = -\sqrt{3}/5 \approx -0.35$.

CHAPTER 4

POLYMERISED MEMBRANE SIMULATIONS: RESULTS

4.1 Introduction

Two-dimensional spring networks have been extensively investigated in the context of percolation theory (Feng and Sen, 1984) and elasticity (Thorpe and Garboczi, 1990). Feng, Thorpe and Garboczi (1985) studied the elastic properties of a network when a fraction of the bonds is removed, the so-called random network. Tang and Thorpe (1988) examined the elastic properties of random networks under an applied tension. The percolation threshold and the behaviour of the elastic constants of the network near this threshold were investigated. A surprising result obtained by Thorpe and Garboczi (1990) is that a regular network of Hooke's law springs appears to form pleats, as parts of the network overlap, when the strain is large. They examined a network of springs with two different natural lengths, confined to two dimensions with no applied tension. When the natural lengths differed by 50%, sections of the network overlapped as nearest-neighbour bonds crossed each other. This pleating occurred suddenly, and the properties of the network showed no anticipation of the change.

In this chapter we present results for the elastic properties of a regular, triangulated network of Hooke's law springs subject to an applied tension. Our results are derived within the constant-pressure ensemble and are complementary to the above work, which was carried out on free networks, or within the constant-area ensemble. The bonds in our network are flexible springs with a Hooke's law potential energy function,

$$V(s_{ij}) = \frac{1}{2} k \left| s_{ij} - s_h \right|^2 \qquad 0 < \left| s_{ij} \right| < \infty, \tag{4.1}$$

where k is the spring constant, s_h is the unstretched spring length and s_{ij} is the distance between vertices i and j. There is no maximum length to the springs. The networks are subject to an applied pressure and we investigate their elastic properties using Monte Carlo simulations in the NPT ensemble. In these simulations the lengths of the x and y dimensions of the network are changed independently, and the elastic moduli of the network are obtained from fluctuations in the box side lengths. In the results that follow, we consider s_h to set the length scale and express the temperature in the dimensionless combination, $k_B T/ks_h^2$, and the pressure as p/k. For the rest of this chapter the pressure on the networks is restricted to the range $p/k = 0$ to $-\sqrt{3}$, corresponding to a network under tension.

Consider a rectangular patch of N vertices connected by $3N$ springs cut from a triangulated network and confined to two dimensions. A typical snapshot of a stretched, regular network is shown in Figure 4.1. We first present results for self-avoiding networks, in which the springs are constrained not to intersect each other; later we remove the self-avoidance constraint and consider networks in which the springs can cross, the so-called phantom networks. In order to reduce the influence of the edges of the network, periodic boundary conditions are used. The essence of the constant pressure MC method is to make small random changes in the variables of interest, here, the positions of the vertices and the lengths of the box sides, and to assign a pseudo-Boltzmann weight to the resulting configuration. This weight ensures that the configurations generated by the MC method are distributed according to the equilibrium probabilities of the canonical ensemble. The interesting network observables are obtained from the configurations and used to construct thermodynamic averages. The NPT ensemble allows us to set the pressure and extract the area of the system as an ensemble average. The technical details of the simulations are described in Appendix B, where we also describe the error analysis for the simulations.

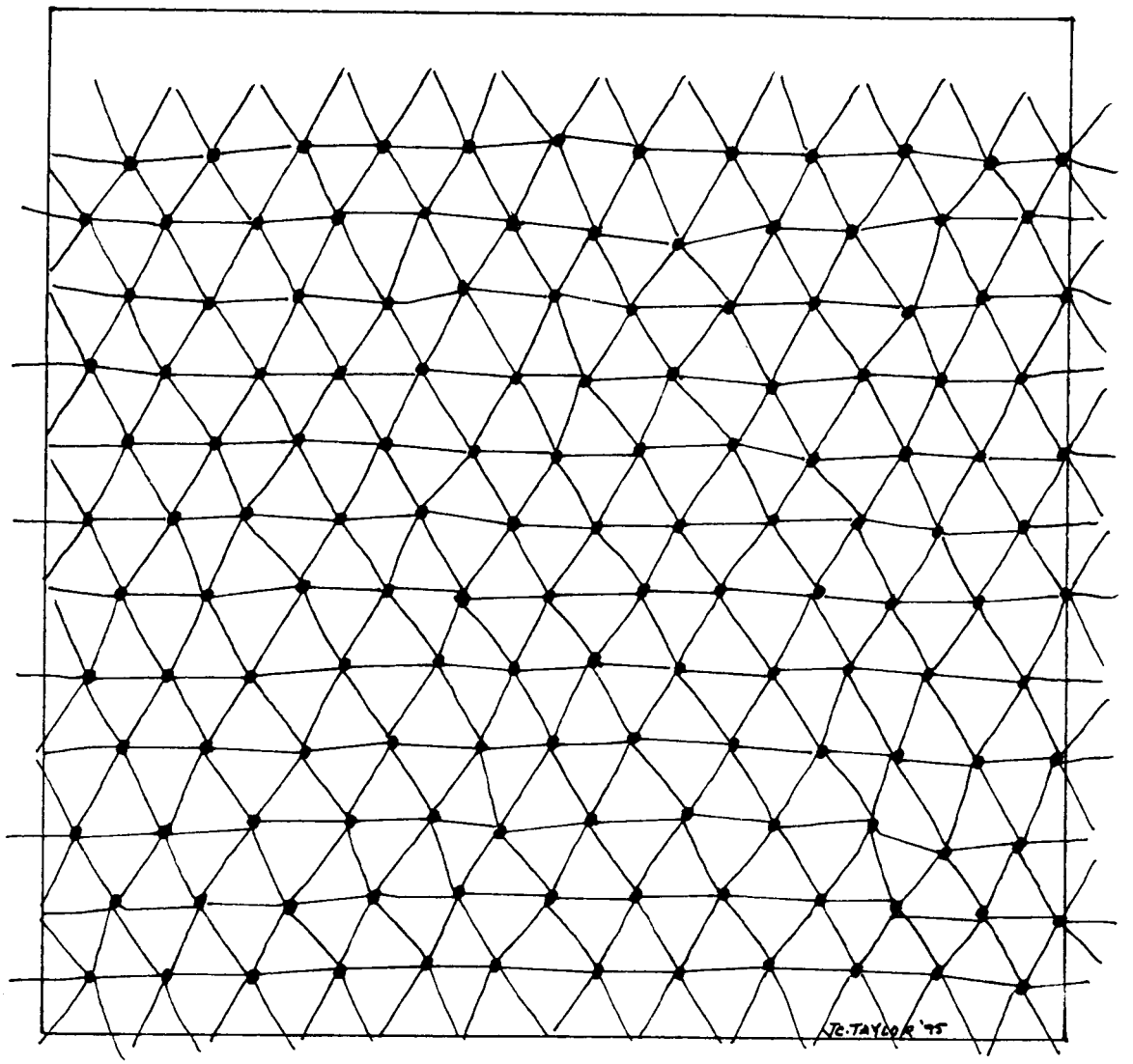

Figure 4.1 Stretched Hooke's law network at a pressure $p/k = -1.5$. The temperature is $k_B T/ks_h^2 = 1$, and the average spring length is $\langle s \rangle / s_h = 7.5$. The network shown has $N = 144$ vertices.

4.2 Self-Avoiding Hooke's law network

We examine first the mean area per vertex, $\langle A \rangle / N s_h^2$, of the self-avoiding (SA) Hooke's law network. This is shown in Fig. 4.2 for the range of temperatures simulated[1], together with the zero-temperature mean-field-theory[2] (MFT) prediction from Section 3.3 for comparison.

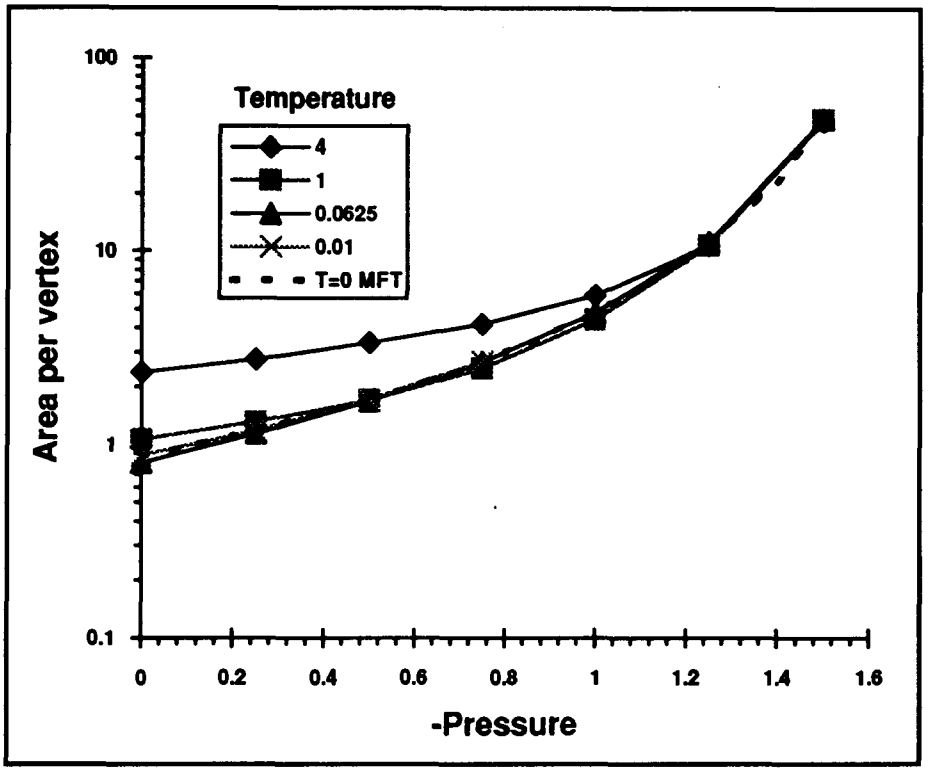

Figure 4.2 Area per vertex $\langle A \rangle / N s_h^2$ against pressure p/k for self-avoiding Hooke's law network at several temperatures $k_B T / k s_h^2$. $N = 144$ vertices. The T=0 MFT prediction from Eq. (4.2) is shown for comparison.

[1]We have omitted the curve for infinite temperature as it cannot be normalised to appear in this graph.
[2]In the rest of this chapter we identify the zero temperature mean field results by the abbreviation T=0 MFT.

The MFT of Chapter 3 predicts that the area per vertex, scaled by the unstretched spring length $\langle A \rangle / N s_h^2$, should increase with tension (negative pressure) at constant temperature. Mean field theory also predicts that the area per vertex should increase with temperature at constant pressure. These results follow from Eq. (3.28) and are both seen in Fig. 4.2. At the highest temperature simulated, $k_B T / k s_h^2 = 4$, there is a significant deviation of the area per vertex from the T=0 MFT prediction except for pressures $p/k < -1.2$. At the temperature $k_B T / k s_h^2 = 1$ the simulation agrees with the T=0 MFT prediction except for pressures $p/k > -0.3$. These deviations agree with Eq. (3.28), where the first correction term to the average spring length grows with the temperature. Recalling Eq. (3.28)

$$\frac{s_p}{s_h} = \frac{\langle s \rangle}{s_h} = \frac{1}{1+\bar{p}} + \frac{k_B T}{3 k s_h^2} + \cdots, \tag{3.28}$$

from which the area per vertex is

$$\frac{\langle A \rangle}{N s_h^2} = \frac{\sqrt{3} s_p^2}{2 s_h^2} = \frac{\sqrt{3}}{2(1+\bar{p})^2} + \frac{k_B T}{\sqrt{3} k s_h^2 (1+\bar{p})} + \cdots. \tag{4.2}$$

Figure 4.2 and Eq. (4.2) show that finite-temperature corrections to the T=0 MFT result become irrelevant when the networks are highly stretched, that is, as $p/k \to -\sqrt{3}$. The instability of the network at $p/k = -\sqrt{3}$ predicted by MFT is also seen in Fig. 4.2[3]. The area per vertex is predicted to increase to infinity by Eq. (4.2) when $p/k = -\sqrt{3}$, and this behaviour appears in the simulations.

The average spring length is shown in Fig. 4.3, and follows the zero temperature mean field prediction of Eq. (3.28) except at the highest temperature, $k_B T / k s_h^2 = 4$, which shows an obvious deviation for pressures $p/k > -1.2$. The curve at the lowest temperature $k_B T / k s_h^2 = 0.01$ agrees with the T=0 MFT curve to better than 1% in Figure

[3]Notice that the y axis scale is logarithmic in Fig. 4.2, so the area increase is steeper than it appears.

4.3. The finite-temperature MFT predicts that the average spring length should increase with temperature at fixed pressure, and this effect is also seen in Fig. 4.3.

For each configuration in the simulation, we define an average spring length, $\bar{s}$, and its standard deviation, $\sigma(\bar{s})$. The quantity $\bar{s}$ averaged over all the configurations in the simulation gives the average spring length $\langle s \rangle / s_h$ plotted in Fig. 4.3. In Fig. 4.4 we show the standard deviation of the spring length, averaged over all configurations, divided by the average spring length $\langle \sigma(\bar{s}) \rangle / \langle s \rangle$. This shows the relative spread of spring lengths within a single configuration.

This ratio approaches zero when the network is stretched at high pressure, but it

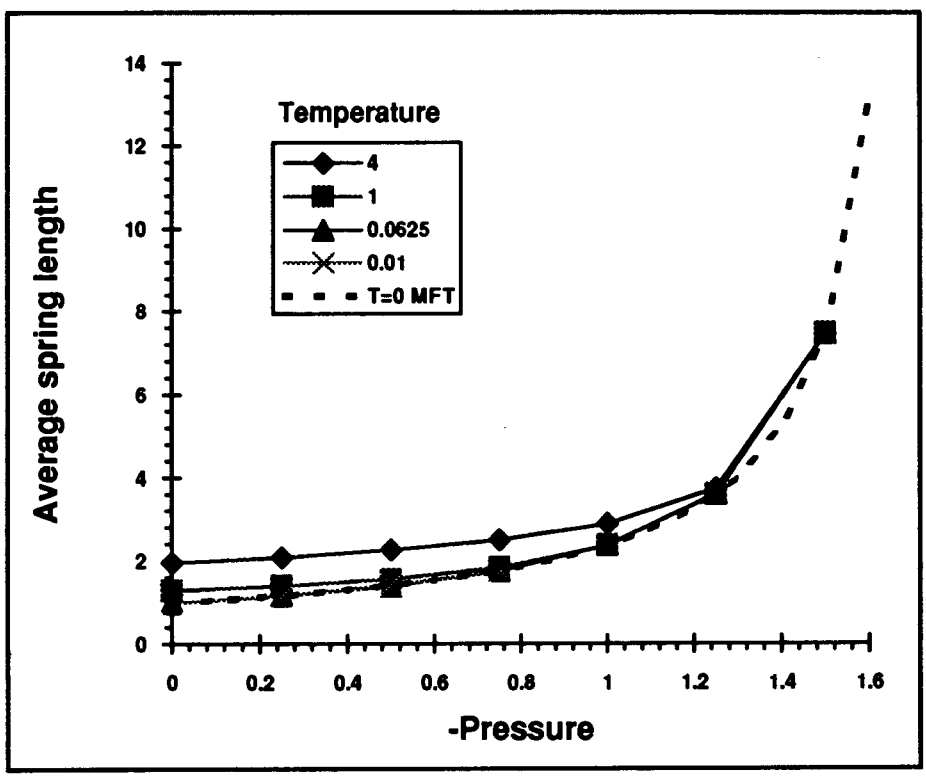

Figure 4.3 Average spring length $\langle s \rangle / s_h$ against pressure p/k for self-avoiding Hooke's law network at four temperatures $k_B T / k s_h^2$. N = 144 vertices. The T=0 MFT prediction from Eq. (3.28) is shown for comparison.

stays finite even as the pressure approaches zero. This is predicted by MFT in Eq. (3.28) of Chapter 3. However, in the simulations this ratio is also finite at infinite temperature. The low temperature mean field theory is obviously invalid at high temperatures, but Eq. (3.28) predicts that the corrections to the average spring length diverge as the temperature increases. Notice that the average spring length at infinite temperature cannot be plotted in Fig. 4.3, but that the relative standard deviation in Fig. 4.4 is well-defined.

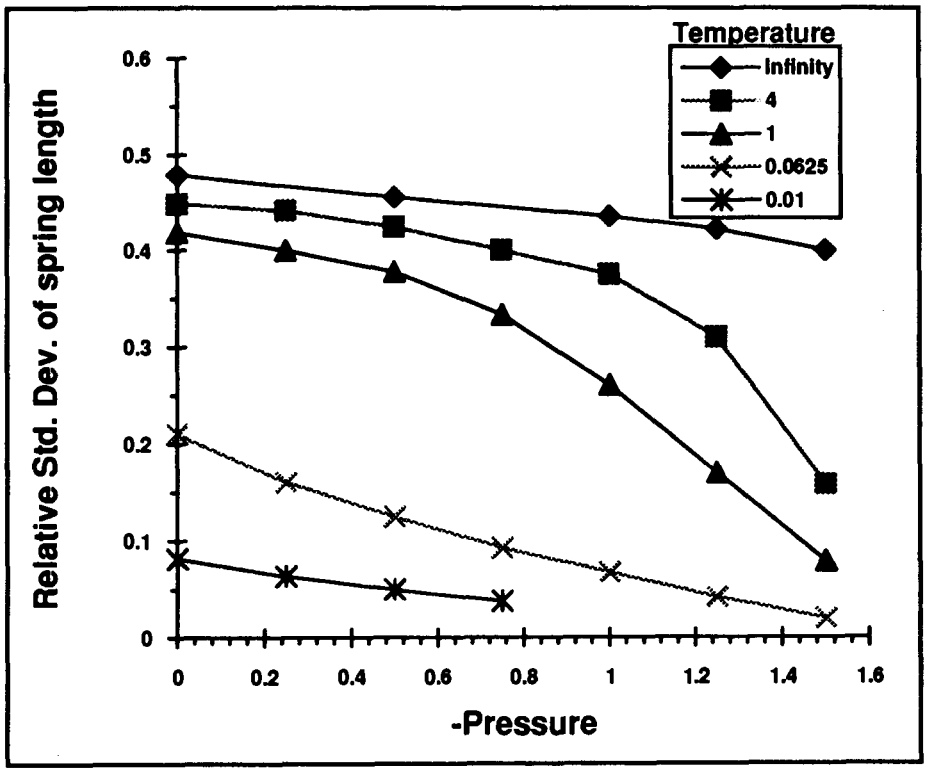

Figure 4.4 Relative standard deviation of spring length $\langle \sigma(\bar{s}) \rangle / \langle s \rangle$ against pressure p/k for self-avoiding Hooke's law network at all temperatures $k_B T / k s_h^2$ considered. N = 144 vertices.

When the lateral pressure on the network is zero, MFT predicts that the average spring length $\langle s \rangle / s_h = 1 + k_B T / 3 k s_h^2$ (see Eq. (3.28)). Figure 4.5 shows that the low-temperature simulations, $k_B T / k s_h^2 \leq 0.0625$, agree with T=0 MFT but that the simulations at temperatures $k_B T / k s_h^2 \geq 1$ do not. The discrepancy between T=0 MFT and the

simulations grows with temperature, as expected. The criterion for the low temperature MFT, Eq. (3.28), to be applicable is Eq.(3.29) which requires $k_B T/ks_h^2 << 3$ at zero pressure.

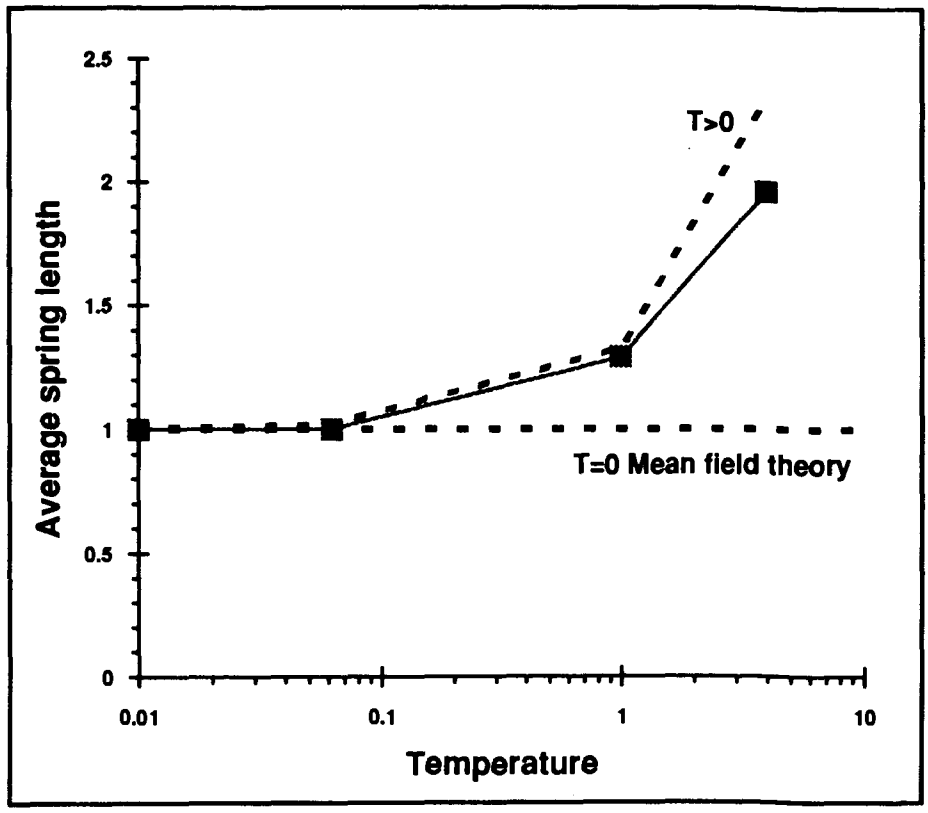

Figure 4.5 Average spring length $\langle s \rangle / s_h$ at zero pressure against temperature $k_B T/ks_h^2$ for self-avoiding Hooke's law network. The MFT prediction at T=0 and the prediction including the first-order temperature correction are shown for comparison. N = 144 vertices.

The relevant elastic constants of the two-dimensional network are the compression (K) and shear (μ) moduli. These may be combined to give the Poisson ratio (σ). Figure 4.6 shows the compression modulus against pressure for all the temperatures simulated. The compression modulus is defined in Section 3.2.2, and has the interpretation that a large value of K means that the material is rigid and fluctuations in its size are small.

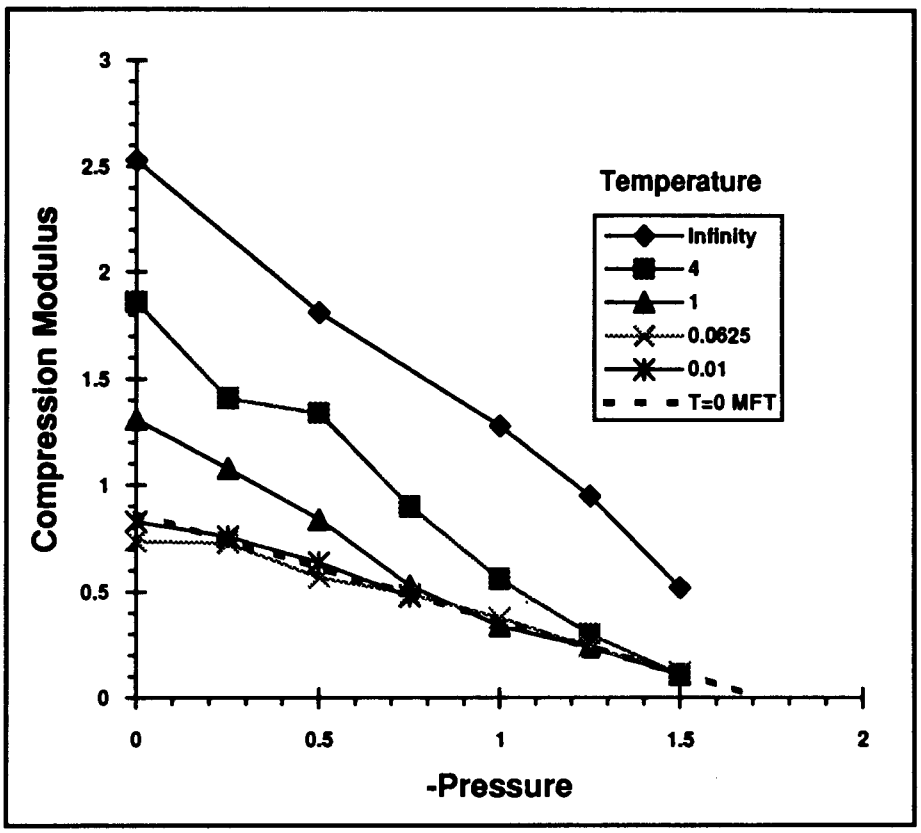

Figure 4.6 Compression modulus K/k against pressure p/k for self-avoiding Hooke's law network at all temperatures k_BT/ks_h^2 considered. N = 144 vertices. The T=0 MFT prediction from Eq. (3.31) is shown for comparison.

The trend in Fig. 4.6 is clear: as the pressure approaches the unstable point $p/k = -\sqrt{3}$, a small change in pressure produces a large change in network area and the compression modulus vanishes. As the pressure tends to zero the network becomes harder to compress until, at zero pressure, there is a temperature-dependent residual resistance to

compression. It is also clear from Fig. 4.6 that the zero temperature mean field expression for the compression modulus is only applicable for a network under a significant tension or at a low temperature, as expected.

For comparison we show the same results for the compression modulus against the area per vertex in Fig. 4.7 below. This shows that the data for different temperatures collapse onto one curve, the zero-temperature mean-field expression,

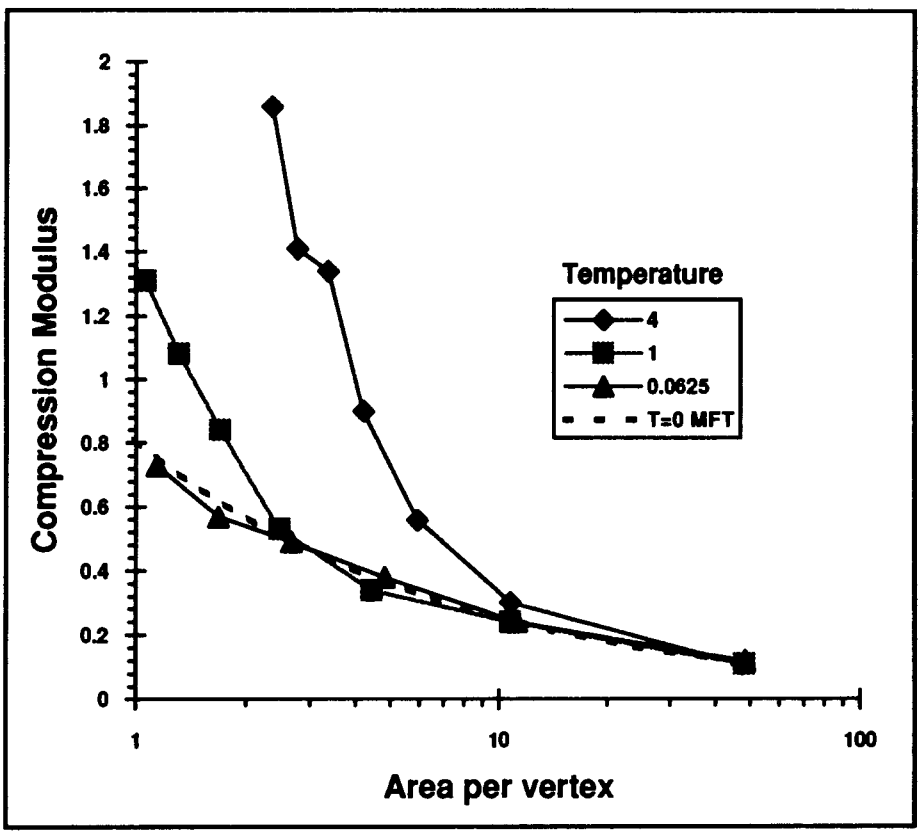

Figure 4.7 Compression modulus K/k against area per vertex $\langle A \rangle / N s_h^2$ for self-avoiding Hooke's law network at three temperatures $k_B T / k s_h^2$. N = 144 vertices. The T=0 MFT prediction using Eqs. (3.31) and (4.2) is shown for comparison.

when the network is stretched[4]. Notice that the infinite-temperature simulation cannot be normalised to plot against the area per vertex but is well-defined when plotted against pressure.

In Fig. 4.8 below we show the shear modulus against pressure for all temperatures.

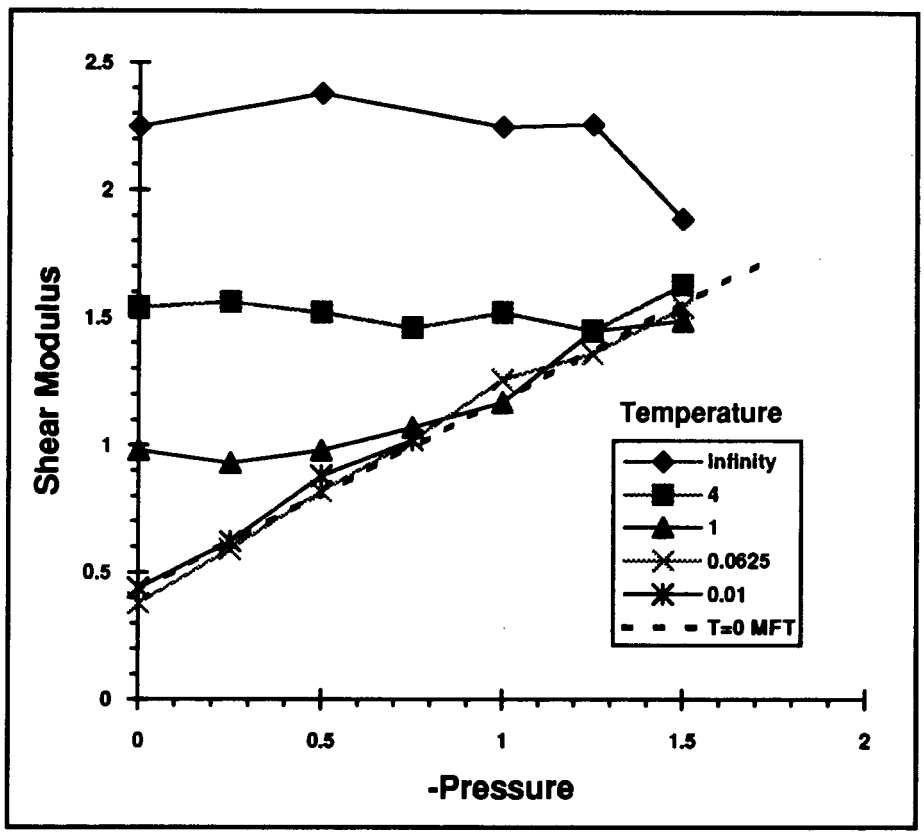

Figure 4.8 Shear modulus μ/k against pressure p/k for self-avoiding Hooke's law network at all temperatures k_BT/ks_h^2 considered. N = 144 vertices. The T=0 MFT prediction from Eq. (3.32) is shown for comparison.

[4]We omit the curve for a temperature of k_BT/ks_h^2 = 0.01 here and in Figure 4.9 for clarity, as it is indistinguishable from the T=0 MFT curve.

The shear modulus reflects the network's ability to resist two opposing, non-collinear forces in the plane, and a large value implies a strong resistance to shear. It can be seen that the shear modulus approaches the zero-temperature mean-field predictions from Eq. (3.32) ($\mu/k = \sqrt{3}/4$ at zero pressure, and $\mu/k = \sqrt{3}$ at a pressure of $p/k = -\sqrt{3}$) for temperatures $k_B T/ks_h^2 < 1$. We show the same results against the area per vertex in Fig. 4.9. This figure, and Fig. 4.7, show that as $p/k \to -\sqrt{3}$ the network behaviour agrees with the T=0 MFT prediction, in that the relative fluctuations of the spring lengths are small compared to the equilibrium length.

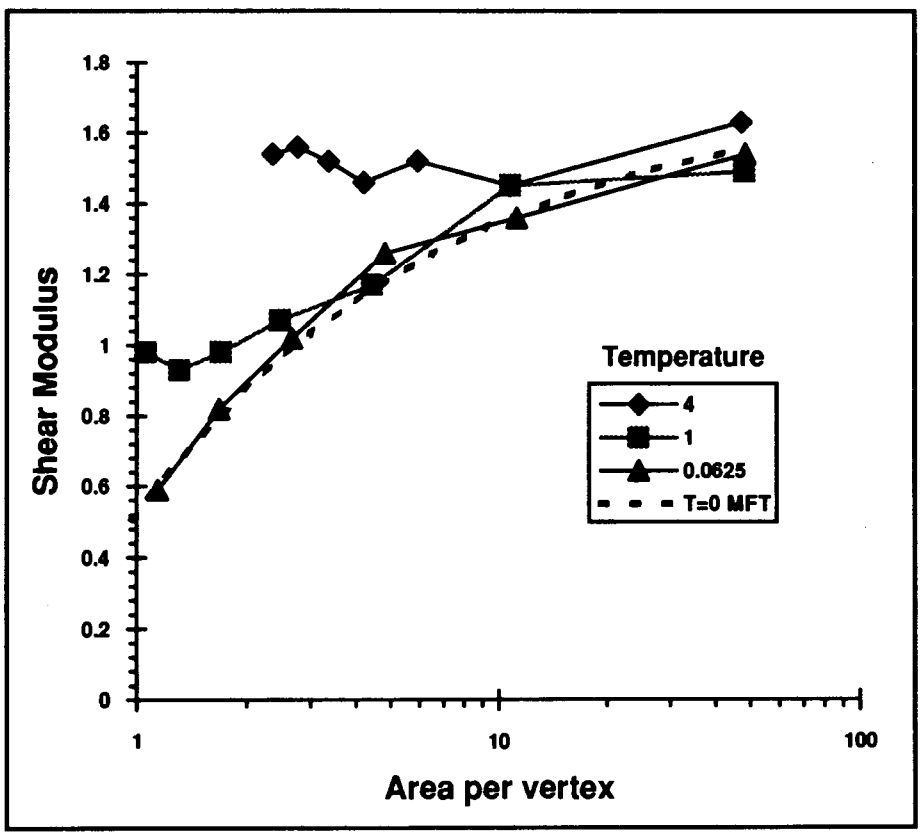

Figure 4.9 Shear modulus μ/k against area per vertex $\langle A \rangle / Ns_h^2$ for self-avoiding Hooke's law network at three temperatures $k_B T/ks_h^2$ considered. $N = 144$ vertices. The T=0 MFT prediction using Eqs. (3.32) and (4.2) is shown for comparison.

At low temperatures $k_BT/ks_h^2 < 1$, Figures 4.6 and 4.8 show that the ratio of the compression modulus to the shear modulus approaches the value of one half in the limit of zero pressure. This is predicted by the T=0 MFT in Eqs. (3.31) and (3.32) in Section 3.3.

The Poisson ratio σ is defined in Eq. (3.12) of Section 3.2.1, and it was mentioned in the introduction to Chapter 3 that almost all materials have a positive Poisson ratio. We plot the Poisson ratio for the SA network in Fig. 4.10. For pressures $p/k < -0.25$, the Poisson ratio is negative and becomes more negative with increasing pressure. It also appears from the figure that this result depends only weakly on temperature. There are fluctuations in the data but the trend is consistent for all temperatures. The results are in close agreement with the zero-temperature mean-field prediction of Eq. (3.33).

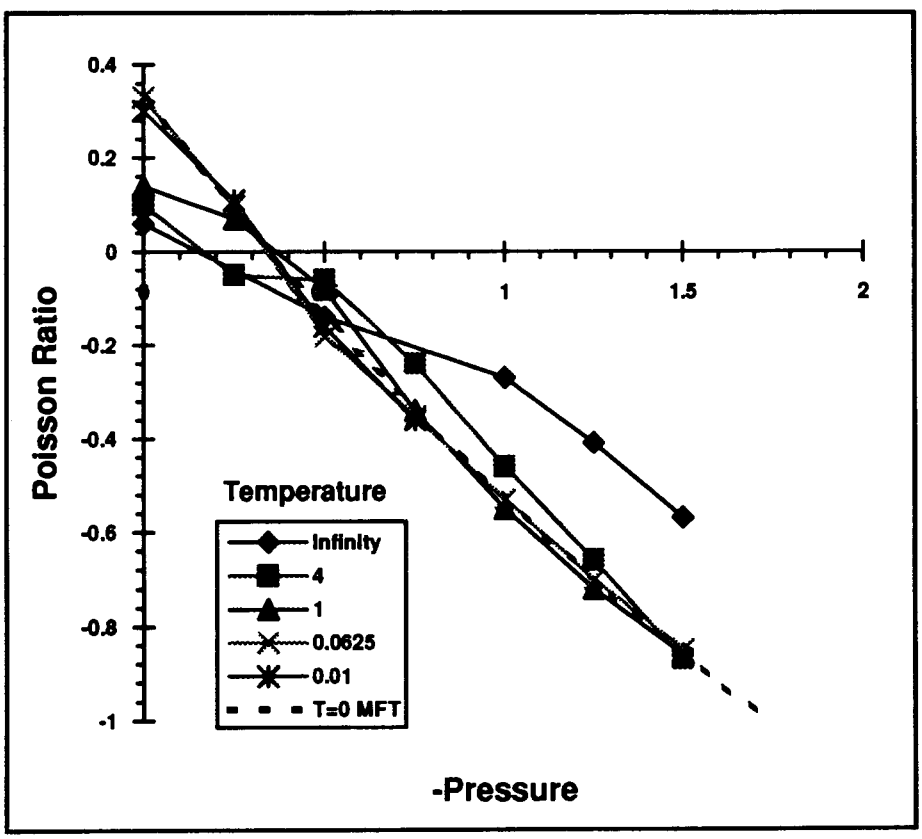

Figure 4.10 Poisson ratio σ against pressure p/k for self-avoiding Hooke's law network at all temperatures k_BT/ks_h^2 considered. N=144 vertices. The T=0 MFT prediction from Eq. (3.33) is shown for comparison.

4.3 Phantom Hooke's law networks

The self-avoiding network described in the previous section does not allow springs to cross one another. Removing this constraint produces a phantom network, whose springs can freely intersect. Here we describe the behaviour of the phantom network and compare it with that of the self-avoiding network. It may be recalled that phantom networks exhibit a collapsed phase in which the linear dimension grows with the logarithm of the system size. We do not investigate this regime here, because the simulations converge very poorly for the system sizes achievable.

It may be useful to mention here one-dimensional analogues of two-dimensional self-avoiding and phantom networks confined to a plane. The analogue of a self-avoiding network is the self-avoiding chain; and the analogue of a phantom network is the phantom chain, or random walk. The random walk as a model of a polymer has been extensively investigated and many results are known (see de Gennes, 1979 for a comprehensive discussion). Of relevance here is the comparison of the average size of the self-avoiding and random walks. The self-avoiding walk in one dimension consists of N equal length steps without overlap. Hence its average size is equal to its maximum size, Na, where a is the size of each step. By contrast, the average displacement of a one-dimensional random walk is given by $N^{\nu}a$, with $\nu = 1/2$. Removing the constraint of self-avoidance thus causes the walk to shrink. We anticipate that the self-avoiding and phantom networks in two dimensions will have different properties, as have self-avoiding and random chains in one dimension.

The first difference between the phantom and self-avoiding networks is seen in the normalised area per vertex shown in Figure 4.11. The phantom networks are seen to collapse to a small area at values of the pressure that depend on the temperature. Note that, although the phantom network at a temperature of $k_BT/ks_h^2 = 0.0625$ appears to

remain expanded even at zero pressure, it actually collapses to a value $\langle A \rangle / N s_h^2 < 0.05$ at a pressure very close to zero. In the highly stretched regime, as $p/k \to -\sqrt{3}$, the SA and phantom networks coincide, because the external pressure prevents the springs in the

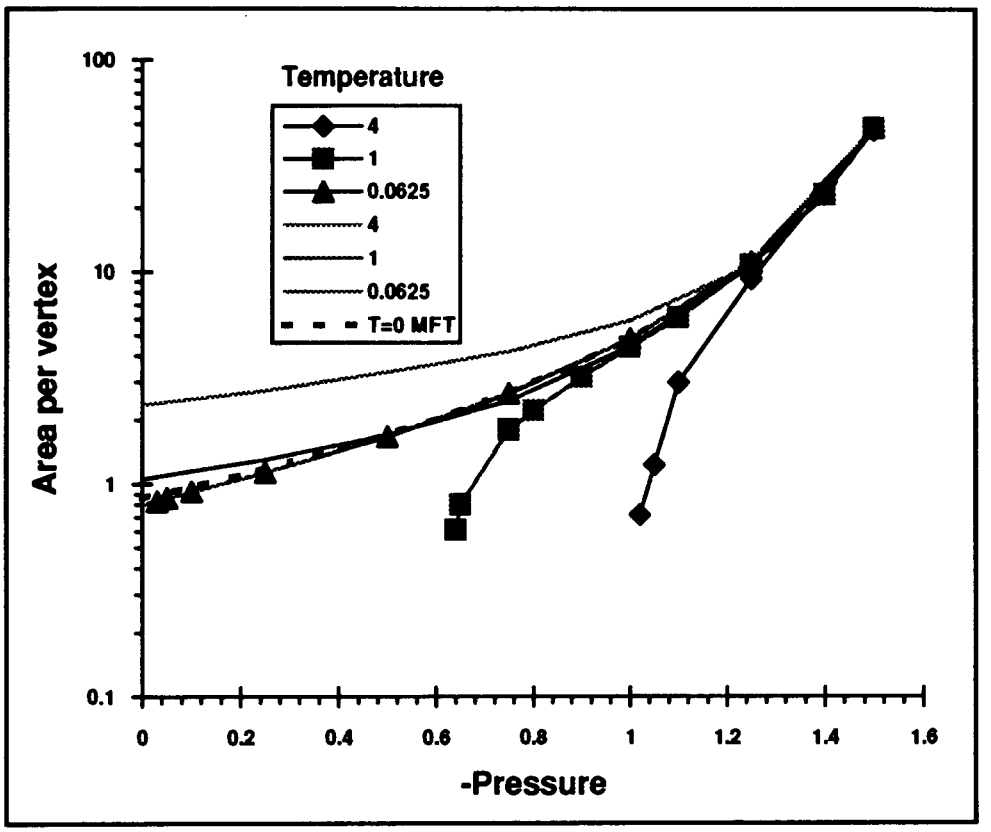

Figure 4.11 Area per vertex $\langle A \rangle / N s_h^2$ against pressure p/k for self-avoiding (without markers) and phantom (with markers) Hooke's law networks at three temperatures $k_B T / k s_h^2$. N = 256, 400 vertices for the phantom network. The T=0 MFT prediction from Eq. (4.2) is shown for comparison.

phantom network from overlapping. Hence, when the pressure $p/k < -1.2$, the SA and phantom networks both agree with the T=0 MFT prediction, to within the accuracy of the simulations.

The average spring length as a function of pressure is shown[5] in Fig. 4.12, and the relative standard deviation of the spring length is shown in Fig. 4.13. The average spring length in the phantom network agrees with the T=0 MFT prediction when the network is stretched at pressures $p/k < -1.2$. Unlike the area per vertex, the average spring length does not show a significant decrease even close to the collapse transition.

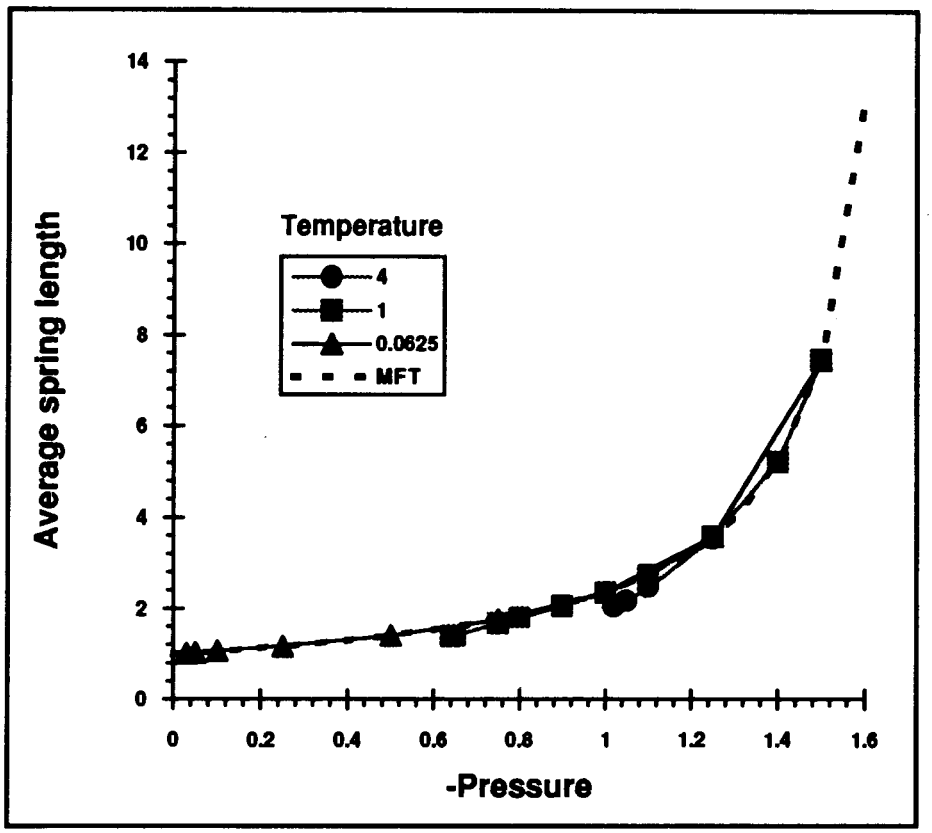

Figure 4.12 Average spring length $\langle s \rangle / s_h$ against pressure p/k for a phantom Hooke's law network at three temperatures $k_B T / k s_h^2$. $N = 256, 400$ vertices. The T=0 MFT prediction from Eq. (3.28) is shown for comparison.

For example, at a temperature of $k_B T / k s_h^2 = 4$, the pressure $p/k = -1.02$ is within 2% of the collapse pressure, but the average spring length is still $\langle s/s_h \rangle = 2.040 \pm 0.002$,

[5]We omit the SA results in Fig. 4.12 for clarity. They are indistinguishable from the T=0 MFT curve for temperatures $k_B T / k s_h^2 < 1$.

and the dispersion of spring lengths within a configuration is $\sigma(s) = 0.03 s_h$. This may be compared with a stretched configuration at a pressure of $p/k = -1.25$, for which the average spring length is $\langle s/s_h \rangle = 3.540 \pm 0.004$ and the spread within a configuration is $\sigma(s) = 0.04 s_h$.

Figure 4.13 shows that the relative dispersion in the spring lengths approaches zero as $p/k \to -\sqrt{3}$, as found for the SA network in Fig. 4.4, but increases as the collapse pressure is approached, in contrast to the SA network where the dispersion tends to a temperature-dependent constant as the pressure approaches zero. This suggests that the relative range of spring lengths in the phantom network increases as the network collapses.

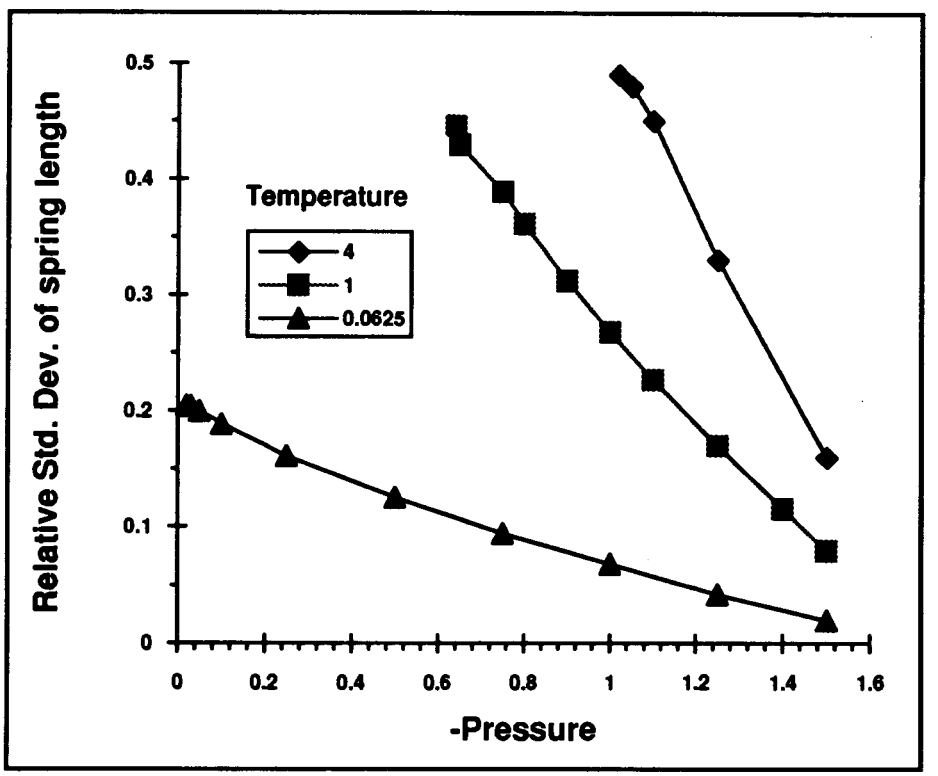

Figure 4.13 Relative standard deviation of spring length $\langle \sigma(\bar{s}) \rangle / \langle s \rangle$ against pressure p/k for phantom Hooke's law network at three temperatures $k_B T / k s_h^2$. $N = 256$, 400 vertices.

We plot the average spring length normalised by the square-root of the area per vertex in Fig. 4.14. This ratio is constant within the T=0 MFT, as may be seen from Eqs. (3.28) and (4.2), and has the value $\left(\sqrt{3}/2\right)^{-\frac{1}{2}} \approx 1.07$. This value implies that the simulation

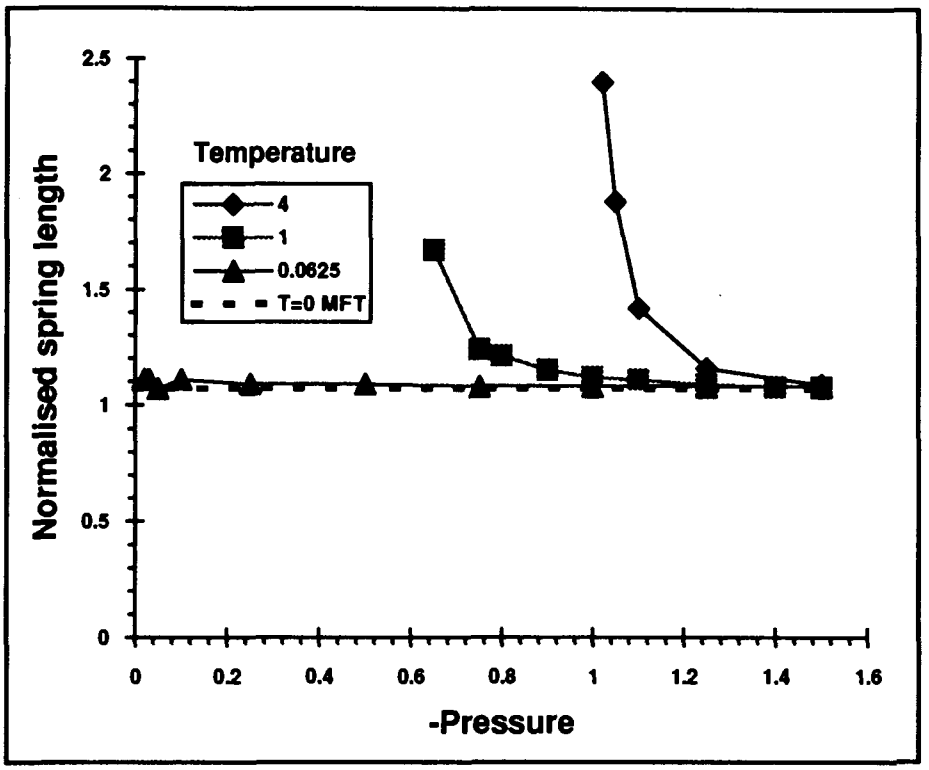

Figure 4.14 Normalised spring length $\langle s \rangle / \sqrt{\langle A \rangle / N}$ against pressure p/k, at three temperatures $k_B T / k s_h^2$, for phantom Hooke's law network showing the abrupt decrease in the network area at the collapse transition. N=256, 400 vertices. The T=0 MFT value from Eqs. (3.28) and (4.1) is shown for reference.

box is much larger than the average spring length in the network. When the average spring length approaches the dimensions of the system, the periodic boundary conditions become unreliable, as a vertex may interfere with its own periodic reflections. We have used 400 and 900 vertices for simulations close to the transition to try to keep the system dimensions larger than the average bond length. However, the reduction in the area per vertex is too great to allow us to simulate a collapsed network accurately.

The elastic constants for the phantom network show very different behaviour from that found in the SA network. The compression modulus is shown in Fig. 4.15 together with that of the self-avoiding network and the zero temperature mean field prediction. Both types of network agree with each other and the T=0 MFT, when they are highly

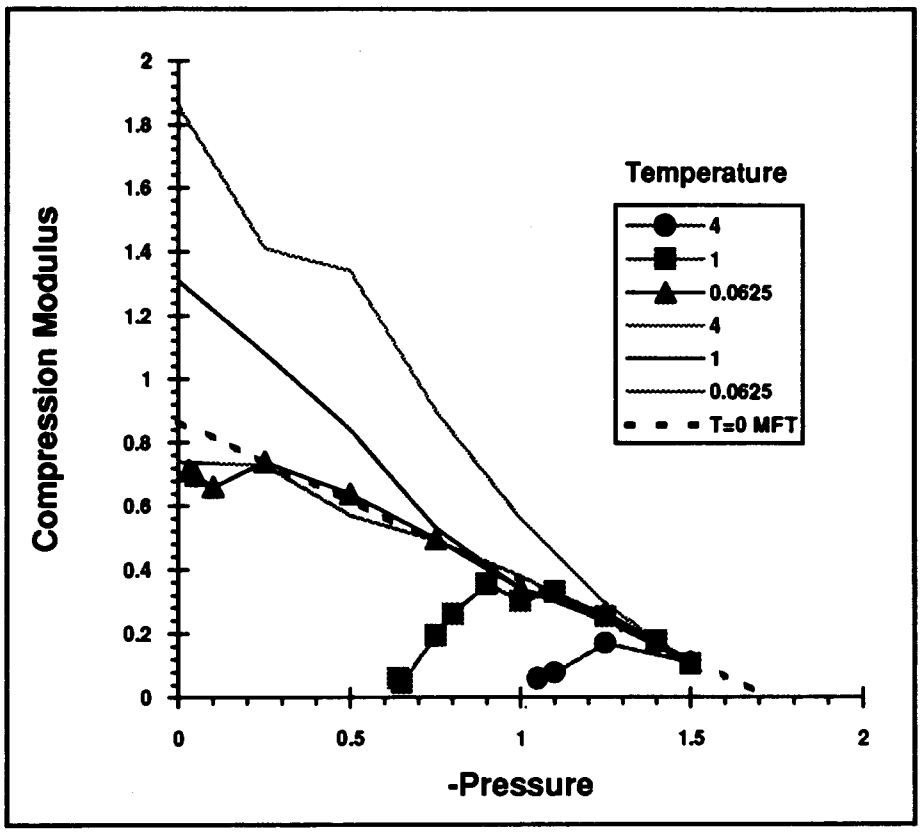

Figure 4.15 Compression modulus K/k against pressure p/k for phantom and self-avoiding networks at three temperatures k_BT/ks_h^2. The markers show the phantom network data. $N = 256, 400$ vertices. The T=0 MFT prediction from Eq. (3.31) is shown for comparison.

stretched and the pressure $p/k \to -\sqrt{3}$. As the pressure is reduced to zero the compression modulus for the phantom network reaches a maximum value and then drops to zero at a pressure that depends on the temperature.

There are thus two limits in which the phantom membrane has a small resistance to compression: when $p/k \to -\sqrt{3}$ the network is highly elastic and responds strongly to an infinitesimal change in pressure, and as the pressure is reduced to zero the springs in the network overlap allowing large fluctuations in area for small pressure changes.

Figure 4.16 compares the shear modulus for the SA and phantom networks with the T=0 MFT prediction. As for the compression modulus, the shear moduli for both types of network agree as the pressure $p/k \to -\sqrt{3}$. The shear modulus for the phantom network drops rapidly to zero at the same temperature-dependent pressure as the compression modulus and area per vertex.

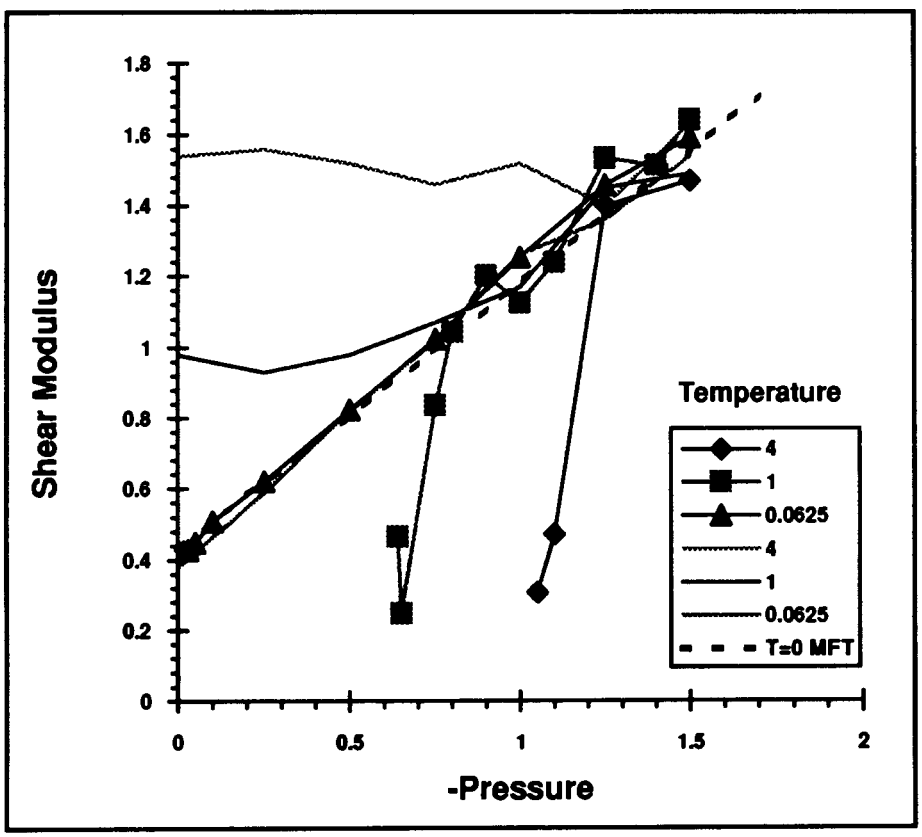

Figure 4.16 Shear modulus μ/k against pressure p/k for phantom and self-avoiding networks at three temperatures $k_B T/ks_h^2$. The markers show the phantom network data. $N = 256$, 400 vertices. The T=0 MFT prediction from Eq. (3.32) is shown for comparison.

The Poisson ratios for the SA and phantom networks are compared in Figure 4.17. Both networks have a negative Poisson ratio for all pressures $p/k < -0.4$. Unlike the results for the SA network where all the curves collapsed onto the T=0 MFT result, the Poisson ratio for the phantom networks falls away from the T=0 MFT curve at the same values of the pressure as found for the elastic constants and area. Note that for clarity we only show the SA curve at a single temperature as the curves at other temperatures are similar.

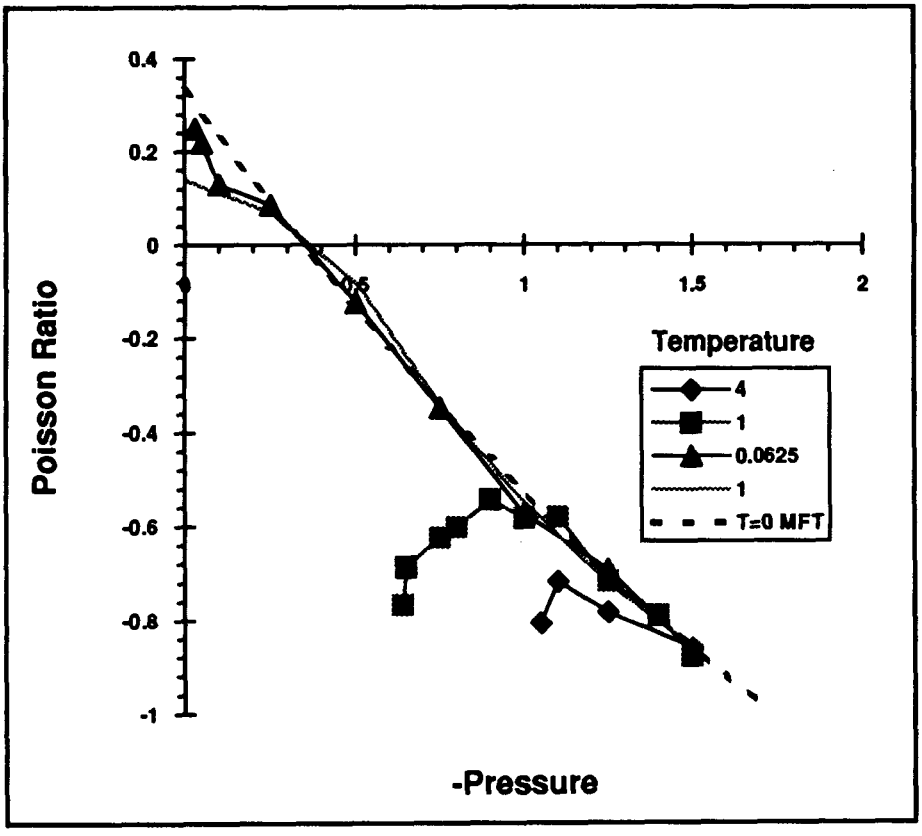

Figure 4.17 Comparison of Poisson ratio σ against pressure p/k for phantom and self-avoiding Hooke's law networks with T=0 MFT. The line without markers is for a self-avoiding network at a temperature $k_B T/ks_h^2 = 1$. $N = 256$, 400 vertices. The T=0 MFT curve from Eq. (3.33) is shown for comparison.

At the lowest temperature $k_BT/ks_h^2 = 0.0625$, the Poisson ratio appears to tend to the T=0 MFT limit of 1/3 at zero pressure as predicted by Eq.(3.33). However, we expect that at zero pressure the data will again diverge from the T=0 MFT curve as mentioned at the beginning of this section (see page 76).

Finally, we show an order parameter for the collapse transition in Figure 4.18. The order parameter is obtained from the normal vector to a triangle defined by three adjacent vertices in the network. This vector is positive by construction for the initial configuration

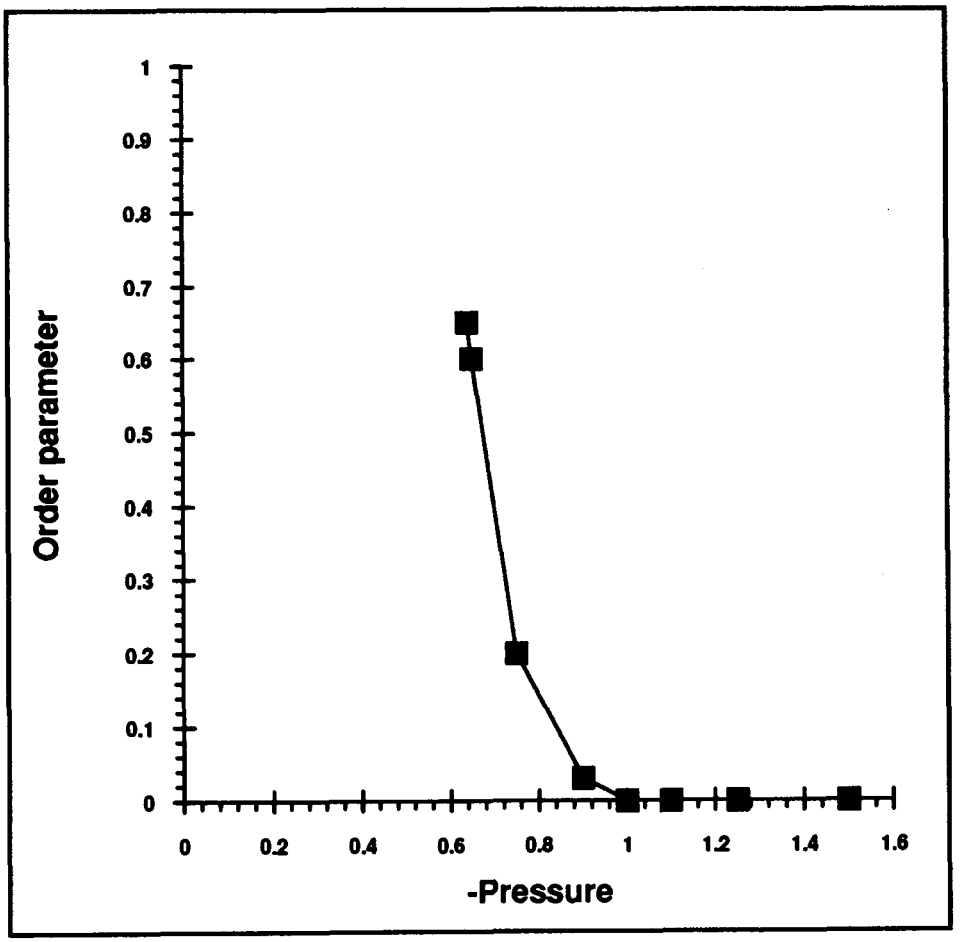

Figure 4.18 Order parameter (twice the fraction of inverted triangles) against pressure p/k for phantom network at a temperature $k_BT/ks_h^2 = 1$. $N = 256, 400$ vertices.

of springs in the regular, hexagonal network. If two of the springs along the side of a triangle subsequently cross, the sign of the normal vector is changed. We call such a triangle an inverted triangle. The order parameter is twice the fraction of inverted triangles.

4.4 Discussion

The zero temperature mean field theory of Chapter 3 accurately predicts the behaviour of both self-avoiding and phantom Hooke's law networks in the limits of low temperature, $k_BT/ks_h^2 < 1$, and high extension, $p/k \to -\sqrt{3}$. In these regimes, both types of network are composed of equivalent springs whose length is given by Eq. (3.28). The fluctuations in the spring lengths, relative to the equilibrium length, tend to zero as the network becomes highly stretched or the temperature tends to zero.

At constant temperature, $k_BT/ks_h^2 < 1$, the area per vertex of the self-avoiding network differs slightly from the T=0 MFT prediction as the pressure tends to zero. When the first finite temperature correction term to the area per vertex is included, the difference is reduced below 5%. At higher temperatures, $k_BT/ks_h^2 > 1$, the area per vertex diverges from the T=0 MFT result as the pressure decreases. This divergence is not accurately represented by including only the first correction term to the T=0 MFT result. Including further terms is not warranted, because the assumption on which the T=0 mean field theory is based breaks down at high temperatures. The zero temperature assumption is that all the springs in the network are at the same equilibrium length. This assumption becomes less applicable for the self-avoiding network at temperatures $k_BT/ks_h^2 > 1$. At these temperatures the dispersion of the spring lengths approaches one half of the equilibrium length as the pressure tends to zero, which shows there are many different spring lengths in the network.

The area per vertex for the phantom network is close to zero[6] below a temperature-dependent pressure. We refer to this effect as the collapse transition. Simultaneously, the dispersion in the spring length divided by the equilibrium length increases as the network approaches the collapse transition. This behaviour cannot be described within mean field theory. The springs in the phantom network become much less regular than is found in the self-avoiding case, although they maintain an average spring length not very different from the T=0 MFT prediction. This is borne out in the snapshot of the phantom network near the collapse transition shown in Figure 4.19.

At the critical pressure $p/k = -\sqrt{3}$ both the self-avoiding and phantom networks appear to expand without limit as predicted by T=0 MFT. The unstable expansion of the network at a finite pressure follows from consideration of the energy density of the springs. The work done in stretching the springs in the network is the product of the pressure and the area. Both the spring potential energy and the work scale linearly with the area of the network. A fluctuation that causes an increase in the area of the net, ΔA, produces a negative contribution[7] to the enthalpy due to the external pressure, $p\Delta A$. This is opposed by the increase in the spring energy $\frac{1}{2}k(s-s_h)^2$ but, depending on the relative magnitudes of the pressure and the spring constant, the net change in the enthalpy may be negative. In this case the fluctuation will grow, causing the network to undergo an unstable increase in area.

---

[6]At zero pressure the area per vetex $\langle A \rangle / Ns_h^2 < 0.05$.

[7]Recall that a stretching pressure has $p/k < 0$.

The elastic moduli of the self-avoiding network agree with the T=0 MFT predictions for temperatures $k_BT/ks_h^2 < 1$, and in the limit $p/k \to -\sqrt{3}$. Both the compression and shear moduli diverge from the T=0 MFT predictions at temperatures $k_BT/ks_h^2 > 1$. This deviation is larger than predicted by the first term in the finite temperature mean field theory. The Poisson ratio agrees with the T=0 MFT prediction surprisingly well.

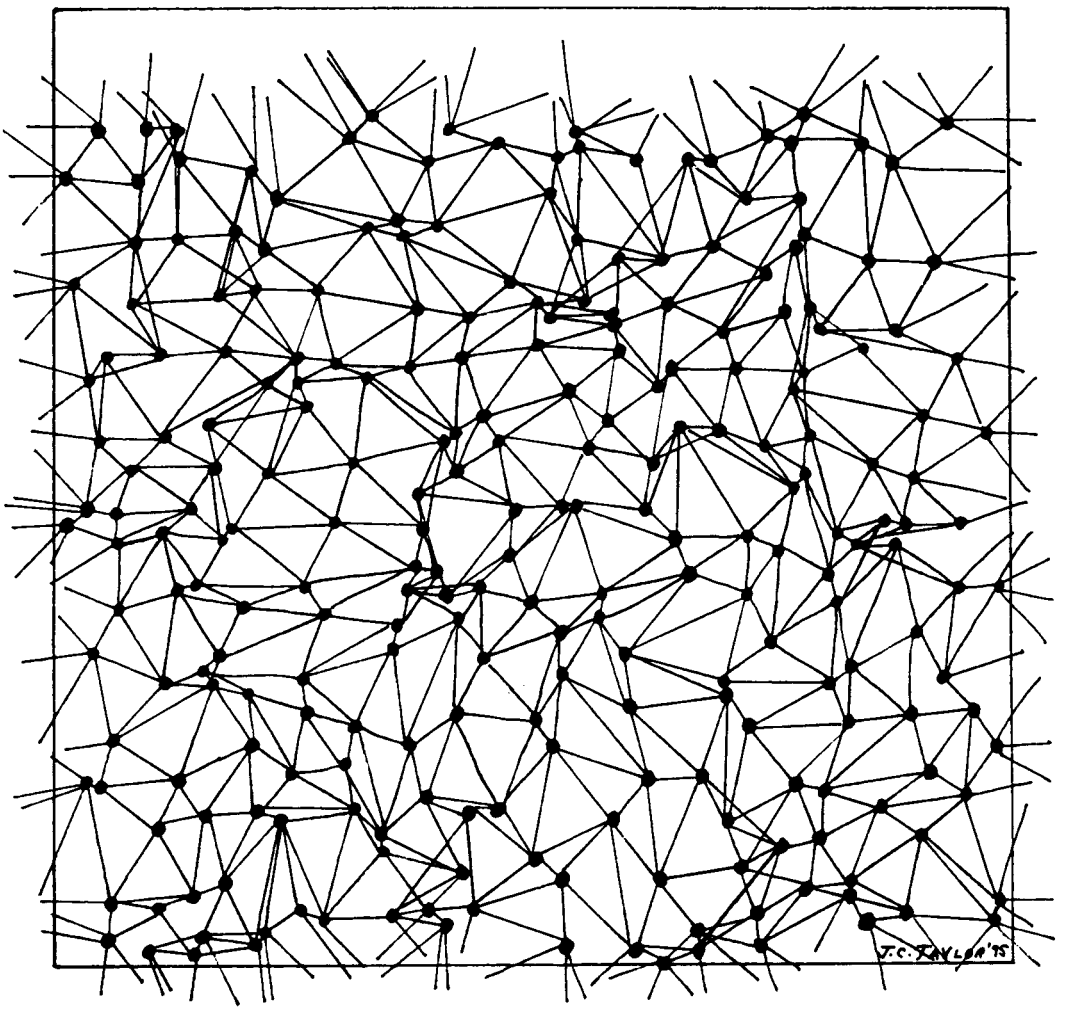

Figure 4.19 Phantom Hooke's law network near the collapse transition. The pressure is $p/k = -0.8$, and the temperature is $k_BT/ks_h^2 = 1$. The network shown has $N = 256$ vertices.

The elastic moduli of the phantom network behave quite differently from those of the self-avoiding network near the collapse transition. As the pressure is increased from $p/k = -\sqrt{3}$, the compression modulus follows the T=0 MFT at first and then falls to zero at a finite, temperature-dependent pressure. The shear modulus, compression modulus and area collapse occur at the same pressure and temperature. There are thus two regimes where the compression modulus of the phantom network vanishes. At the critical pressure $p/k = -\sqrt{3}$ an infinitesimal change in pressure produces an infinite[8] change in area and the network ceases to resist a hydrostatic pressure. Reducing the tension from the critical value allows the network to reduce its area by decreasing the length of its constituent springs. As the collapse transition is approached however, the phantom network area is further reduced as springs overlap. Because the spring lengths are not significantly different from their equilibrium value, there is no energy cost to these configurations, although there is a considerable entropy gain. The Poisson ratios for the phantom and self-avoiding networks are negative, and coincide when the networks are highly stretched or at low temperatures $k_B T/ks_h^2 < 1$. The Poisson ratio for the phantom network exhibits a maximum, below zero, and then drops to a more negative value as the pressure is reduced towards zero, while that for the self-avoiding network increases and becomes positive at a pressure just below zero.

4.5 Summary

We have presented results for the elastic properties of a two-dimensional membrane modelled as an hexagonal network of vertices connected by Hooke's law springs. The effects of temperature and an applied stretching pressure on the network's behaviour have been examined. The difference between a network in which the springs are self-avoiding and one in which the springs can cross is also investigated.

[8]In the thermodynamic limit of an infinite network.

The self-avoiding and phantom Hooke's law networks show an instability as the applied pressure approaches $p/k = -\sqrt{3}$: both networks expand without limit. As the pressure approaches zero, the behaviour of the two types of network diverges. The self-avoiding network approaches a stable state with the springs subject to thermal fluctuations about a finite average length. The fluctuations are smaller at lower temperatures as expected from zero temperature mean field theory. By contrast the phantom network shows a transition to a collapsed state of very small network area at a non-zero value of the applied pressure. The transition pressure depends on the temperature, and the elastic constants of the network approach zero at this pressure. The collapse process involves springs in the network crossing to remove area from the network at low pressures. The springs that overlap are not compressed significantly from their average length in the non-overlapping regions of the network.

The compression and shear moduli for the self-avoiding network approach the ratio $K/\mu = 2$ predicted from zero temperature mean field theory as the pressure approaches zero, for temperatures $k_B T/ks_h^2 < 1$. This agreement is lost for networks at higher temperatures. A criterion derived in Chapter 3 predicts that networks at zero pressure should agree with zero temperature mean field theory for temperatures $k_B T/ks_h^2 << 3$, and this is borne out in the simulations. The first term in the finite temperature mean field theory accurately predicts the network behaviour for temperatures up to $k_B T/ks_h^2 = 1$.

Both self-avoiding and phantom Hooke's law networks have a negative Poisson ratio over a large range of applied pressure. The Poisson ratio for self-avoiding networks agrees with zero temperature mean field theory at all the temperatures simulated. The Poisson ratio for the phantom network agrees with the T=0 prediction when the network is highly stretched, but it exhibits a maximum and then drops to a more negative value as the pressure is reduced towards zero.

CHAPTER 5

FLUID MEMBRANE STABILITY AND RUPTURE

5.1 Introduction

Lipid molecules spontaneously aggregate to form micelles or bilayers when placed in an aqueous solution at sufficient concentration (Israelachvilli, 1992, Ch. 16). The type of aggregate formed, e.g., micelle, bilayer, bicontinuous phase, etc., is determined by the physical characteristics of the lipids, such as their headgroup size and the length of their hydrocarbon tails. The stability of an aggregate results from the hydrophobic effect of the lipids and depends on the concentration of lipids in the surrounding aqueous environment. The cohesive energy of the lipids in a bilayer, for example, is also altered by adding lipids of incompatible shape. It is known that chemically treating erythrocytes with tellurite compounds (among others) causes leakage (Deuticke et al., 1992), although this process involves transmembrane proteins and protein-lipid interactions.

The health of a cell depends on the integrity of its plasma membrane which maintains its controlled isolation from the extracellular space. The lipid bilayer provides a tight chemical insulator that separates the interior of the cell from the exterior (Bloom, Evans and Mouritsen, 1991). Nevertheless, controlled transport of ions across the bilayer is needed to maintain constant cellular volume under osmotic stress. The fluid bilayer cannot support a significant pressure difference (Tanford, 1979), so transmembrane proteins control osmotic gradients by pumping ions across the bilayer. Thermal and osmotic stresses also act to destabilise the bilayer. Several experimental means have been used to probe the stability of the lipid bilayer by subjecting it to a lateral tension. Such tension is opposed by the hydrophobic effect of the lipids, but may cause the cell to rupture, or lyse, if the stress is sufficiently great. Experiments have also been directed at the reverse

process of attempting to reseal ruptured cells by adding surfactants that congregate at holes in the bilayer (Lee at al., 1992; Lee et al., 1994). In this chapter we investigate the stability of a model fluid membrane against hole formation at finite temperature and the effects of an applied tension.

Experimentally, cell lysis may be induced by means of an electric field across the cell that compresses the membrane (Glaser et al., 1988; Zhelev and Needham, 1993; Wilhelm et al., 1993; Freeman et al., 1994) or by placing the cell in a hypoosmotic solution, causing it to swell (Ertel et al., 1993; Hallett et al., 1993; Mui et al., 1993). Both processes tend to pull apart the lipids in the plasma membrane, thereby reducing their cohesion. Electroporation experiments show that the increase of the membrane area prior to rupture is small, only 2-3 percent of the total area, and the tension needed is of the order of 2-15 dyn/cm (Evans and Needham, 1987; Needham and Hochmuth, 1989).

It is not clear from experiments whether rupture occurs via a single large hole or many small holes. Vacancy condensation in ideal monolayers may result in the formation of a single large hole (Joós et al., 1994). Electroporation experiments suggest that irreversible membrane rupture proceeds via the unstable growth of a single hole (Wilhelm et al., 1993), while reversible leakage of intracellular solutes follows the appearance of many small holes. In addition, Hallett et al. (1993) and Mui et al. (1993) find that lysis of vesicles under hypoosmotic stress is not always irreversible. Vesicles swell until they rupture and eject some of their lumenal contents, whereupon they reseal. If the residual osmotic gradient is still great enough they will lyse again and eject another fraction of their contents. Taupin et al. (1975) measured the time-dependent leakage of a marker molecule from egg lecithin vesicles as a function of osmotic stress. They found different functional dependences for the leakage rates at high and low stress that were well described by postulating the irreversible growth of unstable holes that rupture the vesicle at high stress and fluctuations in size of many small, stable holes at low stress.

Recent experiments on the diffusion of water across lipid bilayers (Jansen and Blume, 1995) have been interpreted by postulating that small, transient pores created by thermal fluctuations of the lipids are always present in the plasma membrane of a cell. Transient pores have been used previously (Taupin et al., 1975) to account for variation in leakage rates of marker molecules in rupture experiments. Glaser et al. (1988) proposed that reversible electrical breakdown of lipid membranes involves two types of pore: the first are hydrophobic, with the lipid hydrocarbon tails in contact with the aqueous surroundings, the second are hydrophilic, in which the lipids around the pore rearrange so as to expose only their headgroups to the surrounding solution. They suggest that hydrophobic pores are formed spontaneously by thermal fluctuations of the lipids, and, if a pore has sufficient energy to overcome an energy barrier it rearranges into a hydrophilic pore.

A lipid bilayer subject to a lateral tension is in a metastable state. A transmembrane voltage reduces the barrier against hydrophilic pore growth and so causes rupture. A detailed model for the appearance of lipid vacancies in a fluid bilayer, and their aggregation to produce membrane rupture, has been proposed by Kashchiev and Exerowa (1983). This model postulates that thermally generated lipid vacancies in the bilayer can condense to form holes, and predicts a first-order transition between an unbroken state of the membrane and a condensed vacancy phase in which the bilayer has ruptured.

A different approach to modelling the rupture of the lipid bilayer uses a mesoscopic approximation to the actual intermolecular forces. Such a model was introduced by Litster (1975) and developed by Abidor et al. (1979), Powell and Weaver (1986), Popescu and Rucareanu (1991), among others. It has been extensively used to interpret the results of electroporation experiments (Glaser et al., 1988; Wilhelm et al., 1993; Freeman et al., 1994). These models represent the altered interactions of lipids on a hole boundary via a phenomenological edge free energy. The competition between the tension stretching the

membrane, and tending to increase the area of a hole, and the edge free energy, acting to reduce the perimeter of a hole, results in a barrier to rupture that renders the membrane metastable at non-zero stretching tension.

A somewhat related model for the transition of a circular membrane fragment to a closed, spherical vesicle, based on energy minimisation arguments, was described by Fromherz (1983, 1986). The transition is driven by the competition between the edge energy acting to close the disk to a sphere, and a bending energy that opposes distortion of the disk. The model restricts the membrane fragment to have the shape of a spherical shell lying on the continuum between a flat, circular disk and a closed sphere. For a particular ratio of the edge energy to bending energy, the disk spontaneously closes up to a sphere in a first-order transition. The edge energy at the transition derived from this model, $\lambda = 4.2 \times 10^{-6}$ dyn, agrees with that from electric field induced permeabilisation experiments, $\lambda = 0.9 - 3.05 \times 10^{-6}$ dyn, (Zhelev and Needham, 1993). The transition is susceptible to edge-active agents that reduce the edge energy around the disk boundary and destabilise the vesicle with respect to the disk.

Boal and Rao (1992b) studied the transition from an open sheet of fluid membrane to a closed sphere under the influence of an edge energy, membrane rigidity and temperature. Calculations at zero temperature examined the energy minimising shapes of the membrane, and Monte Carlo simulations were used to explore the finite temperature transition from an open membrane sheet to a closed vesicle, as the edge energy and rigidity of the vesicle were altered. Fromherz' model is a special case of this more general approach. The simulations showed that the open/closed transition persisted at zero bending rigidity. This demonstrates that thermal fluctuations can act to open a hole in a closed model membrane, whereas Fromherz' model requires a bending energy to destabilise the spherical vesicle.

In this chapter we study the stability and lysis of a two-dimensional model fluid membrane. The creation of a hole is subject to an energy cost, or line tension, that represents the interaction energy of lipids on the hole boundary compared to those in the bulk of the membrane. We use MC simulation to predict the behaviour of a single hole as a function of the edge energy, temperature, and surface pressure on the membrane. Finite temperature fluctuations in the shape of the hole boundary are treated exactly in the simulations. We make predictions for the following quantities related to membrane stability:

- minimum edge energy required for membrane stability at zero pressure
- hole size distribution and scaling behaviour
- effect of a crushing pressure, and the metastability of a membrane at a finite, stretching pressure.

Section 5.2 discusses the generic zero-temperature model for the rupture of a membrane under stress and introduces our description of membrane stability at finite temperature. Section 5.3 presents the results of the membrane stability simulations. Section 5.4 is a discussion of the results and their relation to other theories and simulations, and Section 5.5 summarises this chapter.

5.2 Theory of hole formation in 2D fluid membranes

5.2.1 Tension-driven membrane rupture at zero temperature

Common experimental techniques used to study cell rupture create a tension in the bilayer by applying an external electric field or osmotically inflating the cell. The tension stretches the bilayer laterally, forcing its component lipids apart and weakening their hydrophobic repulsion from water. It is believed (Freeman et al., 1994) that this is followed by rapid rearrangement of lipids in the membrane to form one or more aqueous holes, in which the lipids pack around the hole boundary with their headgroups facing into

the hole. The increase of the membrane area prior to rupture is small, only 2-3 percent of the total area (Needham and Hochmuth, 1989), and the tension needed is of the order of 2-15 dyn/cm (Evans and Needham, 1987).

We can understand the appearance of a hole in a membrane under lateral tension from the following zero-temperature argument. Consider a flat, uniform, circular membrane in 2D subject to a mechanical tension Γ (energy per unit area) that stretches the membrane. A circular hole of radius R is allowed to appear in the membrane subject to an edge energy λ (energy per unit length). The energy of the membrane with a hole, in excess of that of the unbroken state, is

$$E = 2\pi R\lambda - \pi R^2\Gamma, \tag{5.1}$$

where we assume that the membrane is incompressible, so that its only response to the tension is to change the size of the hole. The energy of the membrane increases monotonically with hole perimeter when the tension Γ is zero as shown in Fig. 5.1. At (small) non-zero tension the appearance of a hole renders the membrane metastable. The energy has a maximum at a hole radius

$$R^* = \frac{\lambda}{\Gamma}. \tag{5.2}$$

Holes smaller than the critical size R^* are long-lived, while holes larger than R^* grow without bound. The ruptured state is the thermodynamic equilibrium state of the membrane under tension; but, the barrier to the ruptured state may be very large and is found from Eq. (5.1)

$$\Delta E = E(R^*) = \frac{\pi\lambda^2}{\Gamma}. \tag{5.3}$$

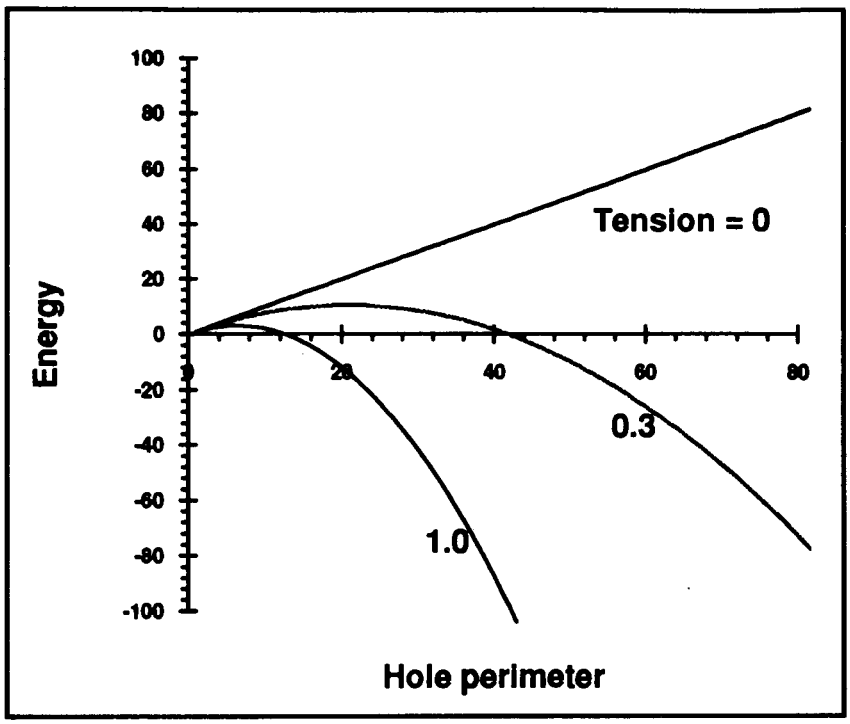

Figure 5.1 Energy $E/\lambda a$ of a flat membrane with a circular hole as a function of the hole perimeter (measured in units of a microscopic length a) for three values of the tension $\Gamma a/\lambda = 0, 0.3, 1.0$, as determined from the zero temperature expression Eq. (5.1).

The barrier height in Eq. (5.3) may be estimated using values for λ and Γ obtained from micromechanical and electroporation experiments. The tension at rupture Γ is proportional to the square of the transmembrane voltage in electroporation experiments (Glaser et al., 1988). Typical values for several vesicle/cell types are $\Gamma = 2-3$ dyn/cm for DMPC, 3-6 for SOPC, and 10 dyn/cm for an RBC (Evans and Needham, 1987; Needham and Hochmuth, 1989). These values increase with the addition of cholesterol to the membrane showing that the cholesterol-lipid interactions strengthen the membrane. The line tension λ has also been measured using electroporation techniques and has a value around $\lambda = 0.9 \times 10^{-6}$ dyn for SOPC (Zhelev and Needham, 1993). An estimate of the line tension necessary to close a circular membrane disk to a sphere has been made by Fromherz (1983), who obtained a value $\lambda = 4.2 \times 10^{-6}$ dyn. Most workers have assumed

that the line tension does not depend on the hole size and membrane curvature. Taking $\Gamma = 3$ dyn/cm and $\lambda = 10^{-6}$ dyn as representative values, the barrier height to rupture is 10^{-12} erg, or about 25 k_BT at room temperature. This value rises to 450 k_BT if Fromherz' value for the line tension is used. Such barriers are inaccessible to thermal fluctuations, at physiological temperatures, showing that the lipid bilayer is secure from rupture under normal conditions. This conclusion is supported by a theoretical model of membrane rupture that predicts a barrier height to spontaneous hole formation of 90 k_BT (Popescu and Rucareanu, 1991).

5.2.2 Entropy-driven membrane disintegration at finite temperature

The model of membrane rupture used in the experiments discussed so far assumes that the hole has an energy-minimising, circular shape. The inclusion of thermal fluctuations in the model will create a distribution of hole sizes in the membrane and allow the hole boundary to undergo shape fluctuations. These fluctuations will lower the free energy barrier against membrane rupture.

The lipid bilayer is usually viewed as a dense fluid of lipids held together by the hydrophobic effect of the hydrocarbon tails and opposed by the steric (and sometimes electrostatic) repulsion of the headgroups. Fluctuations in the membrane surface density occur at finite temperature. Weaver (1994) conjectures that vacancies occur when a lipid leaves the bilayer and goes into the surrounding bulk solution, while Helm et al. (1992) propose that adjacent lipids may spontaneously separate, briefly exposing their hydrocarbon tails to the surrounding solution. Dimples may also occur in the surface of the fluid bilayer (Popescu and Rucareanu, 1991). One model for rupture proposes that lipid vacancies can aggregate and form a hole that ruptures the membrane (Kashchiev and Exerowa, 1983).

The creation of a hydrophilic hole in the lipid bilayer involves rearrangement of the lipids to enable them to pack around the hole boundary. To avoid treating such complex motion, we try to model the behaviour of the hole boundary after rearrangement using a phenomenological line tension λ. In addition, because the radius of curvature of a cell is much larger than the hole diameter of interest, we restrict our model to two dimensions. The motive force for rupture is provided by a surface pressure p and thermal fluctuations. The free energy of an incompressible membrane with a hole of perimeter L, measured with respect to the unbroken state, may be written as the sum of the energy cost of creating the hole boundary λL, the work done by the external pressure p on the membrane of area A, and the entropy TS due the increased mobility of the "lipids" on the hole boundary.

The Gibbs free energy of the model membrane is

$$G = \lambda\langle L\rangle + p\langle A\rangle - T\langle S(L)\rangle, \tag{5.4}$$

where $S(L)$ is the entropy of the hole with perimeter L. Note that the pressure is conjugate to the total area of the membrane including the hole. We write the entropy of the hole boundary of length L as

$$S(L) = k_B \ln \Omega(n), \tag{5.5}$$

where k_B is Boltzmann's constant, and $\Omega(n)$ is the number of configurations of the boundary of a hole with perimeter $L = nb$, relative to the unbroken state of the membrane, and b is the average length of the individual elements around the hole. Boal and Rao (1992b) used an explicit counting of configurations for a simply connected sheet on a three-dimensional lattice to estimate the entropy change in hole formation via Eqs. (5.4) and (5.5) at zero pressure. They found a transition of the open membrane sheet in 3D to a closed vesicle as the line tension around the membrane boundary was increased. The open membrane was found to scale as a branched polymer, and its boundary contributed a

substantial configurational entropy to the sheet that had to be overcome in forming the closed vesicle. We expect the hole boundary in the 2D membrane to contribute a significant entropy to the free energy as well. As a trial calculation to see if an open/closed transition occurs at zero pressure in two dimensions, we estimate the behaviour of Eq. (5.5) using lattice results. While it is obviously not exact to treat the continuous boundary as having only a discrete number of conformations, it is not inconsistent with the spirit of the Monte Carlo simulations in the next section, in which the membrane is represented as a two-dimensional network of vertices connected by tethers, but the vertices are allowed to move continuously in the plane.

Lattice calculations of closed loops in two and three dimensions (McKenzie, 1976) and open sheets in three dimensions (Glaus, 1988) show that the number of configurations of length n behaves asymptotically as

$$\Omega(n) = \Omega_0 z^n n^{\alpha-2}, \qquad (5.6)$$

where z is related to the coordination number of the lattice, α is an exponent and Ω_0 is a prefactor that is independent of n. We postpone discussion of the precise scaling behaviour of the hole boundary, described by the exponent α, until Section 5.4. Given Eqs. (5.4)-(5.6), the Gibbs free energy, at zero pressure, of the membrane with a hole is

$$\beta G = (\beta\lambda b - \ln z)n - (\alpha - 2)\ln n - \ln \Omega_0, \qquad (5.7)$$

where β is the inverse temperature and b is a microscopic length. The last two terms are negligible relative to the first for large n, and the membrane has two distinct equilibrium states depending on the size of the line tension. These are

1 $\beta\lambda b > \ln z$ only small holes are present in the membrane,

2 $\beta\lambda b < \ln z$ holes in the membrane may grow without bound.

The transition separating these two cases occurs when the line tension is such as to make the first term in Eq. (5.7) vanish. As in the three-dimensional fluid sheets, this calculation predicts a sharp transition, in an infinite system, from a uniform state of the membrane with no hole at large line tension to a state with an infinite hole, when the line tension is below a critical value. However, the logarithmic term in the entropy cannot be neglected in a finite system. The $\log n$ term in Eq. (5.7) is a finite-size effect and is particularly important when the first term in the free energy is small, as it is in the transition region.

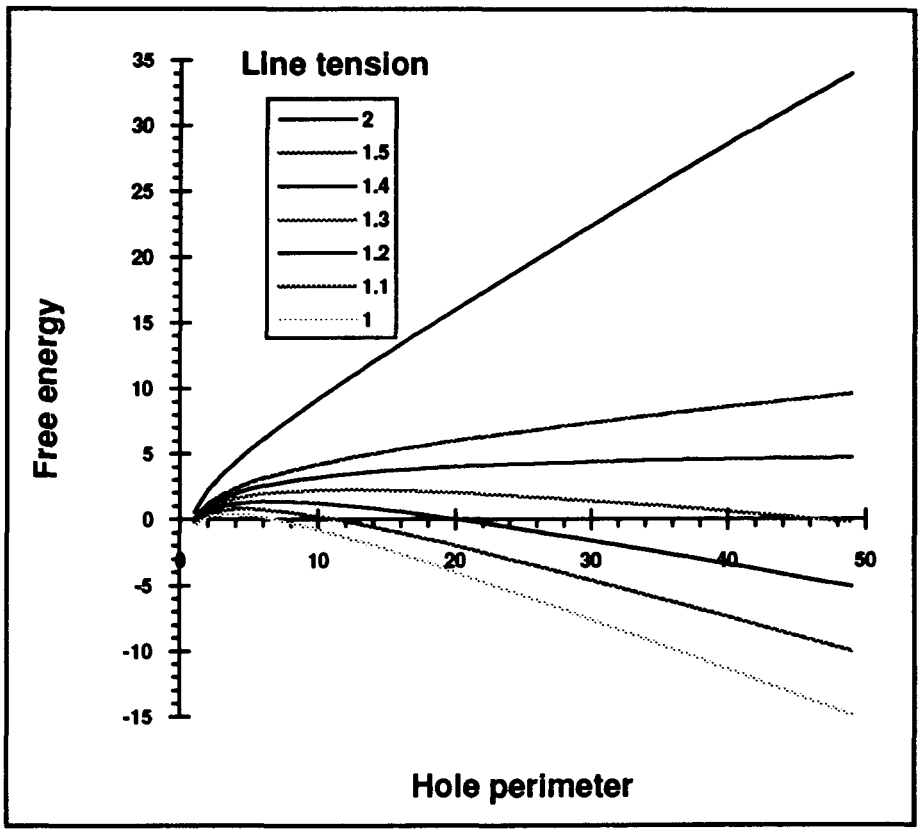

Figure 5.2 Dimensionless free energy $\beta G - \log \Omega_0$ of a model fluid membrane with a hole as a function of the hole perimeter L as determined from Eq. (5.7). The line tension appears in the dimensionless combination $\beta\lambda b$, and the hole perimeter is measured in units of b. The model assumes $p = 0, T \neq 0$, and the parameters $z = 4.15, \alpha = 0.5$ appropriate for a two-dimensional triangular lattice have been used (McKenzie, 1976).

The response of the membrane to the spontaneous appearance of a hole is illustrated in Fig. 5.2 where we plot the dimensionless free energy of the membrane as a function of hole perimeter for several values of the line tension at zero pressure. Note that we have subtracted the constant term, $\log\Omega_0$, from the free energy in the figure. If $\beta\lambda b$ is greater than a critical value, the smallest hole has the lowest free energy. If $\beta\lambda b$ is less than the critical value, then large holes are thermodynamically favoured, but small holes are metastable. The critical hole size at the transition is

$$n^* = \frac{(\alpha-2)}{(\beta\lambda b - \ln z)}, \tag{5.8}$$

and the barrier height at this hole size is

$$\beta G(n^*) = (\alpha-2)\left[1-\ln\left(\frac{\alpha-2}{\beta\lambda b-\ln z}\right)\right]. \tag{5.9}$$

This lattice-based model predicts that a membrane at finite temperature must have a minimum line tension to prevent spontaneous holes from growing and rupturing the membrane, even at zero pressure. We return to this model in Section 5.4 after presenting the results of our simulations.

5.3 Fluid membrane simulations

5.3.1 Introduction

In this section we investigate the growth of a hole in a model fluid membrane using Monte Carlo simulations. The membrane is represented by a triangulated network of vertices, with nearest-neighbour vertices connected by tethers with the potential energy function,

$$
\begin{aligned}
V(s_{ij}) &= \infty \qquad |s_{ij}| < a, \\
&= 0 \qquad a < |s_{ij}| < s_0, \\
&= \infty \qquad s_0 < |s_{ij}|,
\end{aligned}
\tag{5.10}
$$

where s_{ij} is the length of the tether joining vertices i and j, a is the hard-core diameter of a vertex, and s_0 is the maximum tether length. All vertices are subject to the hard-core repulsion embodied in the first line of Eq. (5.10). In order to prevent the tethers from crossing one another, to make the membrane self-avoiding, the maximum tether length must satisfy $s_0 < 2a$. We define λ as the energy cost per unit length to create the hole boundary. This energy represents the difference, in the actual fluid bilayer, of the interaction energy of the lipids on the hole boundary compared to those in the bulk membrane. We use a to set the length scale, so that the simulation contains as parameters the dimensionless combinations, $\beta\lambda a$ and $\beta p a^2$, where $\beta = 1/k_B T$ is the inverse temperature and p is the surface pressure.

Consider a rectangular patch of N vertices connected by $3N$ tethers cut from a triangulated network and confined to two dimensions. Confining the membrane to two dimensions restricts its application in biomembranes to length scales small compared to the persistence length of the surface. This latter quantity is typically more than a micron for biomembranes. Experiments have found that the holes present when a vesicle ruptures are typically tens of nanometres (Mui et al., 1993) to a micron (Zhelev and Needham, 1993) in diameter. Periodic boundary conditions are used to reduce the influence of the edges of the network. We use the isobaric-isothermal Metropolis MC algorithm to make small random changes in the relevant degrees of freedom, here the vertex positions and box side lengths, and to assign a Boltzmann weight to the resulting network configuration. This weight ensures that the configurations generated by the algorithm are distributed according to the equilibrium probabilities of the canonical ensemble. The vertex-move and box-rescaling algorithms are similar to those for the polymerised membrane simulations,

with the additional constraint that a vertex move or box rescaling is rejected if any tether violates the conditions of Eq. (5.10). The fluidity of the membrane is simulated by allowing the tethers to be cut and reconnected between adjacent vertices, again subject to Eq. (5.10). The algorithm for implementing bond fluidity was introduced by Baumgartner and Ho (1990), and its details are given in Appendix B.

A hole is introduced into the network by removing a single bond in the initial configuration, so that the membrane always contains at least four bonds defining the hole. Attempts are made to shrink or expand the hole using the Metropolis procedure. An adjacent pair of vertices on the hole perimeter is randomly chosen and an attempt is made either to remove the tether between them or to add a tether across one of the two vertices by linking its two neighbours on the perimeter. Notice that we restrict the maximum tether length to $s_0 = 1.688a < \sqrt{3}a$, to prevent interference by a distant vertex on the hole perimeter with a tether being connected across a vertex. This choice also facilitates comparison with three-dimensional membrane simulations which use $s_0 = \sqrt{3}a$ as the maximum tether length. This algorithm is similar to that used by Boal and Rao (1992b) for membranes embedded in three dimensions.

We define a *sweep* through the network as an attempt to move each vertex, rescale the box side lengths independently, cut and reconnect each tether that is not on the hole perimeter, and attempt to remove or add N tethers around the hole perimeter. Technical details of the procedures are given in Appendix B. The network is allowed to relax from the initial configuration (in which all vertices occupy the sites of a regular triangular lattice) before data collection begins. To reduce the correlations between successive configurations generated by the MC procedure, sample configurations are collected at intervals separated by a large number of sweeps, usually 50,000. We monitor the autocorrelations of the hole area, the eigenvalues of its inertia tensor and the simulation box area.

A snapshot of a typical network with a small hole is shown in Fig. 5.3. A snapshot of a similar network with a larger hole is shown in Fig. 5.4, and illustrates the non-local steric interaction that results from the self-avoidance of the tethers around the hole perimeter. Note that the network is not allowed to separate into disconnected pieces, so the hole perimeter must remain simply connected as depicted in Fig. 5.5, where the line tension is well below the critical value and the hole has expanded to occupy most of the membrane area.

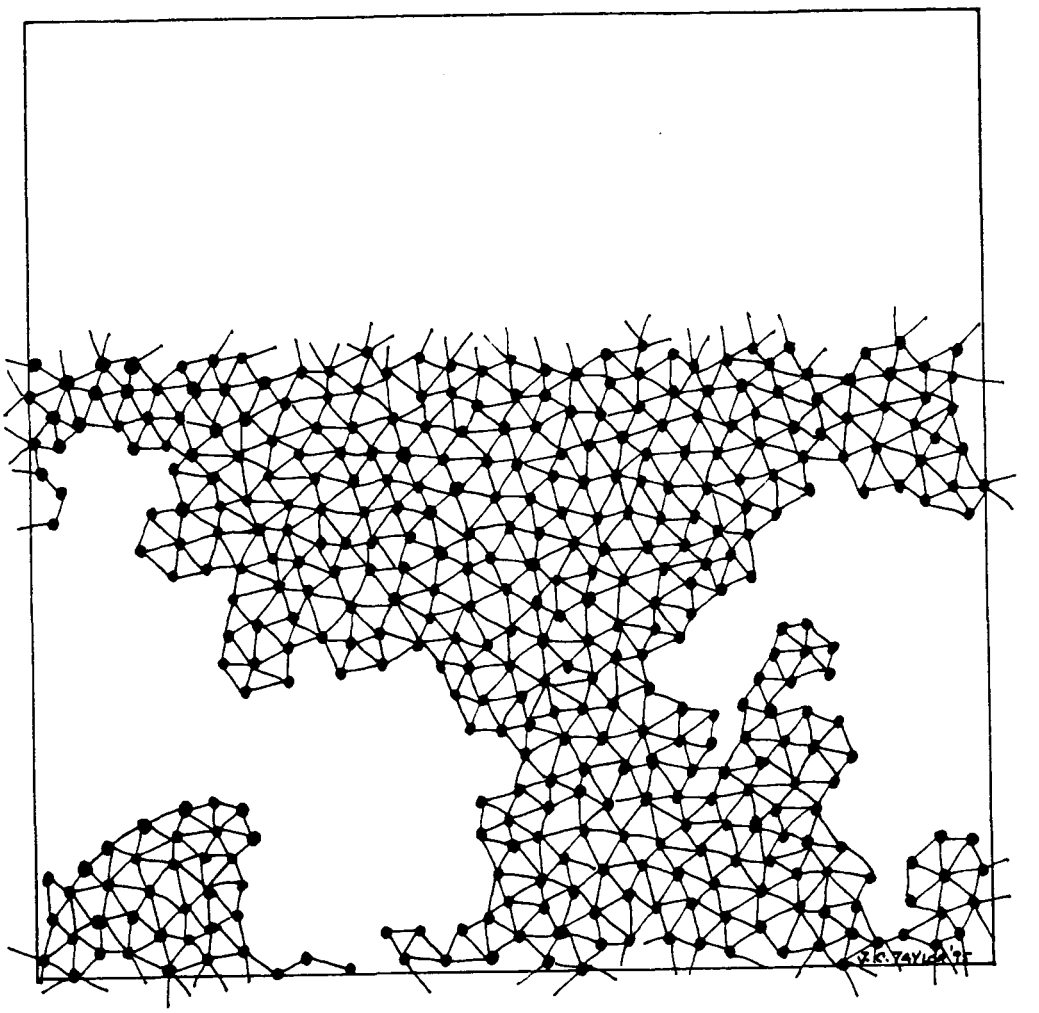

Figure 5.3 Snapshot of a fluid network with $N = 400$ vertices and a line tension $\beta\lambda a = 1.24$, showing a small hole.

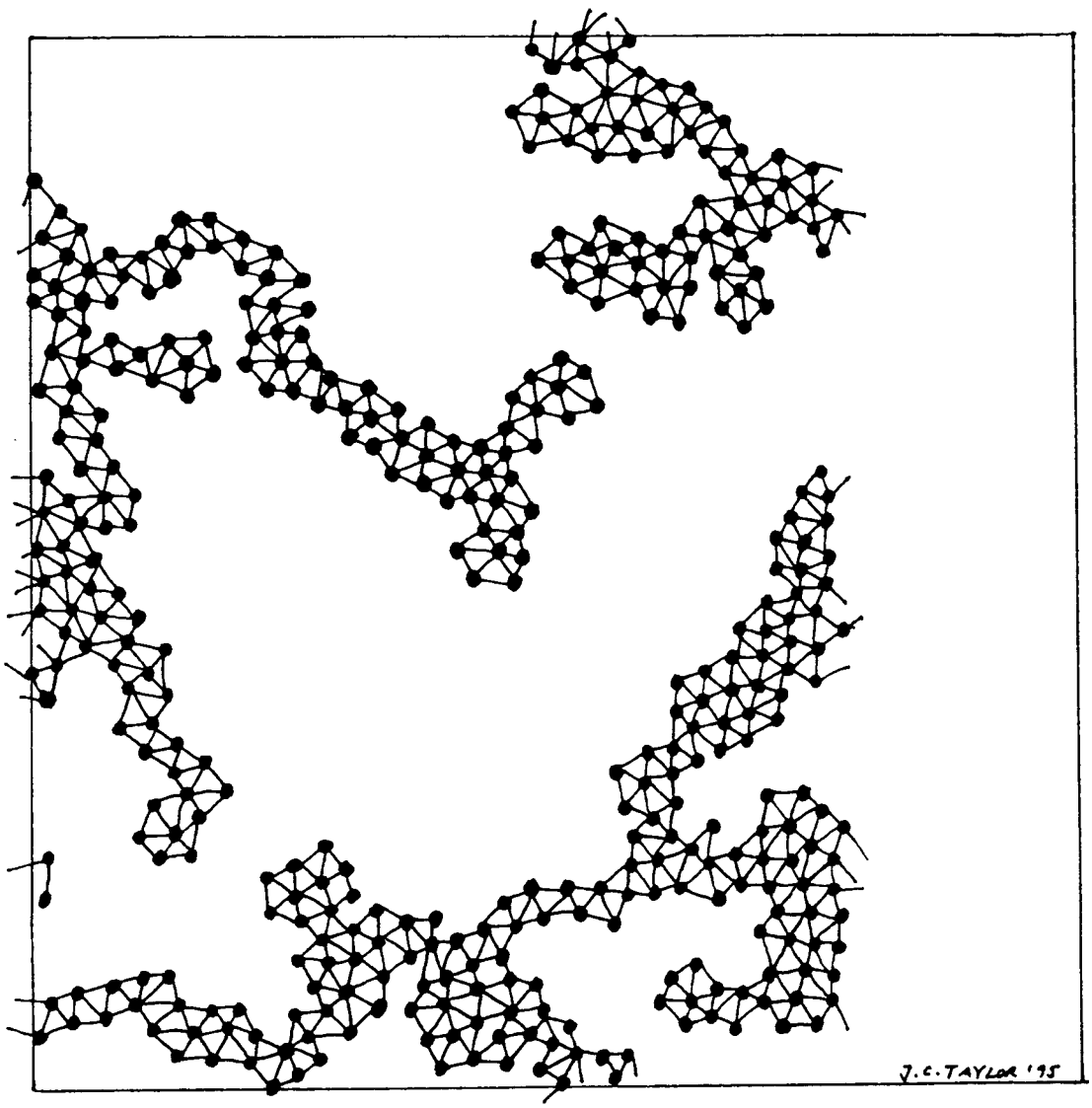

Figure 5.4 Snapshot of a fluid network with $N = 400$ vertices and a line tension $\beta\lambda a = 1.24$, showing the convoluted shape of the perimeter of a large hole.

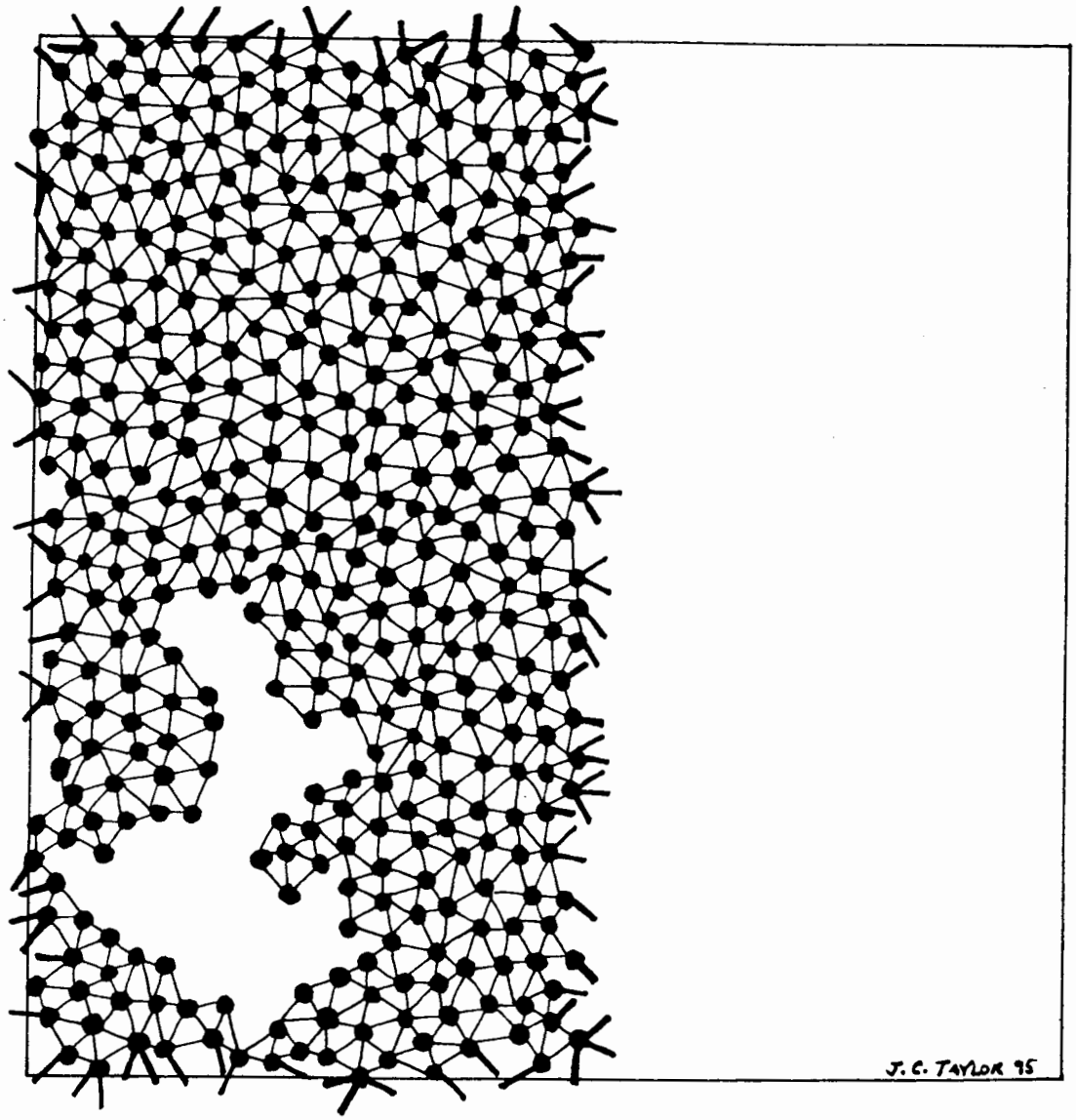

Figure 5.5 Snapshot of a fluid network with $N = 400$ vertices and a line tension $\beta\lambda a = 0.8$, showing the branched polymer character of the ruptured membrane.

5.3.2 *Membrane stability at zero pressure*

The theory of Section 5.2.1 only considers the possibility of a circular hole appearing in the model membrane at finite surface pressure and zero temperature. Non-circular hole configurations are expected at finite temperature as outlined in Section 5.2.2. The barrier separating the unbroken membrane[1] from the ruptured state at finite temperature and zero pressure, Eq. (5.9), has a very different form from the zero temperature barrier function, Eq. (5.2). We look first at the appearance of the membrane boundary (or hole perimeter) as a function of the line tension at zero pressure.

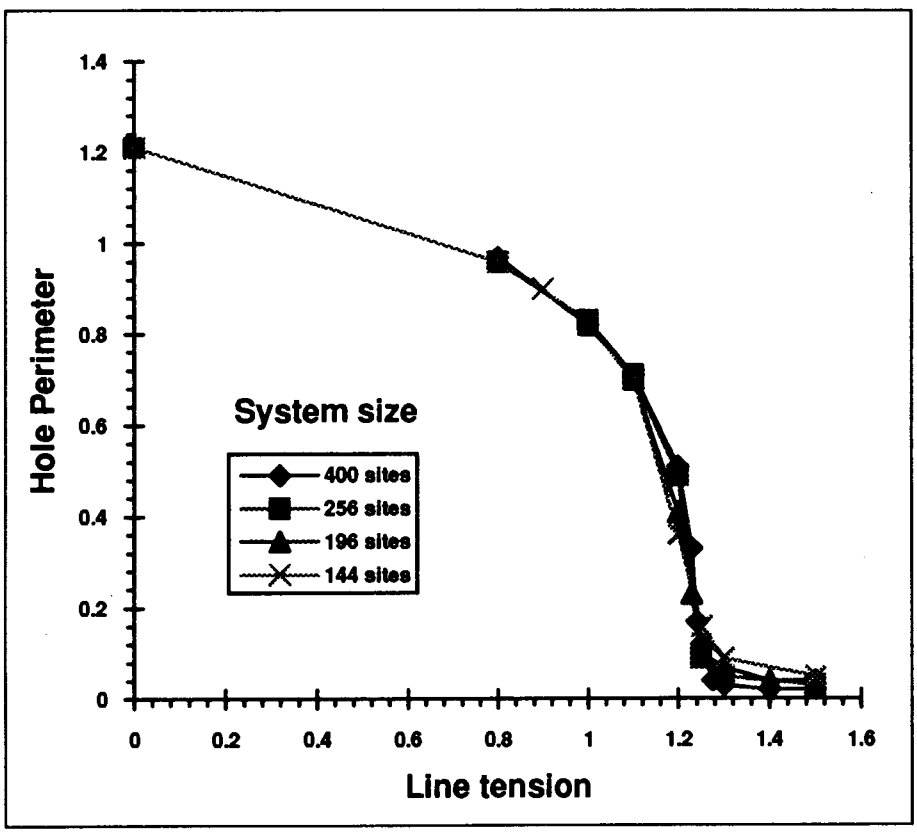

Figure 5.6 Hole perimeter scaled by the system size $\langle L \rangle / Na$ against the dimensionless line tension $\beta\lambda a$ for system sizes $N = 144, 196, 256, 400$ vertices.

[1]The minimum hole has four vertices on its perimeter because one tether is always missing from the network. We regard such holes as negligible because they owe their existence to the discrete nature of the model network and not to the energetics of hole creation.

The average length of the hole perimeter as a function of the line tension is shown in Fig. 5.6 for the four network sizes used, $N = 144,196,256,400$ vertices. The data collapse onto a single curve when scaled by the system size. The hole has a perimeter on the scale of the tether length for line tensions greater than a critical value $\beta\lambda a = 1.25 \pm 0.05$, and grows abruptly for line tensions lower than this value. The critical line tension is the same within statistical error for all the system sizes studied. For line tensions less than the critical value, the hole grows to occupy the whole network and is limited only by the requirement that the network remain simply connected. It is clear from Fig. 5.6 that the hole perimeter scales linearly with the membrane size, a characteristic to which we return in Section 5.4.

The standard deviation of the hole perimeter divided by the average perimeter is

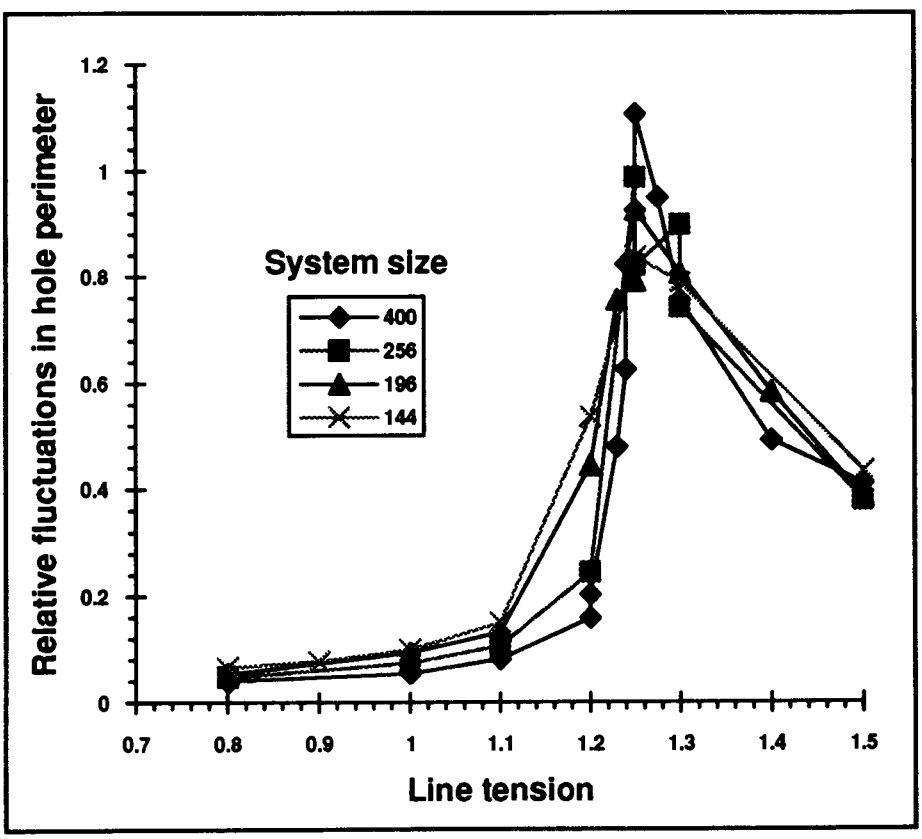

Figure 5.7 Standard deviation of the hole perimeter divided by the average perimeter $\langle\sigma(L)\rangle/\langle L\rangle$ as a function of the dimensionless line tension $\beta\lambda a$, for system sizes $N = 144,196,256,400$ vertices.

seen in Fig. 5.7 to peak at approximately the same critical line tension for the four system sizes. The magnitude of the relative fluctuations is not significantly different within the range of system sizes we have simulated. The slight increase seen for the systems with 256, 400 vertices compared to the systems with 144, 196 vertices is smaller than the spread of values obtained from different simulations. We are therefore unable to conclude that the change with system size is significant.

There are many ways to characterise the size and shape of an irregular object, such as the hole depicted in Fig. 5.4, none of which is both simple and complete. The area of the hole is an obvious measure of its size but gives no information about its shape. The radius of gyration offers a simple, one-parameter measure of the size of an object. The radius of gyration, R_g^2, of an object embedded in d-dimensional space is related to the eigenvalues of the inertia tensor T_{ij}, $(i, j = 1,...d)$

$$T_{ij} = \frac{1}{2N^2} \sum_{\alpha,\beta=1}^{N} \left(x_i^\alpha - x_i^\beta\right)\left(x_j^\alpha - x_j^\beta\right), \tag{5.11}$$

via

$$R_g^2 = \sum_{i=1}^{d} \lambda_i , \tag{5.12}$$

where λ_i are the eigenvalues. A simple measure of the shape asymmetry of an object in two dimensions is given by the ratio Δ of the larger to smaller eigenvalue of the inertia tensor,

$$\Delta = \lambda_1/\lambda_2 , \tag{5.13}$$

where $\lambda_1 > \lambda_2$. This ratio is unity for a circle and tends to infinity as the object becomes more elongated, i.e., one-dimensional.

Fractal objects share the property that their radius of gyration scales as a power of their mass (or number of monomers in a discrete object). Objects that scale with the same power law are said to be in the same universality class, and much effort has been spent trying to distinguish the criteria for membership of different universality classes. The radius of gyration has been extensively used to describe ring-polymers[2] embedded in two dimensions (Leibler, Singh, Fisher, 1987; Camacho, Fisher, Singh, 1991) as precursors to investigations of vesicles in three dimensions (Baumgartner and Ho, 1990; Gompper and Kroll, 1992; Boal and Rao, 1992a; Gompper and Kroll, 1995). The presence of a bending rigidity, or pressure difference between the inside and outside of the ring, results in the ring polymer having several distinct scaling regimes that are characterised by different exponents. The scaling properties of the radius of gyration, volume, and area of an object distinguish different universality classes, such as the closed self-avoiding random walk (CSAW) and branched polymer (BP). In 2D, the area and radius of gyration of a ring polymer (in the absence of bending rigidity and pressure) both scale with mass M to the same power, while the scaling exponents for a branched polymer differ. This is expressed as

$$\left\langle A\left(M_{per}\right)\right\rangle = A_0 M_{per}^{2\nu}, \tag{5.14}$$

$$\left\langle R_g^2\left(M_{per}\right)\right\rangle = R_{g0}^2 M_{per}^{2\nu}, \tag{5.15}$$

with one exponent ν for a random walk, and M_{per} being the mass of the ring or perimeter, and

$$\left\langle A\left(M_{enc}\right)\right\rangle = A_0 M_{enc}^{2\nu_A}, \tag{5.16}$$

$$\left\langle R_g^2\left(M_{enc}\right)\right\rangle = R_{g0}^2 M_{enc}^{2\nu_R}, \tag{5.17}$$

[2]A ring polymer is a closed, one-dimensional chain in which adjacent vertices are connected such that the ring does not intersect itself.

with two exponents for the branched polymer, and M_{enc} now being the mass or area enclosed by the branched polymer. The angle brackets represent ensemble averages. The prefactors in Eqs. (5.14)-(5.17) may have finite-size dependence.

The hole area and radius of gyration are calculated from the positions of the vertices on the hole boundary[3]. Figure 5.8 shows a negligible hole area for line tensions above $\beta\lambda a = 1.25$, and an abrupt increase for line tensions below this value. The area increase occurs at the same line tension as the hole perimeter increase in Fig. 5.5. The radius of

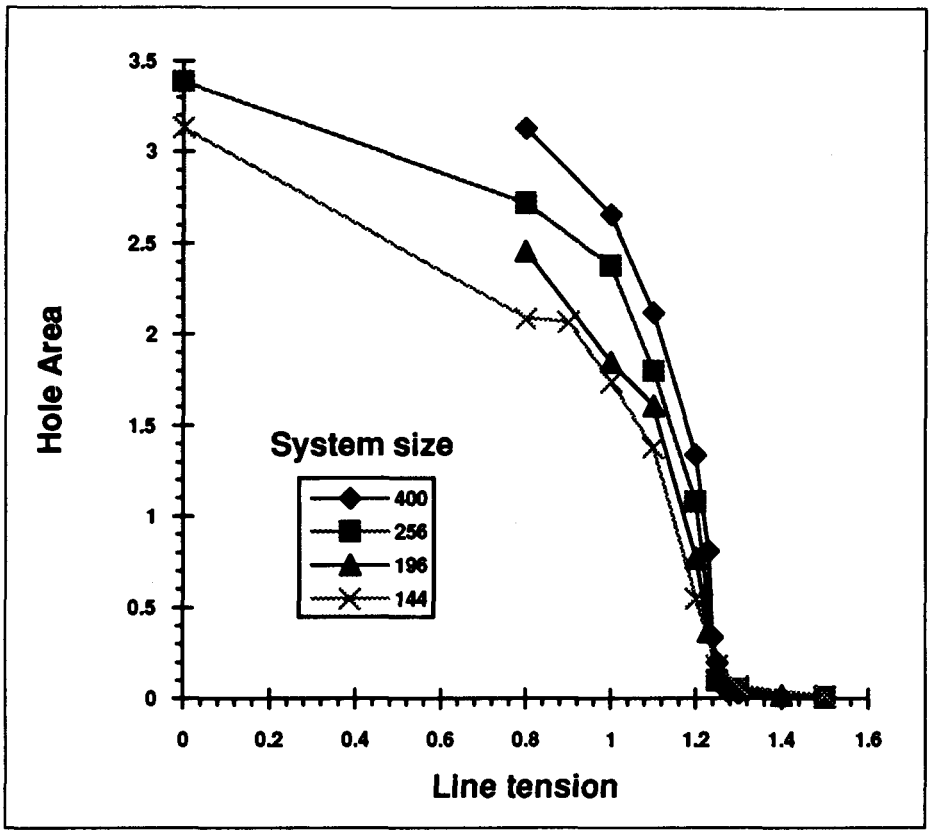

Figure 5.8 Hole area scaled by the system size $\langle A_{hole} \rangle / Na^2$ against the dimensionless line tension $\beta\lambda a$, for system sizes $N = 144, 196, 256, 400$ vertices.

[3]The accuracy of the calculation of R_g^2 is increased by dividing each external tether into 50 points and using these points to define the hole boundary.

gyration, shown in Fig. 5.9, has similar behaviour to that of the area. Both graphs show the data scaled by the system size, but it is clear that the hole area and radius of gyration do not scale linearly with the system size as did the hole perimeter. The correct scaling

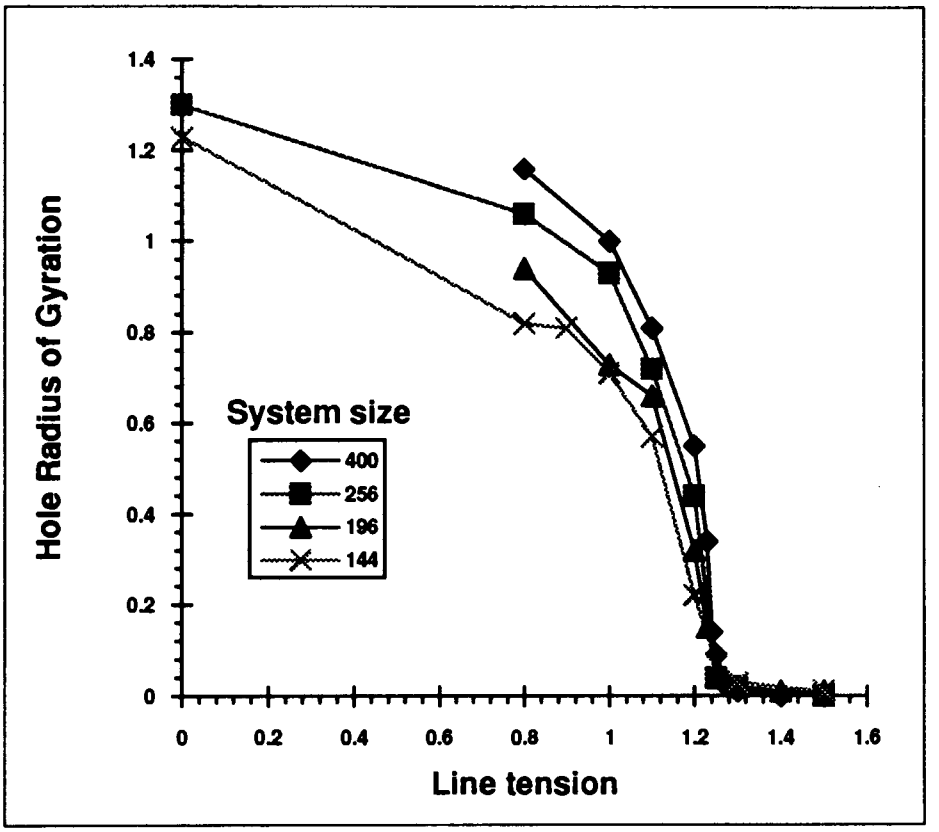

Figure 5.9 Hole radius of gyration scaled by the system size $\langle R_g^2 \rangle / Na^2$ against dimensionless line tension $\beta\lambda a$, for system sizes $N = 144, 196, 256, 400$ vertices.

form of these quantities is discussed later.

The scaling behaviour of the membrane area (excluding the hole) with the hole perimeter is shown in Fig. 5.10 for the four system sizes used, $N = 144, 196, 256, 400$ vertices. The membrane area is independent of the hole perimeter for line tensions above the critical value, because the hole is negligibly small, and it scales linearly with the hole perimeter for line tensions below the critical value, indicative of branched polymer

behaviour. The slopes of the curves for $\beta\lambda a = 0.8, 1.0$ are 0.97 ± 0.02 and 0.99 ± 0.01 respectively. Boal and Rao (1992b) investigated the transition between an open sheet and a closed sphere for fluid membranes in three dimensions as a function of the line tension around the boundary. They found that the open membrane has branched polymer scaling behaviour, and we see this behaviour in two dimensions.

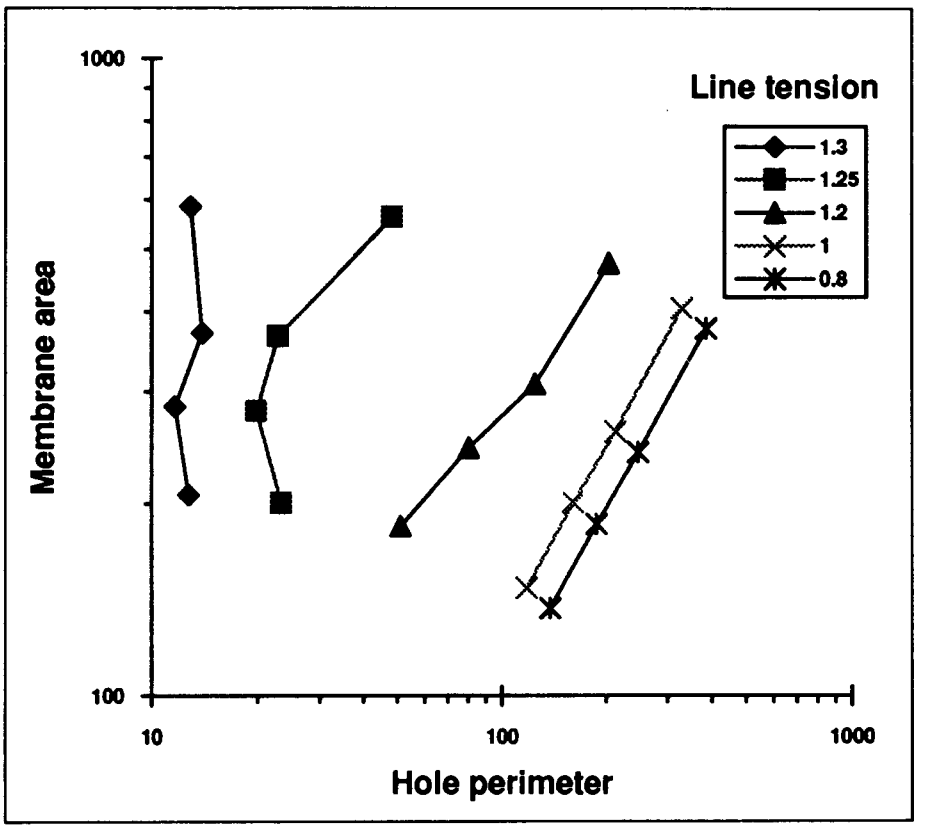

Figure 5.10 Membrane area $\langle A \rangle / a^2$ (excluding the hole area) against hole perimeter $\langle L \rangle / a$ for system sizes $N = 144, 196, 256, 400$, and several values of the dimensionless line tension $\beta\lambda a$. The slopes of the lines for $\beta\lambda a = 0.8, 1.0$ are unity.

We show how the hole area scales with its perimeter in Fig. 5.11. When the line tension is above the critical value, $\beta\lambda a > 1.25$, the hole is small and almost circular, and its area scales as the square of its perimeter. The slope of the curve for $\beta\lambda a = 1.3$ is

2.10 ± 0.12, while at $\beta\lambda a = 1.25$ and $\beta\lambda a = 1.2$ the slopes are 1.56 ± 0.06, and 1.38 ± 0.10. The exponent for a line tension $\beta\lambda a = 1.25$ suggests that the hole area scales as a CSAW at the transition: further results supporting this scaling behaviour are presented in Section 5.3.4. The slopes of the curves for $\beta\lambda a = 0.8, 1.0$ are 1.36 ± 0.04 and 1.35 ± 0.10 respectively, suggesting that the hole area does not scale as a BP below the transition. Comparing Figs. 5.10 and 5.11 shows that the hole and membrane areas have different scaling behaviour below the transition.

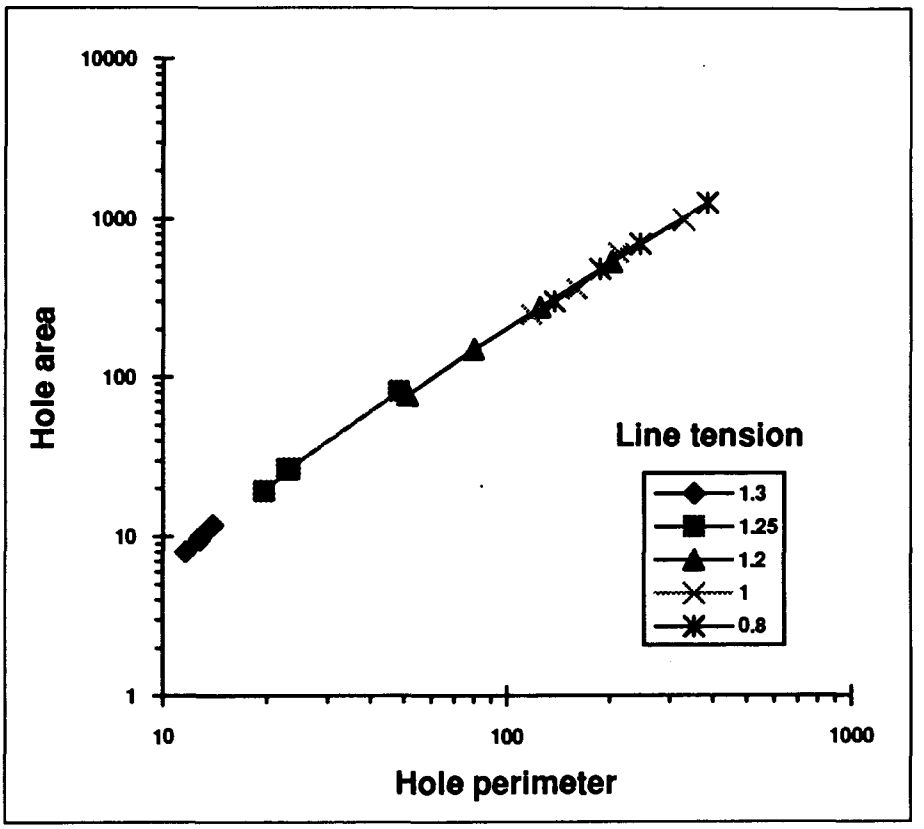

Figure 5.11 Hole area $\langle A_{hole} \rangle / a^2$ against hole perimeter $\langle L \rangle / a$ for system sizes $N = 144, 196, 256, 400$, and several values of the dimensionless line tension $\beta\lambda a$. The slopes of the curves are given in the text.

The model presented in Section 5.2.2 assumes that the presence of the hole has no effect on the remainder of the bulk membrane or network. We have verified this assumption by examining the area per triangle of the network as a function of the hole size. The area per triangle is the network area divided by the number of triangles N_Δ in its interior. The maximum tether length in the simulations is $s_0 = 1.688a$, leading to a mean tether length, averaged over 20 independent simulations of networks with 400 vertices, and line tensions ranging from $\beta\lambda a = 0.8$ to $\beta\lambda a = 1.5$, of $\langle s/a \rangle = 1.3320 \pm 0.0003$. This average was found to be independent of the line tension and system size to the accuracy of the simulations. The area per triangle is predicted to be $\langle A/N_\Delta a^2 \rangle = \sqrt{3}/4 \langle s/a \rangle^2 \approx 0.7683$. The area per triangle averaged over the 20 simulations is $\langle A/N_\Delta a^2 \rangle = 0.7366 \pm 0.0005$, which is within 4% of the predicted value. The area per triangle varies by less than 1% for all simulations regardless of the line tension and system size. The independence of the area per triangle from hole size supports the assumption made in Section 5.2.2 that the average properties of the bulk membrane are unaffected by the presence of the hole.

Visual examination of the network shows the occurrence of highly asymmetrical boundary shapes. The asymmetry arises because there are more ways of stretching the fluid network and reconnecting the tethers around a long, thin rectangular shape than one that is more nearly square. It was checked by inspection that the shape of the network was not correlated with hole size. Because the periodic boundary conditions constrain the network to be rectangular, the network asymmetry is measured by the ratio of the long to the short side averaged over all configurations. The average of eight simulations with $\beta\lambda a > 1.25$ (two at each system size) gives a network asymmetry of 2.75 ± 0.02, whereas the asymmetry averaged over eight simulations with $\beta\lambda a < 1.25$, is 1.57 ± 0.06.

The average of eight simulations with $\beta\lambda a > 1.25$ (two at each system size) gives a (small) hole asymmetry Δ of 3.01 ± 0.34. The asymmetry of the (larger) holes averaged

over eight simulations with $\beta\lambda a < 1.25$, is 3.40 ± 0.08. No dependence of the hole or network asymmetry on system size is found.

5.3.3 *Membrane elastic properties*

The shear modulus of a fluid network is identically zero. The small fluctuations of the shear modulus with different sample sets provide an estimate of the statistical accuracy of the simulations. The shear modulus, for simulations at zero pressure, was found to satisfy $\beta\mu a^2 < 0.01$ independent of the hole size, and was closer to zero than its statistical error.[4] This accuracy is achieved with 400 configurations for most cases, and with 1000 configurations used for approximately one third of the simulations. There was no significant change in the accuracy in the two cases.

The compression modulus for the network drops from a value $\beta K a^2 \approx 20$, as found previously in simulations of the network representation used here (Boal, Seifert and Zilker, 1992), for line tensions above the critical value, to a value close to zero when the hole is present. The presence of the hole removes the resistance to compression of the network, and even the small holes present for line tensions just above the critical value are sufficient to reduce the compression modulus. Figure 5.12 shows that the compression modulus is independent of the system size to the accuracy of the simulations; the compression modulus is known to 20% accuracy for line tensions greater than the critical value, and is consistent with zero, within statistical error, for line tensions below the transition. To estimate the standard errors of the elastic moduli we use the following method. The sample configurations from a simulation are divided into five groups and the elastic moduli are calculated for each group. The five independent values of the moduli are used to estimate the standard errors of the mean values for the complete set of configurations in the simulation.

[4]The Young's moduli and elastic constants of the fluid network are measured using the methods described in Chapter 3 for polymerised networks.

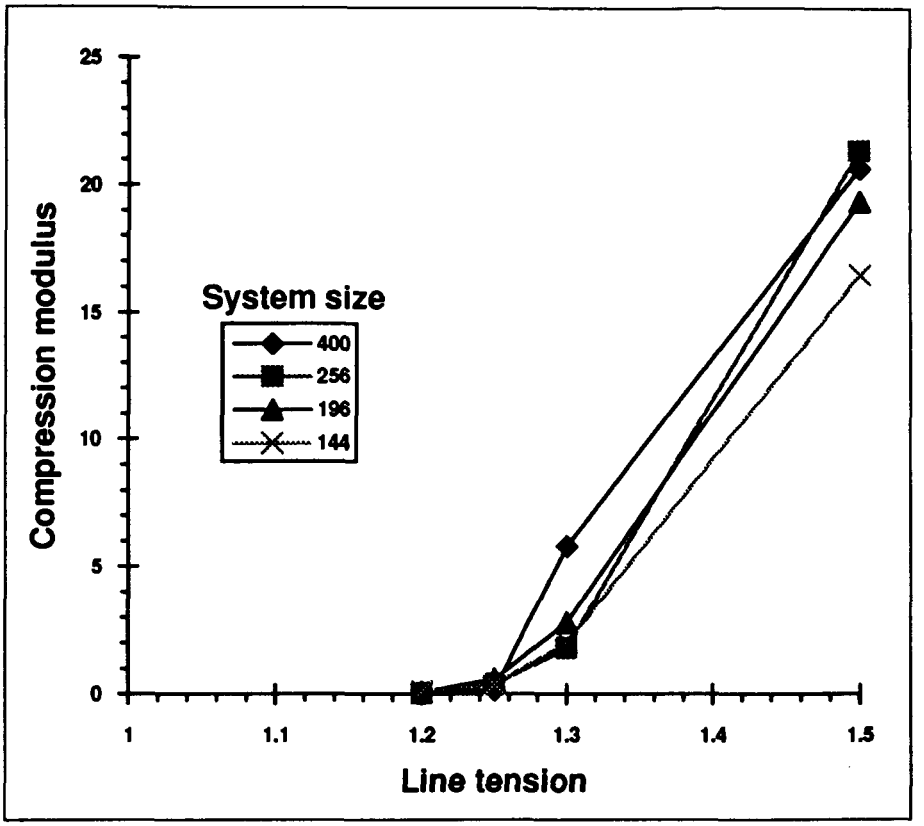

Figure 5.12 Membrane in-plane compression modulus $\beta K a^2$ against line tension $\beta\lambda a$ for system sizes $N = 144, 196, 256, 400$.

5.3.4 *Hole scaling behaviour at zero pressure*

At large line tension, we expect small holes to be approximately circular (or polygonal, as the tethers around the perimeter are taken to be straight edges). At a line tension $\beta\lambda a = 1.4$, somewhat above the transition, the area and radius of gyration of the hole scale with the hole perimeter M_{per} according to $A = A_0 M_{per}^{2\nu}$ and $R_g^2 = R_{g0}^2 M_{per}^{2\nu}$ respectively, with the same exponent $2\nu = 1.80 \pm 0.05$. The area scales with the radius of gyration to the power 1.00 ± 0.05, supporting the equivalence of the scaling exponents for the area and radius of gyration. This shows that the scaling behaviour of small holes has an exponent close to 2, as expected for a quasi-circular object. When the line tension is reduced to $\beta\lambda a = 1.24$, close to the critical line tension at which the membrane ruptures,

the scaling exponents take the value $2\nu = 1.52 \pm 0.05$, showing that the area and radius of gyration of the hole close to the rupture transition scale according to the self-avoiding walk exponent $\nu = \frac{3}{4}$. The area scales with the radius of gyration as 0.97 ± 0.01. The snapshots of the membrane in Figs. 5.4 and 5.5 support these results. The ratio of the prefactors in the scaling laws is estimated to be $\langle A_{hole} \rangle / \langle R_g^2 \rangle = 2.52 \pm 0.03$, independent of the hole size, precluding any collapse of the hole to zero area as the system size increases. Note that for a circular disk this ratio is $A/R_g^2 = \pi$, while for CSAWs it has been calculated analytically to be $A/R_g^2 = 4\pi/5 \approx 2.51$ (Cardy, 1994). The scaling exponents extracted here from the fluctuations in the area of a hole at a fixed system size agree with those shown in Fig. 5.11 which are obtained from four system sizes.

When the line tension is below $\beta\lambda a = 0.6$, the area and radius of gyration of the hole have large average values determined by the system size and the requirement that the membrane remain simply connected. In this regime, the hole area does not fluctuate over a large enough range to allow the extraction of a scaling exponent from one system size.

So far we have discussed the expectations of observables as a function of system size. We next present the frequency distribution of the membrane and hole areas, at fixed system size, in three regimes: above the transition, at the critical line tension, and below the transition. At a line tension $\beta\lambda a = 1.4$, above the transition, the area of the membrane is seen in Fig. 5.13 to be approximately normally distributed, while the hole area, shown in Fig. 5.14, is narrowly distributed around a value close to zero. The hole area distributions for a line tension $\beta\lambda a = 1.24$, close to the transition, and $\beta\lambda a = 0.6$, well below the transition, are shown in Figs. 5.15 and 5.16. The bimodal distribution for the hole area at a line tension $\beta\lambda a = 1.24$, seen in Fig. 5.15, suggests that the hole is fluctuating between two states. The hole area for the membrane with a line tension well below the transition is normally distributed about a large average value as expected.

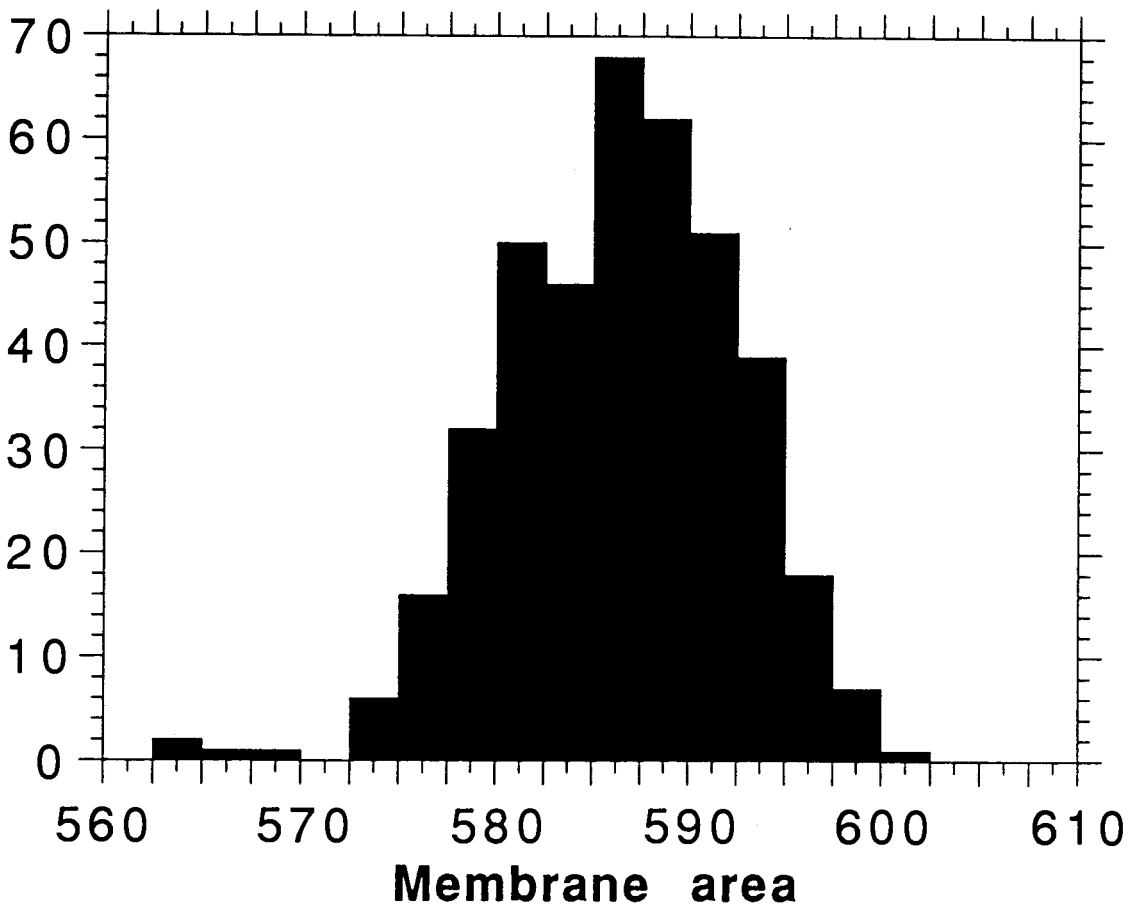

Figure 5.13 Histogram of frequency of occurence of membrane area $\langle A/a^2 \rangle$ at a dimensionless line tension $\beta\lambda a = 1.4$, for a system with 400 vertices. This line tension is above the critical value of $\beta\lambda a = 1.25$, and the membrane area is seen to be normally distributed.

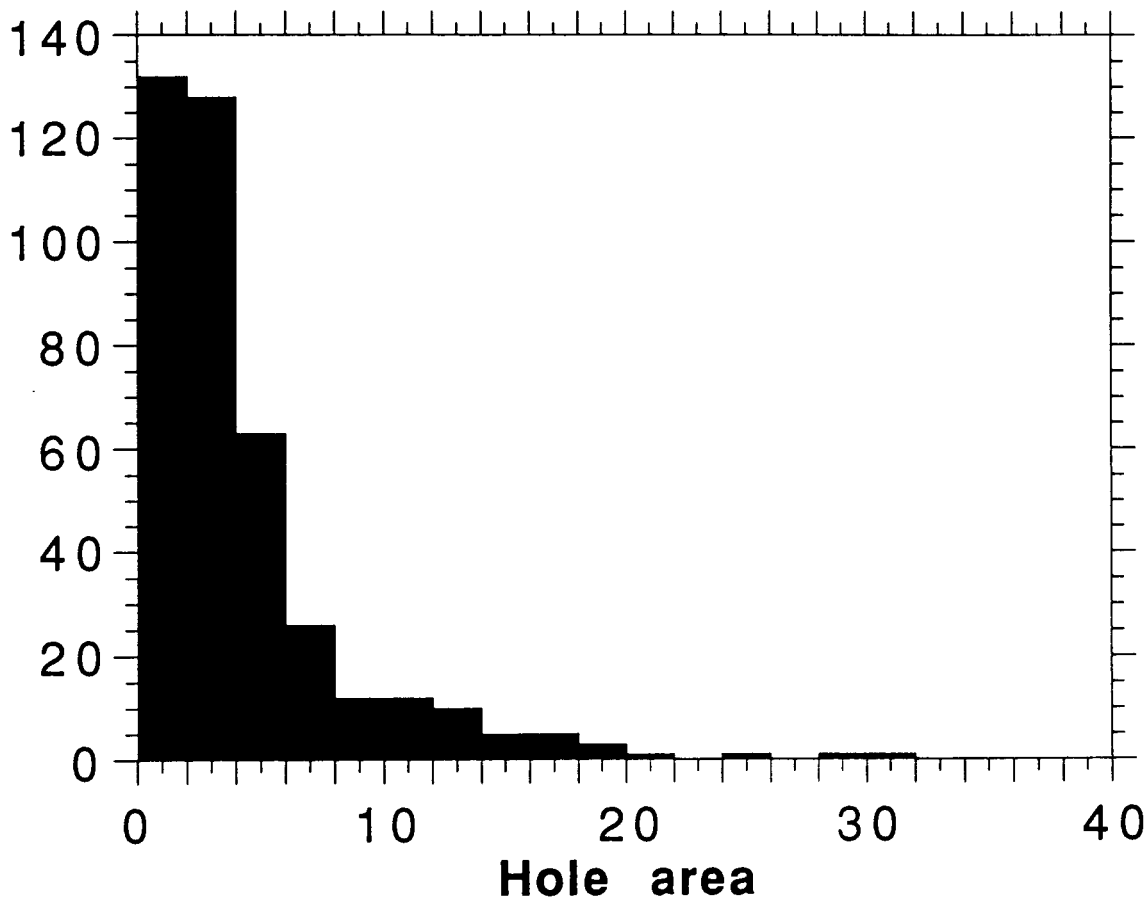

Figure 5.14 Histogram of frequency of occurence of hole area $\langle A_{hole}/a^2 \rangle$ at a dimensionless line tension $\beta\lambda a = 1.4$, for a system with 400 vertices. The hole area is narrowly distributed around a value close to zero.

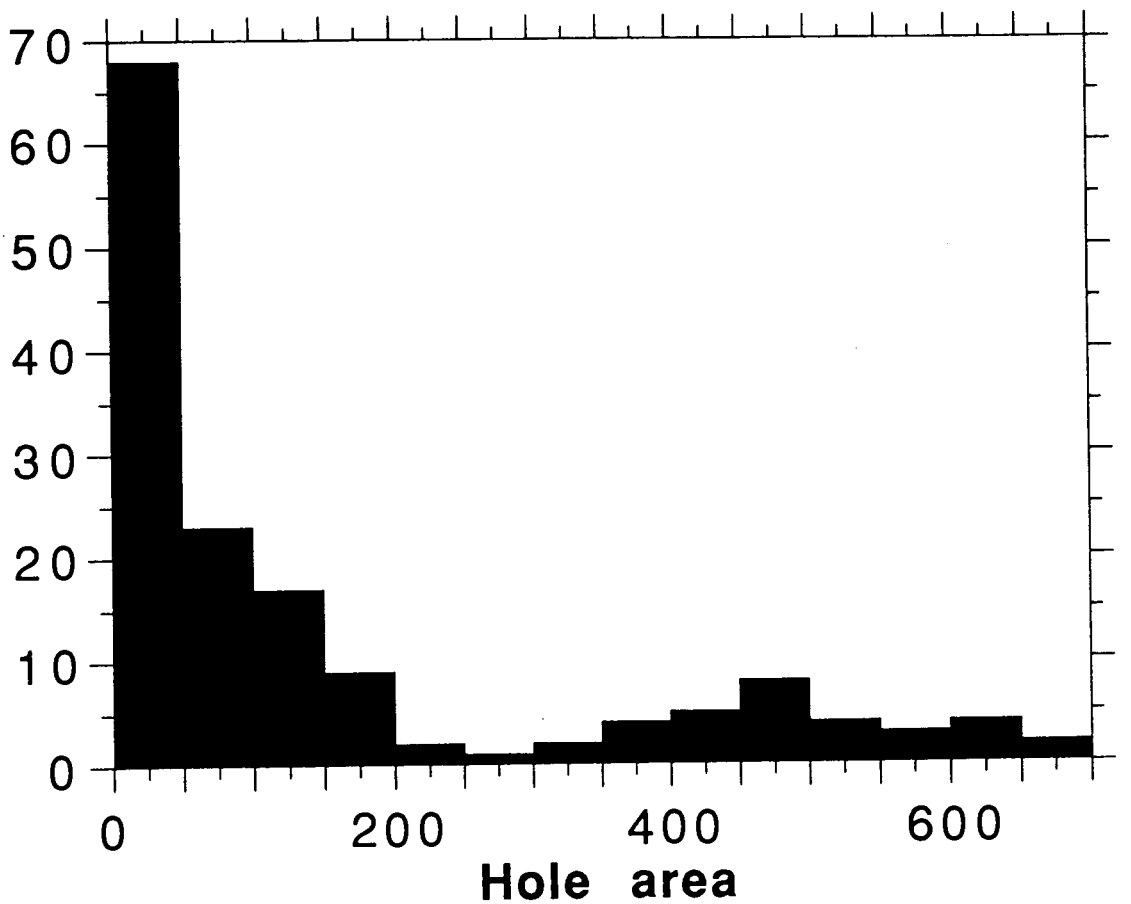

Figure 5.15 Histogram of frequency of occurence of hole area $\langle A_{hole}/a^2 \rangle$ at a dimensionless line tension $\beta\lambda a = 1.24$, for a system with 400 vertices. This line tension is close to the critical value of $\beta\lambda a = 1.25$. The appearance of two peaks shows that the hole is fluctuating between two distinct states.

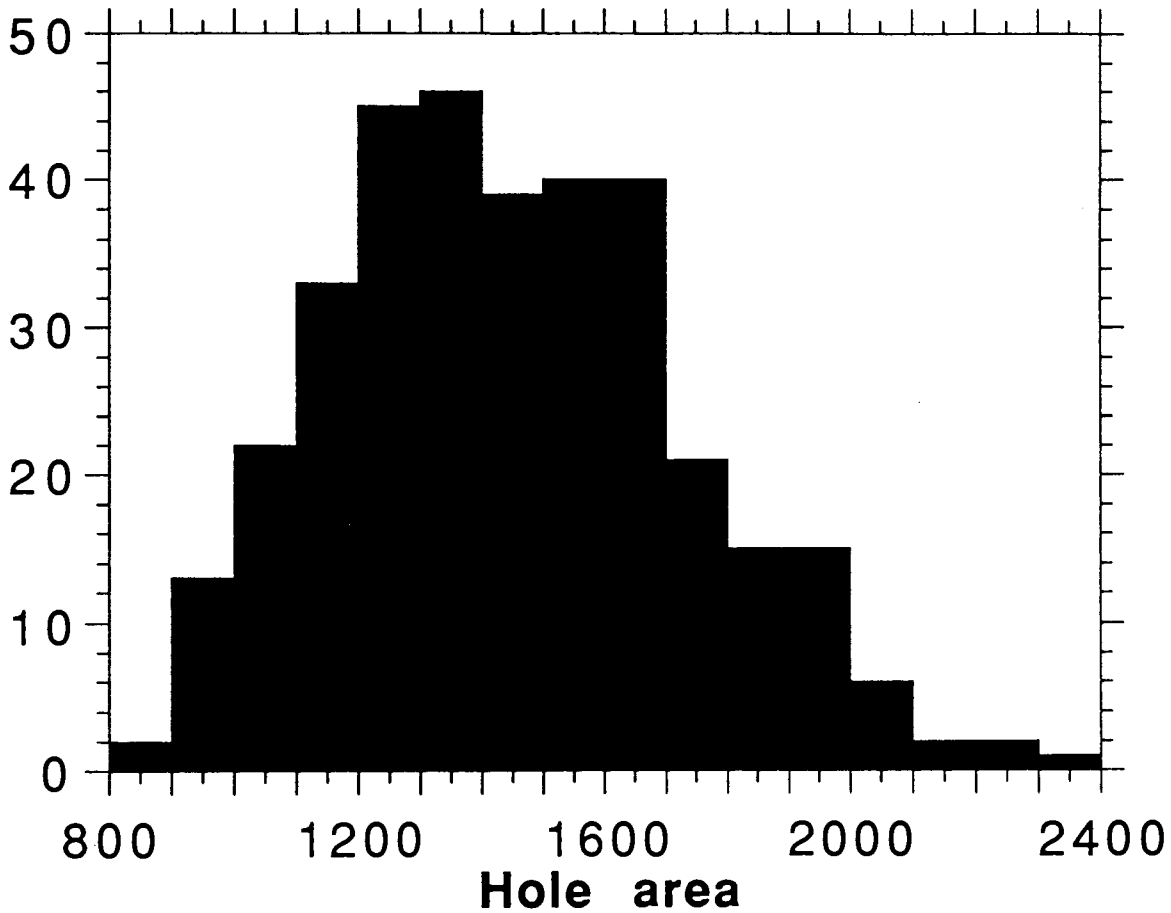

Figure 5.16 Histogram of frequency of occurence of hole area $\langle A_{hole}/a^2 \rangle$ at a dimensionless line tension $\beta\lambda a = 0.6$, for a system with 400 vertices. This line tension is below the critical value of $\beta\lambda a = 1.25$, and the average hole area is large and limited only by the system size.

5.3.5 *Membrane behaviour at positive pressure*

A positive pressure reduces the membrane and hole areas as expected. The average hole area, shown in Fig. 5.17, approaches the minimum hole limit, as the pressure increases, when the line tension $\beta\lambda a \geq 0.8$. We define the minimum hole area as $\frac{\sqrt{3}}{2}\langle s/a \rangle^2$, the area of a hole with four vertices on its perimeter connected by tethers of average length $\langle s/a \rangle = 1.33$. When the line tension $\beta\lambda a \leq 0.6$, the hole area decreases slowly with increasing pressure, but does not reach the minimum hole area up to a pressure $\beta p a^2 = 8$.

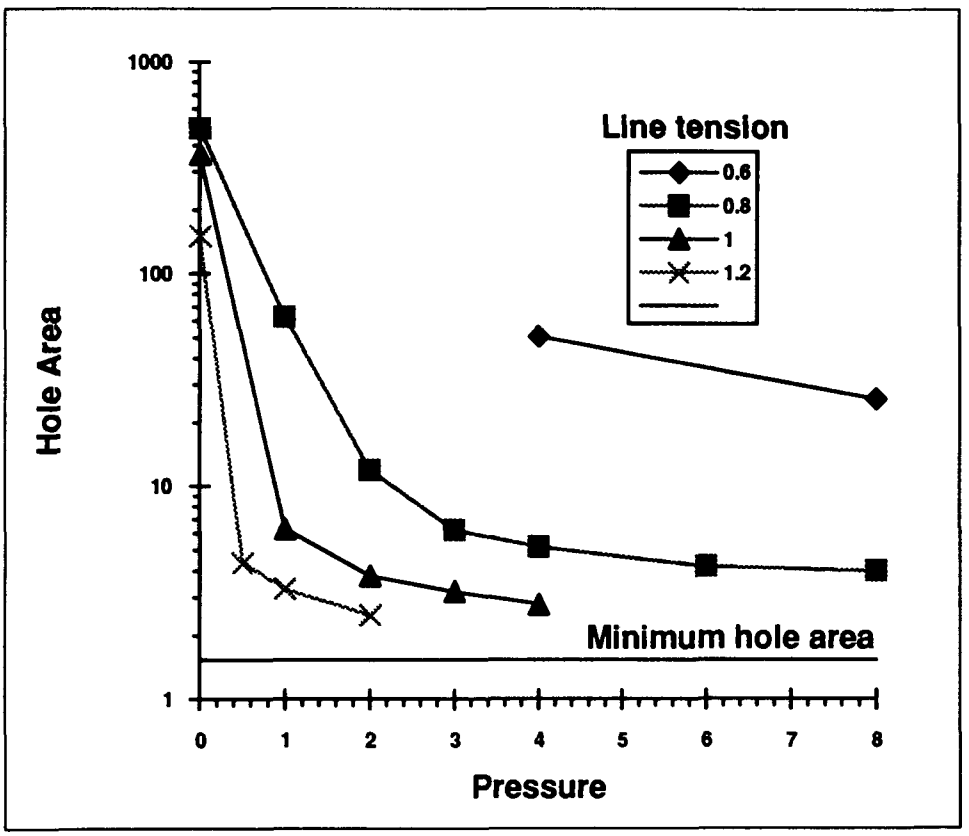

Figure 5.17 Hole area $\langle A_{hole}/a^2 \rangle$ against pressure $\beta p a^2$ for a network with 196 vertices, at several values of the line tension $\beta\lambda a = 0.6, 0.8, 1.0, 1.2$. The minimum hole area for an average tether length $\langle s/a \rangle = 1.33$ is shown for comparison.

The shear modulus of the network remains close to zero[1] for all positive pressures up to $\beta pa^2 = 8$. By contrast, the compression modulus increases dramatically with increasing pressure as shown in Figure 5.18, exceeding the value for a uniform fluid network at zero pressure (obtained from Boal, Seifert and Zilker, 1992), showing that the network is becoming more rigid with increasing pressure. It is interesting to note that the correlation times for the hole area and eigenvalues of its inertia tensor drop to very small

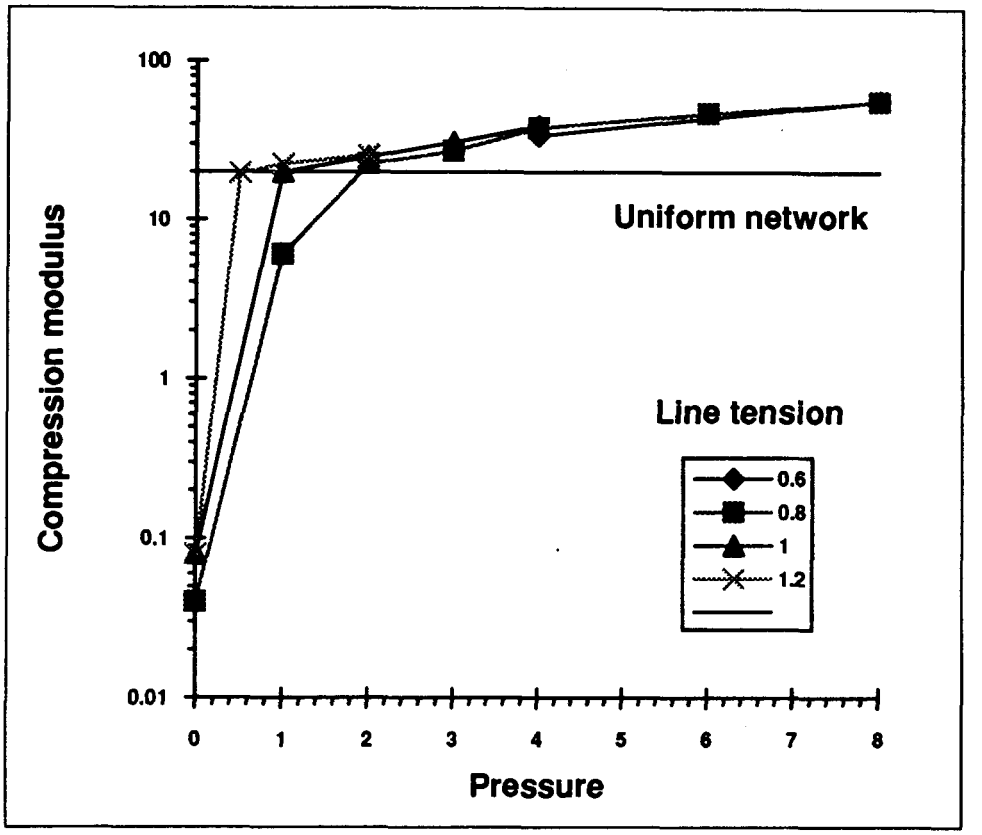

Figure 5.18 Membrane compression modulus βKa^2 against pressure βpa^2 for a network with 196 vertices, at several values of the line tension $\beta\lambda a = 0.6, 0.8, 1.0, 1.2$. The value for a uniform tethered network at zero pressure is shown for comparison.

[1]The shear modulus satisfies $\beta\mu a^2 < 0.01$ for pressures $\beta pa^2 < 8$, and is less than 0.04 at $\beta pa^2 = 8$.

values, typically a few thousand sweeps, when the pressure is non-zero. This is probably related to the increased elasticity in the tethered network when the tethers are stretched or compressed by an external force.

We have examined how the hole area and radius of gyration scale with the system size for networks subject to a line tension and pressure $\beta\lambda a = 0.8$, $\beta p a^2 = 1$ respectively. The results for the area scaling exponent (expected to be unity for a BP, see Leibler, Singh and Fisher, 1987) are 1.08 ± 0.02, 1.07 ± 0.01, 1.03 ± 0.01, 1.004 ± 0.005, and for the radius of gyration (expected to be 1.28, Boal, 1991) 1.25 ± 0.03, 1.25 ± 0.08, 1.10 ± 0.04, 1.13 ± 0.14, for networks with $N = 144, 196, 256, 400$ vertices respectively. Visual inspection of configurations of a membrane under positive pressure reveals that the hole resembles a branched polymer. The change in hole scaling, from a CSAW at zero pressure to a BP at positive pressure, appears for all positive pressures we have used.

5.3.6 Membrane metastability at negative pressure

The analysis in Section 5.2.1, predicts that the network under tension (or negative pressure) is at most metastable, and that the ruptured state is the thermodynamic equilibrium state. The barrier to rupture results from the energy needed to open up the hole against the line tension. At zero temperature, this barrier is described by Eq. (5.3). We have begun to investigate the effect of thermal fluctuations on the network metastability by examining the MC time required for the network to rupture as a function of the pressure.

At a line tension of $\beta\lambda a = 2$ and zero pressure, the barrier against rupture is predicted to be infinite by the zero temperature calculation of Section 5.2.1. At the same line tension and a pressure $\beta p a^2 = -1$, the barrier height for circular holes is predicted to be $E^*/\lambda a \approx 6.3$, and the critical hole perimeter at rupture is $2\pi R^*/a \approx 12.6$. At finite temperature, we estimate the relative probability for the spontaneous appearance of a hole

of the critical size using the Boltzmann factor $\exp(-\beta E^*) \approx 3\times10^{-6}$. The barrier height is thus about $13k_BT$. We expect that the non-circular configurations of the hole perimeter at finite temperature will lower the barrier height from this value, and we can estimate the entropic contribution by using the results of our simulations.

For a line tension and pressure of $\beta\lambda a = 2$ and $\beta p a^2 = -1$, the average time[2] to rupture of a network with 196 vertices is $(14\pm14)\times10^4$ sweeps. The distribution of waiting times prior to rupture is consistent with an exponential distribution. We find that the network does not rupture until the hole has at least 13 bonds on its perimeter. If we assume that each bond requires an energy $\beta\lambda a = 1.25$ to be cut (the zero pressure critical line tension), and that this must be balanced by the entropy gain of the hole perimeter, the approximate entropy of the critical size hole can be obtained from

$$TS_{hole} \approx E_{bonds} \approx 17.$$

The entropy created by fluctuations of the closed self-avoiding walk hole boundary thus reduces the barrier height from its zero temperature value, $E_{hole} \approx 26$ (given $\lambda a = 2k_BT$) and the PA term reduces it further. The barrier height against rupture of the membrane, as measured by the MC time prior to rupture, decreases with increasing tension as expected. When the pressure is $\beta p a^2 = -1.2$, the average time to rupture drops to $(4\pm3)\times10^4$ sweeps (again averaged over 50 simulations).

We may estimate the area change of the network due to the applied pressure and compare it with the experimentally observed value of 5% (Needham and Hochmuth, 1989; Hallett et al., 1993). When the line tension is $\beta\lambda a = 10$, preventing the appearance of a hole, and the pressure is $\beta p a^2 = -1.2$, the average area per triangle in the (stretched) network is $\langle A\rangle/N_\Delta = 0.7850\pm0.0005$. This may be compared to the value at zero

[2]The average is taken over 50 independent simulations, for each of which the initial state is taken from a previous simulation, with the minimum hole, at the same line tension and pressure.

pressure (given on page 117) of $\langle A \rangle / N_\Delta = 0.7366 \pm 0.0005$. This represents a change of 6.6%. We may also estimate the area change from the compression modulus of the network. We have $\Delta A/A \approx \Delta p/K$, and the compression modulus obtained from the simulation of the stretched network is $\beta K a^2 = 19.0 \pm 1.5$, which gives an area change of 6.3%.

5.4 Discussion

5.4.1 Membrane stability at zero pressure

The zero temperature calculation in Section 5.2.1 predicts that, in the absence of tension, the energy of a model membrane is a monotonically increasing function of the hole radius. Spontaneously occurring large holes are suppressed by the energy cost arising from the line tension around the hole perimeter. By contrast, the finite temperature calculation in Section 5.2.2 predicts that a minimum line tension is necessary to prevent the appearance of a hole that ruptures the model membrane, even when the applied tension is zero. The spontaneous appearance of a large hole may reduce the membrane free energy because of the entropic contribution of the hole boundary. We have investigated the effect of thermal fluctuations and tension on the rupture of a model fluid membrane using Monte Carlo simulations.

We can qualitatively predict the behaviour of a model membrane with a single hole by constructing its effective free energy, and calculating the relative contributions of the energy cost, and entropy gain, of the hole perimeter. In Section 5.2.2 we have used a result from lattice counting of the number of configurations of closed loops on a planar triangular lattice to give a functional form for the entropy of the hole boundary. In order to compare the critical line tension derived in Section 5.2.2 with the simulation results, we need values for the constants in Eqs. (5.6)-(5.9). We have assumed that the hole perimeter scales as a closed self-avoiding walk, and so $\alpha = \frac{1}{2}$ and $z = 4.15$ as given by McKenzie

(1976). These values are used to construct the curves in Fig. 5.2, although their qualitative appearance does not depend crucially on the exact values of α and z. In fact, the critical value of $\beta\lambda a$ depends only on the effective lattice constant z, and not on the exponent α, so other scaling forms for the hole perimeter, such as a branched polymer, would also predict a transition at $\beta\lambda a$ of order unity.

Note that for line tensions which make the first term in Eq. (5.7) positive, the free energy of the membrane is again a monotonically increasing function of hole size. It is clear from Fig. 5.2 that as the line tension approaches the critical value $\beta\lambda a = \ln 4.15 \approx 1.4231$ from above, there is a steep drop in the dimensionless barrier height from infinity to a number of order unity that allows a hole to grow and rupture the membrane.

Simulations at zero pressure show that the membrane is stable against hole formation for line tensions larger than a critical value $\beta\lambda a = 1.25 \pm 0.05$. In this regime, the Boltzmann weight for the spontaneous appearance of a hole progressively suppresses larger holes. The critical line tension found in the simulations is only 12% smaller than that predicted by the finite temperature model of Section 5.2.2, and corresponds to a biological line tension of 2.5×10^{-7} dyn, or 2.5×10^{-12} N, assuming a typical length-scale of 2 nm. We do not expect better agreement between the calculation and the simulations because of the error introduced by the use of a lattice counting argument for a continuous quantity (the hole boundary), embodied in the parameter z, the effective lattice constant. Also, the asymptotic formula Eq. (5.6) overestimates the number of conformations of a closed loop for the small holes (only tens of monomers on the hole boundary) that occur in the systems we investigate (144 to 400 vertices in the network). Small holes are almost circular, and this reduces the number of configurations below that predicted by Eq. (5.6) by a factor of between 10 and 100. Nevertheless, the agreement between the theory and simulations is very good. When the line tension is zero, any spontaneous fluctuation that increases the

hole size lowers the membrane free energy because of the consequent increase in entropy of the hole boundary at zero energy cost. In this regime, the model membrane disintegrates, and the membrane in the simulations breaks up into a thin mesh surrounding the hole, which is of the order of the system size.

A first-order open-to-closed transition has been found previously in three dimensional fluid vesicle simulations (Boal and Rao, 1992b), although our value for the critical line tension required for closure of the hole, $\beta\lambda a = 1.25$, is 25% larger than the value, $\beta\lambda a = 1.00$, obtained for the three-dimensional membrane[3]. The simulation techniques are almost identical and cannot account for the difference in the critical value of $\beta\lambda a$. For example, we have checked that increasing our maximum tether length from $s_0 = 1.688a$ to $1.72a$, closer to $s_0 = 1.732a$ used by Boal and Rao, changes the critical line tension by less than 0.05.

It is possible that the relative entropy change between the open and closed states of a vesicle in three dimensions, is less than the corresponding change when a hole appears in a membrane in two dimensions. A fluid vesicle in three dimensions scales as a branched polymer regardless of whether it is open or closed, so the removal of the fluctuations of the membrane boundary when the vesicle closes does not change its scaling behaviour, although it may change its free energy considerably. The closure of the hole in the two-dimensional sheet eliminates the branched polymer scaling behaviour of the open membrane, and hence changes its entropy substantially.

5.4.2 Hole scaling behaviour at zero pressure

The area of a hole in a three-dimensional open vesicle is not well-defined, but it is unambiguous in a planar membrane. Inspection of membrane configurations, illustrated in

[3]Our dimensionless line tension $\beta\lambda a$ is equivalent to $\kappa_{len} a$ in Boal and Rao (1992b).

Figs. 5.4 and 5.5, and the scaling behaviour of the membrane area in Fig. 5.10, suggest that the bulk membrane has branched polymer scaling behaviour when a large hole is present, for sufficiently large system sizes. This is supported by the collapse of the hole perimeter to a single curve when scaled by the system size shown in Fig. 5.6. The area and radius of gyration of the hole, by contrast, are seen in Figs. 5.8 and 5.9 not to collapse to a single curve when scaled with the system size. When plotted as functions of the hole perimeter, for line tensions close to the critical value, the area and radius of gyration of the hole are both found to scale with the exponent $2\nu = 1.52 \pm 0.05$, as expected for a closed self-avoiding walk. When the line tension is below the critical value, the scaling exponent of the hole area and radius of gyration is typically 1.35 ± 0.10.

We conclude that the area of a planar membrane at zero pressure, changing from an unbroken state to a ruptured state is governed by branched polymer scaling laws. This shows that the open-to-closed transition in a model fluid membrane in 2D is the same as that of a fluid vesicle with zero rigidity and zero pressure in three dimensions (Boal and Rao, 1992b). The area of the hole in the planar membrane, however, scales with its boundary as a CSAW at the transition, and does not change to a BP even when the hole is large, and the line tension is well below the critical value.

The scaling behaviour of a ring polymer has been investigated by several groups (Leibler et al., 1987; Fisher, 1989; Camacho et al., 1991). A ring polymer is analogous to the hole boundary in our simulations. Leibler and co-workers (1987) found that the area and radius of gyration of a ring polymer with zero rigidity are well described by the scaling laws

$$A \approx N^{2\nu} Y\left(\bar{p} N^{\phi\nu}\right), \tag{5.18}$$

$$R_g^2 \approx N^{2\nu} X\left(\bar{p} N^{\phi\nu}\right), \tag{5.19}$$

in which $\overline{p} = \Delta p a^2 / k_B T$, and ν is the standard end-to-end length exponent for open SAWs. Note that the convention for the sign of the pressure in Leibler et al. (1987), $\Delta p = p_{\text{int}} - p_{ext}$, is the opposite of ours. The exponent ν is believed to be $\frac{3}{4}$ (see Nienhuis, 1982; Duplantier, 1990), and they find $\nu = 0.755 \pm 0.018$. They also find that $\nu_A / \nu = 1.007 \pm 0.013$. Because the pressure couples to the area they expect the exponent ϕ to be 2. They estimate $\phi = 2.13 \pm 0.17$. The scaling functions $X(x), Y(x)$ are different for different regimes. At zero pressure they find

$$\begin{aligned} X(0)/a^2 &= 0.116 \pm 0.008, \\ Y(0)/a^2 &= 0.29 \pm 0.02. \end{aligned} \tag{5.20}$$

This precludes a collapse of the ring $A/R_g^2 \to 0$ as $N \to \infty$, and they conclude that the ring polymer does not take up a branched polymer configuration at zero pressure. We find[4] the ratio $A/R_g^2 = 2.52 \pm 0.03$, and this compares well with their result $A/R_g^2 = 2.50 \pm 0.24$. In the deflated regime, $\Delta p < 0$, they find

$$\begin{aligned} X(x) &\approx X_- / x^{\sigma}, \\ Y(x) &\approx Y_- / x^{\tau}, \end{aligned} \tag{5.21}$$

with $\sigma = 0.13 \pm 0.05$, $\tau = 0.25 \pm 0.04$. These values are indicative of a collapse into a branched polymer state, and this collapse is also found in our simulations (and discussed in Section 5.4.3 to follow). The agreement between the scaling behaviour of a ring polymer and the hole boundary within a bulk network in two dimensions, suggests that the network surrounding the hole perimeter is irrelevant to the scaling properties of the hole area at the open-to-closed transition.

[4]We have used 16 simulations of a 400 vertex network at line tensions $\beta\lambda a = 0.8 - 1.5$.

5.4.3 *Membrane behaviour at positive pressure*

When the membrane is placed under positive pressure, i.e., compression, its area decreases and its compression modulus increases, as shown in Figs. 5.17 and 5.18. When the line tension is just below the critical value $\beta\lambda a = 1.25$, application of a positive pressure to the membrane causes the hole perimeter to shrink, and its area to maintain a value close to the minimum allowed in the simulations. For line tensions in the range $0.6 < \beta\lambda a < 1.2$, and pressures $\beta p a^2 < 2$, the hole perimeter is large, although its area is small relative to its size at zero pressure. Inspection of membrane configurations shows that the hole is still present. When the line tension is less than $\beta\lambda a = 0.6$, the hole remains large in spite of applied pressures up to $\beta p a^2 = 8$. For all positive pressures we have investigated, the hole area, if sufficiently large, scales with its perimeter as a branched polymer. A typical example has the exponent 1.04 ± 0.03 for a membrane subject to a pressure $\beta p a^2 = 1.0$ and line tension $\beta\lambda a = 0.8$. This agrees with the results of Leibler, Singh and Fisher (1987) as described in the previous section.

The scaling behaviour of the hole in the fluid membrane thus changes from that of a CSAW at zero pressure, to a BP at positive pressure. Under compression, so that the hole area is small relative to its zero pressure value, the membrane behaves as a uniform, fluid network, as shown by the compression modulus which has values in excess of the uniform fluid network value $\beta K a^2 = 20$. The increased compression modulus reflects the fact that the hard-core vertices are constrained to occupy a smaller average area under positive pressure. The existence of the hole becomes irrelevant in this regime, as the vertices in the network are as close together as if the hole were absent.

5.4.4 *Phase diagram of membrane under tension*

We can combine some of our results into a tentative phase diagram, Fig. 5.18, for the stability of a fluid network subject to an applied pressure at finite temperature. At zero pressure, a minimum line tension of $\beta\lambda a = 1.25$ is required to stabilise the unbroken network against hole formation. Under compressive pressure, the average hole area for a given line tension decreases with increasing pressure. Below a line tension $\beta\lambda a = 0.6$ the hole area remains large even at a pressure of $\beta p a^2 = 8$, although smaller than it would be at zero pressure. A hole at finite pressure is represented as "closed" if its area differs by

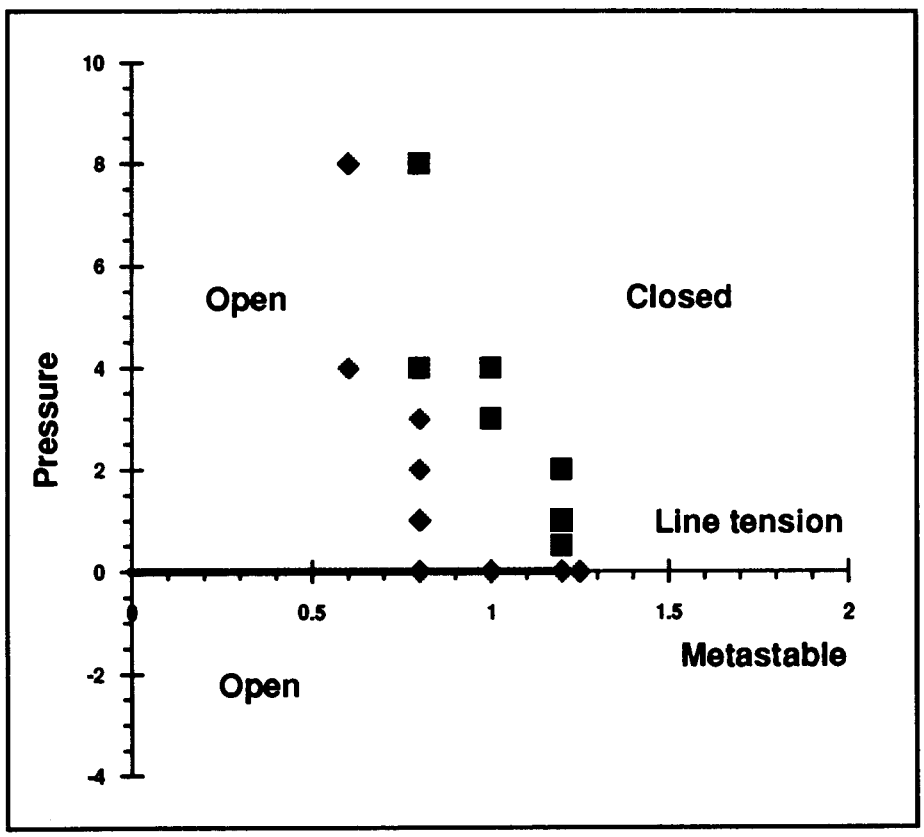

Figure 5.19 Phase diagram for rupture of a model fluid membrane in two dimensions as a function of the line tension around the hole $\beta\lambda a$ and pressure $\beta p a^2$. At zero pressure, the membrane scales as a self-avoiding, branched polymer (BP) for line tensions between zero and a critical value $\beta\lambda a = 1.25$. Above the critical line tension the membrane contains only small holes. (■ closed membrane, ♦ open membrane) See the text for discussion of metastability.

less than a factor of two from the minimum hole area in the unbroken network.

We can relate the transition of the model membrane from an unbroken state to a ruptured state to the experimental work on cell lysis. The fluid lipid bilayer that surrounds a cell is stabilised by the hydrophobic effect of lipids in an aqueous solution that makes it unfavourable for them to leave the bilayer and solubilise. Experiments have shown that red blood cells and vesicles rupture when a lateral tension of 2-15 dyn/cm is created in the lipid bilayer[5](Evans and Needham, 1987; Needham and Hochmuth, 1989). The line tension that acts to close up holes in the bilayer has also been measured (Zhelev and Needham, 1993), and has values in the range $1-3\times10^{-6}$ dyn, depending on the lipid composition of the bilayer. When such values are used in the zero temperature calculation in Section 5.2.1, they predict a barrier height to rupture of the order of tens to hundreds of k_BT. Thermal fluctuations are clearly ineffective at initiating rupture against barriers of this height. Nevertheless, we observe that the model membrane does rupture in the absence of an applied tension.

5.4.5 Rupture of membrane under tension

When the membrane is placed under tension, our simulations show that the barrier height to rupture is reduced from the zero temperature value to approximately zero by the entropy of the hole perimeter. The critical hole size does not change significantly. We find that the fractional area change of the membrane prior to rupturing, approximately 6%, agrees with that observed in osmotic pressure gradient experiments (Hallett et al., 1993), but is larger than the value of 3% observed in electroporation experiments (Needham and Hochmuth, 1989). We are unable to convert the MC time to rupture into estimates of the membrane's dynamical behaviour without making an estimate of the membrane viscosity. However, the distribution of waiting times for rupture in the simulations shows a wide

[5]These tensions are for lipids in the L_α phase appropriate to physiological temperatures; the range of values apply to vesicles composed of different lipids.

statistical variation that is also seen in experiments (Wilhelm et al., 1993). Wilhelm et al. conclude from the linear dependence of the membrane conductance with time, that only a single hole is required to rupture a membrane, which suggests that the rupture process at finite temperature, and tension, modelled in our simulations may be a reasonable approximation to the experimental scenario.

5.5 Summary

Experiments have shown that imposing a lateral tension on the fluid bilayer of a vesicle or cell causes it to rupture by the occurrence of one or more holes. The barrier height between an unbroken, stretched membrane and the ruptured state in several zero temperature models is predicted to be of the order of $25-450k_BT$. In this chapter we have described zero and finite temperature calculations of membrane stability at zero pressure, and presented the results of Monte Carlo simulations that explore the effects of thermal fluctuations on the rupture process.

We have also presented results for membranes subject to a hydrostatic pressure at finite temperature. Previous work in three dimensions has found a transition from an open membrane to a closed sphere as a function of the line tension around the membrane boundary. We have worked in two dimensions to investigate the behaviour of the hole, which is not well-defined for a three-dimensional vesicle, and to allow the effects of pressure on the membrane to be explored.

We model the fluid membrane as a network of vertices, confined to two dimensions, connected by tethers that are allowed to change their connectivity. The energy of the tethers is zero unless they are stretched beyond a maximum length, and the network is self-avoiding. The network is subject to a hydrostatic pressure or tension, and a single hole is allowed to grow, subject to a line tension imposing an energy cost per unit length on the hole perimeter.

A finite temperature calculation predicts, and we find in simulations, that there is a critical value of the line tension, independent of the system size, at which the hole size changes abruptly. The predicted and measured values of the critical line tension differ by approximately 12%. For line tensions larger than the critical value $\beta\lambda a = 1.25 \pm 0.05$, the hole remains negligibly small. The membrane area scales with its perimeter as a self-avoiding branched polymer for all line tensions from zero up to the critical value. The hole area and radius of gyration, by contrast, scale with self-avoiding walk exponents at the transition, and for line tensions $\beta\lambda a < 1.0$, the exponents, although reduced, are still well above the branched polymer value of unity.

Under compressive pressure, the hole area, when sufficiently large, scales with its perimeter as a branched polymer from zero line tension up to the critical value, as found previously for simulations of ring polymers in two dimensions. Under a negative (stretching) pressure, the network becomes metastable. We have investigated the change in the barrier height against rupture for a membrane under tension, and find that thermal fluctuations reduce the barrier height significantly, while the critical hole size is relatively unchanged. The fractional area change of the membrane prior to rupture is approximately 6% similar to that found in rupture experiments.

CHAPTER 6

CONCLUSIONS

The specific conclusions arising from each of the projects described in this thesis have been presented in the relevant chapters. We collect here some thoughts about the implications of the results we have obtained, and pointers for possible future work.

6.1 Phase transitions in discotic liquid crystals

Discotic liquid crystals were first synthesised over fifteen years ago, and yet understanding of the molecular characteristics that make possible their several distinct mesophases remains incomplete. Our computer simulations have revealed that, unlike real liquid crystals, hard-core anisotropy alone is sufficient to produce a nematic phase in a liquid of disk-like molecules in three dimensions, subject to a hydrostatic pressure, when the disk thickness is less than 40% of its radius. Real discotic liquid crystal molecules appear to require long, hydrocarbon chains attached to a central, rigid core to produce a nematic phase. Long-range attractive forces may help to stabilise a mesophase, while molecular flexibility may act to destabilise the ordered mesophases with respect to the liquid phase. These effects have not yet been included in computer simulations because of the consequent dramatic increase in computing time required. Such effects need to be included in simulations if the stability of real mesophases is to be related to molecular models more realistic than the current anisotropic, hard-core potentials.

The isotropic-nematic transition is absent for disks with a thickness to radius ratio of 20%, constrained to lie at an interface between two immsicible fluids, and with a differential interaction for the two fluids. This is somewhat unexpected given that previous work on a restricted model showed signs of nematic ordering in a set of disks at an

interface. The increased orientational freedom of the disks in three dimensions appears to reduce the tendency of the disks to align that results from their anisotropic shape.

The investigation of disks with a differential attraction for two fluids illustrates the problems associated with computer simulations of anisotropic molecules with energetic interactions. The molecular ansiotropy creates potential energy minima that allow neighbouring molecules to become computationally "stuck" in a simulation. Such groups of molecules can be very difficult to break up, and this can greatly slow the approach of the system to its equilibrium distribution. The potential energy can also contain narrow minima that are not easily sampled in a Monte Carlo simulation, resulting in a non-equilibrium distribution of the system amongst its energy states. These problems do not occur in systems with purely hard-core repulsive forces. For these and other reasons simulations of anisotropic molecules have tended to use only hard-core interactions. Models of the interactions between amphiphilic molecules necessary for simulations of biological systems may have to include long-range forces, such as the Coulomb interaction amongst charged lipid headgroups, and this suggests that pure Monte Carlo simulations may not be appropriate for such systems. Combined Monte Carlo-Molecular Dynamics simulations have been found to have faster convergence to equilibrium than pure Monte Carlo simulations, and may prove more adept at simulating complex molecular interactions.

6.2 Elastic properties of polymerised membranes

We have investigated the effects of temperature and hydrostatic pressure on a triangulated network of Hookean springs embedded in two dimensions. A mean field theory of a network composed only of equilateral triangles predicts the elastic properties of the zero temperature, or highly stretched, self-avoiding network quite well. The phantom network, in which the springs are allowed to overlap, agrees with the MFT at

high tension, but collapses to a very small area at a finite, temperature-dependent tension. The lowest-order, finite temperature correction to the MFT brings its predictions closer to the simulation results, but the behaviour of the network is not dominated by equilateral triangles except at very low temperatures. In particular, the variation of the elastic moduli with pressure is quite different from the zero temperature MFT prediction. Extending the MFT to include non-equilateral triangles may improve the description of the pressure-dependence of the network elastic moduli at finite temperature. Such work is currently underway (Discher, unpublished).

The elastic properties of a two-dimensional network of vertices interacting via a square-well potential has been investigated recently (Boal, Seifert and Shillcock, 1992). The elasticity of this network is entropically generated, in contrast to the network of Hookean springs investigated here, and its resistance to deformation increases without limit as the strain approaches a finite value determined by the tether length. The Poisson ratio of both types of network is negative for a large range of applied tension, and both networks also exhibit the collapse transition when the self-avoidance of their bonds is removed. Unlike the Hooke's law network, which is amenable to approximation by MFT at zero and finite temperatures, the square-well network has no temperature scale and no unique ground-state. While being perhaps easier to simulate, the square-well network is plagued by extremely long correlation times. The short correlation times of the Hooke's law network permits the simulation of larger system sizes and the inclusion of more complex interactions.

The behaviour of the membrane-associated cytoskeleton of a red blood cell has recently been modelled as an hexagonally-connected network of chains attached to a flat surface representative of the fluid bilayer (Boal, 1994). Each chain is flexible, being composed of a fixed number of hard beads connected by tethers. The attachment of the network to the bilayer plane is taken at the midpoints of the chains. Recent experiments

(Mohandas, unpublished) suggest that the spectrin network in an RBC is attached to the bilayer by protein band 4.1 at the junction vertices, instead of, or possibly as well as, at the midpoints of the spectrin tetramers. The 2D networks investigated here represent a first approximation to the RBC cytoskeleton, but appear to capture the behaviour found in more complex models. The Hookean network is a good model of a cytoskeleton under moderate stress, as long as its area is within a factor of two of the unstressed, equilibrium value. The cytoskeleton under large tension is more accurately modelled by a square-well network which captures the inextensiblity of the protein chains. Detailed simulations of the RBC cytoskeleton are underway (Boey, unpublished) and preliminary comparison shows that the 2D networks investigated here provide a good description of the more detailed simulations.

6.3 Fluid membrane stability and rupture

Fluid membranes have been investigated as a natural extension of work on polymers and polymerised membranes. The lipid bilayer surrounding a cell is a fluid and has provided motivation for such investigations. Experiments have induced rupture of the lipid bilayer in vesicles or cells by the application of an electric field or osmotic pressure gradient between the inside and outside of the cell. Rupture of the bilayer is opposed by the hydrophobic effect of the lipids that creates a line tension around the boundary of any hydrophilic hole that opens in the membrane. The results of rupture experiments have commonly been interpreted using a zero temperature model to calculate the barrier height against rupture, and the critical hole size.

We have used Monte Carlo simulation to investigate the effect of thermal fluctuations on the properties of a model fluid membrane. We have found that the membrane is unstable to forming a large hole when the line tension is less than a critical value, $\beta\lambda a = 1.25 \pm 0.05$, even at zero pressure. Below this line tension, the membrane has

the appearance, and scaling behaviour, of a self-avoiding branched polymer as found previously for three dimensional vesicles. When the network is subject to a compressive pressure the hole area shrinks, and closes up within the accuracy of the simulations for line tensions within 25% of the critical value. The scaling behaviour of the hole area changes from that of a closed self-avoiding walk at zero pressure to a branched polymer at finite pressure.

When the network is subject to a stretching pressure or tension, it becomes metastable to rupture, as found in electroporation experiments. The MC time needed for the network to rupture varies strongly with the line tension and pressure. For typical values of the line tension we find that thermal fluctuations significantly reduce the barrier height from the zero temperature prediction of tens to hundreds of $k_B T$. The fractional area change of the membrane prior to rupture is similar to that found in experiments.

Many cellular processes involve the formation of holes in the fluid membrane, and the stability of the fluid lipid bilayer to chemical and other stressors. A detailed understanding of the physical processes involved is just beginning. The edge energy of lipids on a hole boundary arises from a complex set of interactions amongst diverse molecules and is altered by the addition of lipids of different character from those composing the bilayer. The edge energy also may not be a constant as has commonly been assumed, but may vary with hole size. In addition, there are electrostatic interactions amongst the lipids and proteins that have so far been ignored. Such interactions are difficult to model accurately because of their long range, and the co-operative effects of the distinct forces. It is the combination of several weak forces that stabilises biological processes, such as protein folding, and enables cells to operate their biochemical machinery. Such systems cannot be accurately treated as being dominated by a single force subject to small perturbations from other forces.

Improved models of biological membranes are needed to understand and explain advances in medical therapeutic techniques. The ease of permeabilisation of a fluid membrane has been linked to the onset of respiratory distress syndrome in infants (Exerowa et al., 1992); cell membrane damage resulting from electric burns is being treated via chemicals that act to reseal holes formed in the lipid bilayer (Lee et al., 1992, 1994); and drug delivery by injected liposomes is an area of active research (Lasic, 1992; Litzinger and Huang, 1992). The interactions amongst the lipids, proteins and other surfactants in the cell plasma membrane are complicated, and the use of computer simulations allows their separate components to be isolated and investigated systematically.

APPENDIX A

MONTE CARLO SIMULATIONS

In this thesis we have used computer simulations to investigate some of the thermodynamic properties of three simple model systems. Nicholas Metropolis devised an algorithm in the 1950s to simulate a system of disks in a square box with periodic boundary conditions that is now almost universally known as the Metropolis Monte Carlo (MC) algorithm (Metropolis et al., 1953). An extensive review of applications of the MC method is given by Binder (1986, 1987). In this appendix we describe the Metropolis MC technique. We also define the autocorrelation function of an observable, and show how it may be used to estimate the reliability of the results of a simulation.

A.1 Metropolis Monte Carlo algorithm

The basic problem in classical statistical mechanics is the evaluation of the partition function of a system. The thermodynamic quantities of interest may then be obtained from this function and its derivatives. We first calculate the partition function for a system at constant volume, and then extend the method to a system maintained at constant pressure.

Consider a box of fixed volume containing N particles interacting via a specified central potential $U(\{r_{ij}\})$, that depends on the set of inter-particle distances $\{r_{ij}\}$. The partition function is defined as

$$Z = \frac{1}{N!h^{3N}} \int d^{3N}p\, d^{3N}q \exp(-\beta H), \qquad \text{(A.1)}$$

where (p,q) are the canonical momentum and position coordinates of the N particles, h is Planck's constant, β is the inverse temperature $(1/k_BT)$, k_B is Boltzmann's constant, and H is the Hamiltonian of the system

$$H = \sum_{i \neq j} \left[\frac{p_i^2}{2m} + U(r_{ij}) \right], \tag{A.2}$$

where m is the mass of a particle, r_{ij} is the distance between particles i and j and the position coordinates are restricted to lie within the volume of the box. The thermodynamic quantities of interest are derived from the Helmholtz free energy

$$A = -k_B T \ln Z. \tag{A.3}$$

This is the free energy appropriate to a system held at constant particle number, volume and temperature (the NVT ensemble).

When the potential $U(\{r_{ij}\})$ is independent of the particles' momenta, the momentum degrees of freedom can be integrated out to give

$$Z = \exp(-\beta A) = \frac{1}{N! \lambda^{3N}} Q_V, \tag{A.4}$$

$$Q_V = \int d^{3N} q \exp\left(-\beta \sum_{i \neq j} U(r_{ij}) \right), \tag{A.5}$$

where $\lambda = \left(\frac{h^2}{2\pi m k_B T} \right)^{1/2}$ is the thermal wavelength and Q_V is the configuration integral.

Evaluation of the free energy and its derivatives is reduced to the problem of integrating Eq. (A.5) given the form of the inter-particle potential. For example, the equilibrium value of an observable $\langle X \rangle$ in the NVT ensemble is

$$\langle X \rangle = \frac{\int d^{3N} q \, X \exp\left(-\beta \sum_{i \neq j} U(r_{ij}) \right)}{Q_V}. \tag{A.6}$$

However, evaluation of integrals of the form of Eq. (A.6) is complicated by the enormous number of dimensions in the integrand, 10^{23} for a physical system, and the ability of the Boltzmann weight to vary over many orders of magnitude depending on the temperature

and potential energy function. A simple numerical integration of Eq. (A.6) is not feasible because of the enormous inefficiency of sampling the integrand at evenly spaced points[1] many of whose weighted contributions to the integral are negligible. Nicholas Metropolis and co-workers (1953) produced an algorithm that effectively removes these difficulties and which forms the basis of almost all Monte Carlo simulation techniques in use today.

The Metropolis algorithm replaces simple random sampling of the integrand in Eq. (A.6) by importance sampling in which configurations with internal energy U are generated with relative probability $\exp(-\beta U)$. This reduces the wasteful generation of configurations that do not contribute to the integral because of their low statistical weight. The algorithm then replaces an average of the form Eq. (A.6) by a sum over a finite number of configurations

$$\langle X \rangle \approx \frac{1}{M} \sum_{i=1}^{M} X_i , \qquad \text{(A.7)}$$

where X_i is the value of the observable in the ith configuration. The replacement of the integral by a sum obviously limits the accuracy of the averages, but the accuracy can be improved by making the number of configurations M large enough. A standard implementation of the Metropolis algorithm is as follows.

Consider N particles placed at arbitrary positions in a box with the number of particles, box volume and temperature held constant. Configurations for use in the averaging procedure, Eq. (A.7), can be generated by the following sequence of steps:

1. Select a particle from the N available.

2. Generate small, random displacements $\Delta x, \Delta y, \Delta z$ in its position coordinates, each uniformly distributed on the interval $(-\Delta/2, +\Delta/2)$, with Δ a parameter.

---

[1]It does not improve matters to select the points randomly.

3. Calculate the change in potential energy ΔU on displacing the particle.

4. If $\Delta U < 0$ accept the new configuration.

5. If $\Delta U > 0$ generate a random number ω uniformly distributed on the interval $(0,1)$ and accept the new configuration if $\omega < \exp(-\beta \Delta U)$, otherwise retain the old configuration.

6. Repeat steps 1-5 for all particles in the system (a single iteration of steps 1 to 5 for all particles in a system we call a *sweep*).

This procedure is repeated until a sufficient number of sample configurations have been generated to estimate averages using Eq. (A.7) to the required statistical accuracy. A proof that this method produces configurations that are asymptotically weighted according to the equilibrium probabilities of the canonical ensemble is given by Zannoni (Ch. 9, Luckhurst and Gray, 1979).

The maximum size of the particle steps, Δ, is not determined by the algorithm so its size may be chosen to optimise convergence of the simulation to equilibrium. Commonly, Δ is chosen so that approximately one half of the attempted moves are accepted. Too high an acceptance rate means the system is moving too slowly through its phase space, while too low an acceptance rate is inefficient in the use of computing time.

The above algorithm generates averages for the NVT ensemble. We have mainly performed simulations with the pressure, not the volume, held constant. This is the NPT ensemble, also known as the isobaric-isothermal ensemble. In the NPT ensemble the Helmholtz free energy Eq. (A.3) is replaced by the Gibbs free energy via a Legendre transformation

$$G(N,P,T) = A(N,V,T) + pV . \qquad \text{(A.8)}$$

The partition function in the NPT ensemble is

$$Z_P = \exp(-\beta G) = \frac{1}{N!\lambda^{3N}} Q_p, \qquad \text{(A.9)}$$

$$Q_p = \int_0^\infty dV \exp(-\beta pV) Q_V = \int_0^\infty dV\, d^{3N}q \exp\left(-\beta\left[\sum_{i\neq j} U(r_{ij}) + pV\right]\right), \qquad \text{(A.10)}$$

where we have written Q_V for the configuration integral defined in Eq. (A.5). This procedure is described by Wood (1968) and Hansen and McDonald (1986). The algorithm given by steps 1-6 now has an extra sequence added to sample the configuration space of the variable box volume.

7. Generate small random changes in the box side lengths, $\Delta L_x, \Delta L_y, \Delta L_z$ uniformly distributed on the interval $(-\Xi/2, \Xi/2)$, with Ξ a parameter, and scale the particle coordinates by the factor $(1+\Delta L_x/L_x)$, for the x coordinate and similarly for the y and z coordinates.

8. Calculate the change in internal energy ΔU as a result of the rescaling, and form the function: $\Delta U' = \Delta U + p\Delta V - Nk_B T \ln\left(\frac{V+\Delta V}{V}\right)$, where ΔV is the change in computational box volume $V = L_x L_y L_z$.

9. If $\Delta U' < 0$ accept the new configuration.

10. If $\Delta U' > 0$ generate a random number ω uniformly distributed on the interval $(0,1)$ and accept the new configuration if $\omega < \exp(-\beta\Delta U')$, otherwise retain the old configuration.

Note that the pseudo-Boltzmann weight for the box rescaling includes terms resulting from the internal energy change, the volume change and the ideal-gas entropy of the

particles. The box side length parameter Ξ is commonly chosen to keep the acceptance rate for box rescaling close to one half.

In most simulations, periodic boundary conditions are used to reduce the effects of the edges of the simulation box, and allow a finite system to mimic an infinite system. If a particle moves across the boundary of the simulation box, it is brought back in at the opposite edge. The distance between two particles, used in calculating the internal energy of the system, is taken to be the shortest distance between one particle and all of the periodically repeated images of its neighbour.

A.2 Autocorrelation function analysis

A typical Monte Carlo simulation starts with an initial configuration of a system in which the particles are randomly or sequentially placed in the simulation box, and the Metropolis algorithm generates configurations for use in calculating ensemble averages via Eq. (A.7). There are several sources of inaccuracy in this procedure that can be reduced to obtain results to a specified accuracy. The initial configuration may be far from equilibrium, and so skew the ensemble averages. Further, successive configurations produced by the Metropolis algorithm are highly correlated as they differ only in the position of a single particle. The system must be allowed to evolve for many sweeps between sample configurations to ensure that positional (and orientational) correlations between the particles have decayed away, and that the sample configurations are distributed according to the equilibrium probabilities of the ensemble. Finally, the rate at which the system moves through its phase space may be too slow to provide a representative average over the accessible region.

The correlation between the values of an observable in successive configurations in an MC simulation is measured by the observable's autocorrelation function. This quantity can be determined from a simulation, and a correlation time estimated. The correlation

time is a measure of the number of sweeps that must separate sample configurations to ensure their statistical independence. It also allows us to estimate how many configurations to discard at the start of a simulation to reduce any dependence on the initial state. We now describe how to calculate the autocorrelation function for an observable.

Given a set of N values $\{x_i\}$ of an observable X obtained from successive samples in an MC simulation, the autocorrelation function of X is defined as

$$C_2(n) = \frac{\sum_{i=1}^{N-n}(x_i - \langle x\rangle)(x_{i+n} - \langle x\rangle)}{(N-n)\sigma^2}, \tag{A.11}$$

where the ensemble average and standard deviation of the set $\{x_i\}$ are defined by

$$\langle x\rangle = \frac{1}{N}\sum_{i=1}^{N} x_i, \tag{A.12}$$

$$\sigma^2 = \frac{1}{N}\sum_{i=1}^{N} x_i^2 - \left(\frac{1}{N}\sum_{i=1}^{N} x_i\right)^2. \tag{A.13}$$

The autocorrelation function is restricted to the range $(0,1)$ with this definition, and complete correlation gives $C_2(n) = 1$, while complete randomness gives $C_2(n) = 0$. If we approximate the autocorrelation function at small times as a single exponential, that is,

$$C_2(n) = C_0 e^{-n/\tau}, \tag{A.14}$$

then the correlation time τ gives a measure of the number of configurations to be discarded between samples to ensure statistically independent values of the observable X. Usually, we perform preliminary simulations to estimate the relevant correlation times in a system, and then arrange for subsequent simulations to produce sample configurations separated by the appropriate numbers of sweeps. The assumption that the correlation time is a simple exponential breaks down if there are many different relaxation mechanisms in

the system. However, we are usually interested only in some features of a system, whose relaxation may be governed by one dominating mechanism. In this case we can measure the autocorrelation function for the observables of interest and neglect the others. The rate at which a system moves through its phase space during an MC simulation is controlled by the particle move parameter Δ, and box side rescaling parameter Ξ. The values of these parameters are chosen from experience to expedite the simulations.

The final point to be made about the Metropolis algorithm is the question of how many configurations to keep in calculating ensemble averages. We cannot generate an unlimited number of samples because of finite computer time and memory. We use a fixed number of configurations for most results and occasionally perform a simulation with a much larger number of configurations. If the averages do not change significantly on extending a simulation, we can be confident that keeping more configurations would not greatly improve the accuracy of the results. Additionally, we repeat several simulations and check that average values of observables are reproduced with the accuracy expected from a single simulation.

APPENDIX B

SIMULATION DETAILS AND ERROR ANALYSIS

In this appendix we describe the details of the simulation techniques used to investigate the three model systems of interest in the thesis. Section B.1 describes the simulations of discotic liquid crystal molecules presented in Chapter 2, Section B.2 describes the polymerised membrane simulations of Chapter 4, and Section B.3 gives the details of the fluid membrane simulations presented in Chapter 5. We also present here the relevant error analyses for the simulations.

B.1 Liquid crystal simulation details

B.1.1 Isotropic-nematic transition in 3D

We consider a system of N hard disks confined to a cubical box subject to periodic boundary conditions. The disks are initially positioned randomly throughout the box. Each MC step consists of an attempt to make small, random changes to the position and orientation of each disk. For the position coordinates this displacement is of the form $2.DS.(\frac{1}{2}-\omega)$, where DS is the maximum allowed step size, and ω is a random number uniformly distributed on the interval (0,1). The angular moves are treated slightly differently. The polar and azimuthal angles (θ,ϕ) are sampled so that the normal vector to an isolated disk uniformly samples the surface of a unit sphere. The probability of the orientation defined by the spherical polar coordinates (θ,ϕ) is thus

$$p(\theta,\phi)\,d\theta d\phi = \frac{1}{4\pi} sin\theta \; d\theta \; d\phi. \qquad \text{(B.1)}$$

The angles are restricted to their usual ranges, $0 \le \theta \le \pi, 0 \le \phi \le 2\pi$. A random change, $\Delta\phi$, is made in the azimuthal angle, but it is the cosine of the polar angle that is altered,

$\Delta(\cos\theta)$. The maximum step size for the translational and azimuthal angle moves is DS and $\pi\times DS$ respectively, while that for the cosine of the polar angle is $0.1\times DS$. Values for DS are given later. The new position and orientation are accepted if the disk does not intersect another disk. The Boltzmann factor associated with the disk moves is zero or one given the hard-core repulsion of the disks.

After an attempt has been made to move each of the disks, a random change is made in the length of the box sides. The algorithm used to generate the new box sides is

$$L' = L + 2.DL.\left(\tfrac{1}{2} - \omega\right) \qquad \text{(B.2)}$$

where DL is the maximum step size for the box rescaling, and ω is a random number uniformly distributed on the interval (0,1). The same rescaling factor is applied to each box side. The new box size is accepted according to the pseudo-Boltzmann factor

$$w = \exp\left(-\beta p \Delta V + N \ln(V'/V)\right) \qquad \text{(B.3)}$$

where $\Delta V = V' - V$ is the change in volume of the box and p the applied pressure. The move is accepted if the weight w is greater than one, or less than one but greater than a random number uniformly distributed on the interval (0,1). The move is rejected if it causes any disk to intersect another. Note that the temperature only appears in combination with the pressure as $\beta p R^3$. A sweep across the system consists of an attempt to move and rotate each disk by random amounts, followed by an attempt to rescale the box volume.

The systems were evolved for 1,000,000 sweeps to equilibrate, and then sample configurations were collected every 50,000 sweeps. The ensemble averages were usually constructed from 50 configurations, although some simulations used 100 -200 configurations. At the time these simulations were performed this was considered reasonable (Boal and Blair, 1990). The disk move step size was in the range 0.02-0.1, and

the volume rescaling step size was in the range 0.001-0.01. This resulted in acceptance rates of 40-90% for disk moves and 15-50% for volume rescalings.

Table B.1 shows the single-particle, polar angle correlation times for representative simulations of disks of thickness $T/R = 0.02, 0.2, 0.4, 1.0$. Except near the I-N transition at $\beta pR^3 \approx 3.5$, the correlations are of the order of the 50,000 sweep standard we used for all applied pressures. We have used the single particle correlation time, instead of the collective correlation time, because it better represents the orientational behaviour of a disk. The orientational correlation time is small for pressures $\beta pR^3 < 3$, but grows rapidly at higher pressures. This reflects the fact that the disks are closely packed at pressures $\beta pR^3 > 3$ and unable to rotate freely, hence their orientations are expected to be

Pressure	Correlation time for $T/R = 0.02$ (sweeps)	Correlation time for $T/R = 0.2$ (sweeps)	Correlation time for $T/R = 0.4$ (sweeps)	Correlation time for $T/R = 1.0$ (sweeps)
0.1	300	2000	300	250
1	4000	10,000	3000	10,000
2	100,000	NA	NA	NA
3	400,000	31,000	40,000	NA
4	25,000	464,000	80,000	80,000
5	NA	52,000	NA	NA
6	NA	155,000	15,000	NA
8	NA	NA	NA	15,000

Table B.1 Single-particle polar angle autocorrelation times for 64 and 100 disks in three dimensions, subject to a hydrostatic pressure βpR^3. The results for $T/R = 0.2$ are from 64 disk simulations, the other results are taken from 100 disk simulations. (NA=Not available)

constrained. As a result of the limited number of configurations used for the averages, the accuracy of the simulations is limited to 10% away from the I-N transition, and approximately 15% near the transition. We show in Table B.2 the orientational order parameter, defined in Section 2.2, and its standard error for systems of 64 and 100 disks. In the isotropic phase, the order parameter is consistent with zero to within statistical

error, while the fluctuations in the order parameter in the nematic phase are less than 1%. Near the I-N transition the error in the order parameter rises to about 15%. Towards the end of this work, quantitatively similar results on the I-N phase transition were published by Veerman and Frenkel (1992) and it was not felt worthwhile to continue the simulations to greater accuracy.

Pressure	$\langle -2\lambda_0 \rangle$ for 64 disks	$\langle -2\lambda_0 \rangle$ for 100 disks
0.1	0.003±0.006	NA
1	0.02±0.008	0.02±0.006
2	0.06±0.01	0.04±0.008
3	0.15±0.02	0.18±0.02
4	0.77±0.01	0.78±0.007
5	0.91±0.004	0.91±0.003
6	0.96±0.002	NA

Table B.2 Orientational order parameter for 64 and 100 disks in three dimensions subject to a hydrostatic pressure βpR^3. The data displayed are constructed from 100-200 configurations separated by 20-50,000 sweeps. (NA=Not available)

B.1.2 Isotropic-nematic transition at a 2D interface

The algorithm used for the simulation of platelets confined to a two-dimensional, planar interface is similar to that used for the three-dimensional simulations. The N platelets are placed randomly at the interface, subject to the constraint that part of their body intersects the interface. The interfacial plane is continued using periodic boundary conditions. An MC step consists of an attempt to move and rotate each platelet independently using the procedure described in Section B.1. A move is rejected if it causes a platelet to intersect another platelet or if it removes the platelet from intersecting the interface.

An attempt to rescale the interfacial area is made once every 10 sweeps. The box sides are rescaled independently in the x and y directions. The z dimension of the box is not rescaled. The algorithm used to generate the new box sides is

$$\begin{aligned} L_x' &= L_x + 2.DL.\left(\tfrac{1}{2} - \omega_1\right), \\ L_y' &= L_y + 2.DL.\left(\tfrac{1}{2} - \omega_2\right), \end{aligned} \tag{B.4}$$

where DL is the area rescaling step size, and ω_1, ω_2 are random numbers uniformly distributed on the interval $(0,1)$. The new box size is accepted according to the pseudo-Boltzmann factor $w = \exp\left(-\beta p \Delta A + N \ln\left(A'/A\right)\right)$, where $\Delta A = A' - A = L_x' L_y' - L_x L_y$ is the change in area of the box and p the applied pressure. Because there is an energy scale in these simulations, the factor of β is relevant. Note that the energy of the platelets does not change when the interfacial area is rescaled, because the area of contact of each platelet with the interface is unchanged. A sweep now consists of an attempt to move and rotate each platelet, followed by an attempt to rescale the interfacial area.

The systems were evolved for 1,000,000 sweeps to equilibrate and sample configurations were taken every 50,000 sweeps. The acceptance rates for particle moves and box rescaling were around 70% and 50% respectively. The correlation times were less than the standard 50,000 sweeps except at temperatures $\left(\beta g_f R^2\right)^{-1} < 1$, where they rose to around 150,000 sweeps. The ensemble averages were constructed from 100 configurations. We estimate the accuracy of the results to be approximately 20%.

B.2 Polymerised membrane simulation details

This section describes the details of the simulations of a network of Hooke's law springs in two dimensions. The initial configuration of the Hooke's law network is taken as a rectangular patch of N vertices cut from a regular, hexagonal lattice with all bond lengths equal to the unstretched spring length s_h. An exception is made for the network at infinite

temperature, for which an initial bond length of $(\beta k)^{-1/2}$ is used. A sweep across the network consists of an attempt to move each vertex by random amounts in the x and y directions, followed by an attempt to rescale the rectangular shape of the network independently in the x and y directions. The algorithms for such moves are similar to those already described. The bonds in the self-avoiding network are prevented from crossing one another by forbidding the cross-product of bond vectors from changing sign during a vertex move. This constraint is not present for the phantom network.

All networks are allowed to relax for 100,000 sweeps to equilibrate, and then sample configurations are extracted every 5,000-10,000 sweeps. The ensemble averages are usually constructed from 1000 configurations. The step sizes for the vertex moves and box rescaling are usually 0.5 and 0.05 respectively, resulting in acceptance rates of approximately 50-70% for vertex moves and 40-50% for box rescaling.

B.2.1 Step size dependence of ensemble averages

The number of configurations needed for a system to reach equilibrium in an MC simulation depends on the step size used for particle moves. The ensemble average of the observables, however, is independent of the magnitude of the step size. In Table B.3 we show the effect of changing the step size on the ensemble averages for the phantom Hooke's law network. We have set the box rescaling step size to 0.1 times the vertex move step size for these simulations. We only show the results for the phantom network because its errors are greater than or equal to those of the self-avoiding network.

$-p/k$	Step size	Asymmetry	$\langle A \rangle / N s_h^2$	K/k	μ/k
1.0	0.1	1.155±0.001	4.340±0.007	0.32±0.02	1.24±0.18
1.0	0.3	1.155±0.001	4.355±0.007	0.32±0.02	1.26±0.10
1.0	0.5	1.155±0.001	4.370±0.007	0.36±0.06	1.42±0.12
1.0	0.7	1.154±0.001	4.380±0.007	0.37±0.05	1.43±0.22
0.75	0.1	1.155±0.002	1.475±0.008	0.09±0.01	0.57±0.08
0.75	0.3	1.160±0.002	1.660±0.006	0.17±0.02	0.86±0.07
0.75	0.5	1.155±0.002	1.765±0.006	0.20±0.01	0.98±0.13
0.75	0.7	1.155±0.002	1.810±0.006	0.22±0.02	1.06±0.26

Table B.3 Variation of representative observables with the vertex move step size for a phantom Hooke's law network at a temperature $k_B T / k s_h^2 = 1$, for two pressures p/k. The results shown are obtained from simulations of 256 vertices using 1000 configurations, separated by 1000 sweeps, to form the averages. (See text for a definition of the errors shown.)

Table B.3 is compiled from simulations of a phantom network with 256 vertices at a temperature $k_B T / k s_h^2 = 1$. The errors quoted in the table are the standard error of the mean value (the standard error is $1/\sqrt{N}$ times the ensemble standard deviation, where N is the number of independent configurations used to construct the averages). The statistical error in the network observables is approximately 1%, and the sample configurations are effectively indpendent as will be shown in the next section. We conclude that the results of Chapter 4 are not unduly affected by the step size used in the simulations.

B.2.2 Autocorrelation function analysis

We have measured the autocorrelation functions, as defined in Section A.2, for the simulation box side lengths and area. These are the observables used to calculate the elastic constants using the results of Chapter 3.

The sequence of values of an uncorrelated observable plotted against simulation time shows random fluctuations about a constant mean value.The values of the area and box side lengths generated in each simulation are plotted and inspected by eye to see if there is any secular trend. The best-fit straight line through the data is compared with the long-time average of the same data. The two curves coincide for an observable in an equilibrated system. This method showed that the observables were uncorrelated in almost all simulations, except near the collapse transition for the phantom networks.

A typical measure of the correlation time for a polymer system is given by the Rouse time, $\tau = N/DS^2$, where N is the number of vertices and DS is the vertex move step size. We have used 5000-10000 sweeps between sample configurations which is approximately 3-6 Rouse times for the 400 site network, and even greater for smaller networks. The

$-p/k$	Step size	τ_x (sweeps)	τ_y (sweeps)	τ_A (sweeps)	Vertex move	Area rescaling
1.0	0.1	330	355	365	0.94	0.91
1.0	0.3	380	335	355	0.81	0.72
1.0	0.5	31	33	32	0.68	0.54
1.0	0.7	24	24	24	0.57	0.39
0.75	0.1	4400	4900	4600	0.94	0.88
0.75	0.3	550	560	530	0.83	0.63
0.75	0.5	170	180	210	0.72	0.42
0.75	0.7	82	88	86	0.61	0.28

Table B.4 Autocorrelation times for network side lengths τ_x, τ_y and area τ_A, and vertex move and area rescaling acceptance rates for phantom Hooke's law networks as a function of vertex move step size. (See Table B.3 for description of simulations used to compile the data.)

correlation time analysis described in Section A.2 shows that the configurations used to generate the results of Chapter 4 are uncorrelated. The measured correlation times for the runs used in the step size analysis discussed above are shown in Table B.4.

Network type	$-p/k$	No of vertices	No of points	$\langle A\rangle/Ns_h^2$	K/k	μ/k
Phantom	1.5	256	1000	48.02±0.04	0.12±0.01	1.60±0.05
Phantom	1.5	400	1000	47.94±0.03	0.12±0.01	1.67±0.24
SA	1.4	256	1000	23.28±0.02	0.17±0.01	1.54±0.22
Phantom	1.4	256	5000	23.24±0.01	0.18±0.01	1.52±0.05
SA	1.0	256	984	4.435±0.007	0.39±0.02	1.39±0.21
Phantom	1.0	256	1000	4.380±0.007	0.37±0.04	1.39±0.18
Phantom	1.0	400	1000	4.365±0.006	0.34±0.04	1.40±0.16
SA	0.75	256	1000	2.480±0.004	0.53±0.07	1.12±0.09
Phantom	0.75	256	1000	1.766±0.006	0.20±0.01	0.98±0.13
Phantom	0.75	256	5000	1.765±0.003	0.20±0.01	0.97±0.03
Phantom	0.75	256	5000	1.770±0.003	0.21±0.01	0.92±0.06
Phantom	0.75	256	5000	1.820±0.003	0.20±0.01	0.83±0.04
Phantom	0.65	400	1000	0.710±0.005	0.06±0.003	0.47±0.03
Phantom	0.65	400	1000	0.700±0.006	0.04±0.005	0.24±0.05
Phantom	0.65	400	1800	0.803±0.004	0.08±0.004	0.58±0.09
Phantom	0.65	900	3530	0.756±0.002	0.07±0.003	0.61±0.05
Phantom	0.64	400	5000	0.613±0.002	0.06±0.003	0.47±0.02
SA[2]	0.5	144	500	1.700±0.006	0.72	1.06
SA	0.5	256	417	1.710±0.004	0.85	1.03
SA	0.5	400	274	1.710±0.004	0.88	1.01

Table B.5 Statistical error in the area per vertex $\langle A\rangle/Ns_h^2$, and elastic moduli for self-avoiding (SA) and phantom networks at a temperature $k_BT/ks_h^2 = 1$, and various pressures p/k, for several system sizes showing the reproducibility of results in independent simulations

Table B.4 shows that the correlation times for the observables used to construct the elastic constants are negligible for pressures less than $p/k = -1$. Near the collapse transition, $p/k \approx -0.65$ at a temperature $k_BT/ks_h^2 = 1$, only simulations using the smallest step size 0.1 show a significant rise in the correlation times. The acceptance rates for vertex moves and box rescaling are around 70% and 40% respectively for the step size of 0.5 used in almost all simulations. As a further test of the accuracy of the results, Table B.5 shows the ensemble averages for networks at several pressures calculated from 1000

[2]The errors in the elastic constants for these three SA simulations are not available.

to 5000 configurations. There is no significant change in the results using the larger number of configurations to form the averages.

Most production runs used 256 vertices for phantom networks and 144 for self-avoiding networks. For pressures close to the collapse transition, $p/k > -0.75$, the phantom networks have 400 and 900 vertices. There is a negligible difference between the observables obtained from the phantom and self-avoiding networks at pressures $p/k < -1$. At pressures $p/k > -1$ the values of observables from independent simulations of the phantom network show some variation. The shear modulus shows the largest deviation, but even this is negligible for pressures $p/k < -0.75$.

The results in Table B.5 show that the statistical error in the area per vertex of the self-avoiding network is less than 1% for all pressures. The elastic constants are accurate to 10%. For the phantom network, the error in the area per vertex is less than 1% for pressures $p/k < -0.75$, but near the collapse transition the area per vertex approaches zero and its error increases to 25%. The elastic constants near the collapse transition are close to zero and difficult to measure accurately. The systematic errors due to correlations between successive configurations may be as high as a factor of two between independent simulations. We conclude that the errors in the data presented in Chapter 4 are less than the symbol size used in the figures, except for the elastic constants of the phantom network close to the collapse transition.

B.2.3 System size dependence of ensemble averages

Most of the results presented in Chapter 4 were for networks containing 144 or 256 vertices. We have also investigated phantom networks with 400 and 900 vertices to see if the network properties are affected by its finite size. The results of simulations using the larger numbers of vertices are shown in Table B.5. We find no appreciable dependence of the network's elastic properties on system size.

B.3 Fluid membrane simulation details

The fluid membrane described in Chapter 5 is represented by a two-dimensional, self-avoiding network of vertices connected by bonds, or tethers, that can migrate through the network. The simulation technique is similar to that for the polymerised network described in Section B.2 with two additions: the vertices are allowed to change their connectivity; and a hole is allowed to develop in the network. The initial configuration of the network is a rectangular patch of N vertices excised from a regular hexagonal lattice. The energy of a tether is given by Eq. (5.10). The initial bond lengths are all equal to $0.9s_0$. A sweep across the network consists of an attempt to move each vertex by random amounts in the x and y directions, followed by an attempt to rescale the network area, and two additional algorithms to simulate the fluidity of the network and the growth of a hole.

All networks are allowed to relax for 1,000,000 sweeps before sample configurations are collected. Most results are derived from ensemble averages of 400-1000 configurations separated by a variable number of sweeps that depends on the simulation parameters (line tension and pressure). We present the correlation time analysis for the relevant observables after describing the network fluidity and hole growth algorithms.

B.3.1 Bond fluidity algorithm

An algorithm for simulating a fluid network was introduced by Baumgartner and Ho (1990). This algorithm allows bonds to migrate between neighbouring pairs of vertices, changing the connectivity of the network. As illustrated in Fig. B.1, a bond initially connected to two end vertices, 1 and 2, may be disconnected and reconnected to the two "adjacent" vertices, 3 and 4.

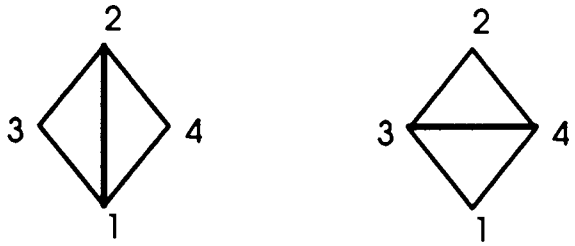

Figure B.1 Bond move showing the reconnection of a bond from its two end vertices 1, 2 to its "adjacent" vertices 3, 4.

The bond move must satisfy the following conditions. The new bond must be less than the maximum tether length s_0, and the coordination number of the four vertices involved must not drop below three or exceed nine. The lower limit is set to maintain the triangulation of the network, while the upper limit is for computational convenience. A final test is applied to the bond move to prevent the network intersecting itself. A typical move that is forbidden by this test is shown below in Fig. B.2.

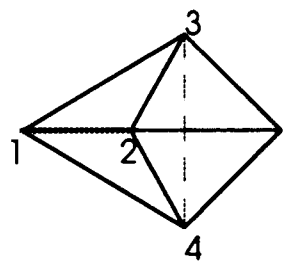

Figure B.2 Example of a forbidden bond move from end vertices 1, 2 to "adjacent" vertices 3, 4: the dashed line does not represent an allowed bond configuration as two bonds are intersecting.

In this attempted move, the bond represented by the solid line connecting vertices 1, 2 is allowed to move to its adjacent vertices 3, 4 by the previous tests of length and coordination number, so an extra test is used to prevent the consequent bond crossing. This test requires that the area of the two triangles adjacent to the bond that is being moved be the same before and after the move.

The fluidity algorithm allows a bond to move through the network by changing its connectivity step by step. Because there is no energy scale for the bonds (as long as they are less than the maximum length) there is no Boltzmann weight for a bond move. An attempt is made to move each internal bond once per sweep. An internal bond is one that satisfies the conditions specified above of having two end vertices and two "adjacent" vertices.

B.3.2 Simulation of a hole in a fluid network

When a hole is present in the network we have to distinguish between internal vertices in the bulk of the network, and external vertices on the perimeter of the hole. External vertices have only one adjacent vertex, and are forbidden from changing their connectivity via the bond fluidity algorithm just described. In addition, the hole is enabled to grow and shrink by attempts to cut and add bonds on its perimeter. After several attempted algorithms for hole growth were found to be biased in some way, the final algorithm used produces hole growth statistics that appear to satisfy detailed balance. The hole perimeter is prevented from intersecting itself by means of a new self-avoidance routine. We now discuss these algorithms in turn.

A hole is introduced into the network by removing one bond from the initial configuration. This creates a hole with a perimeter of four external vertices (and, of course, four external bonds). All other vertices are labelled internal. A sweep across the network includes N attempts to cut or add a bond around the hole[3]. Each attempt is randomly chosen to be a cut or add move. The number of attempts is made equal to the system size to ensure an attempt rate comparable to the vertex move algorithm.

---

[3]As usual, N is the number of vertices in the network and is constant, although the number of bonds varies as the hole grows and shrinks.

The hole growth algorithm is as follows. A bond is randomly selected on the hole perimeter and an attempt is made either to remove it, or to add a bond across one of its end vertices. A bond cut move is forbidden if either of the following two conditions are met:

- The vertex adjacent to the bond to be removed is already on the hole perimeter. This prevents the perimeter passing through the same vertex twice, which would cause it to be not simply connected.
- The coordination of the vertices at either end of the bond falls below 3.

A Boltzmann factor is used to weight the bond cut. The energy change comes only from the line tension around the hole, and is given by $\Delta U = \lambda \Delta L$, where λ is the line tension (energy per unit length of the perimeter) and ΔL is the change in perimeter length due to the bond cut. For a positive line tension, the energy of the system is always increased by removing a bond, and the move is accepted with probability $\exp(-\beta \Delta U)$. If the bond cut is rejected, another vertex is randomly selected and the add/cut process repeated. If it is accepted, the two bonds revealed by the cut bond are labelled external and become candidates for future bond cut or add attempts.

The bond add routine attempts to make the hole shrink by adding a bond between a pair of next-nearest neighbour vertices on the perimeter. In a similar manner to the bond cut move, an external vertex is randomly chosen and one of its next-nearest neighbours is also randomly selected. An attempt is made to add a bond between the two vertices subject to the following checks: the new bond length must be less than the maximum tether length, and the new bond must not intersect any other bond. A move that is prevented by this test is illustrated below in Fig. B.3.

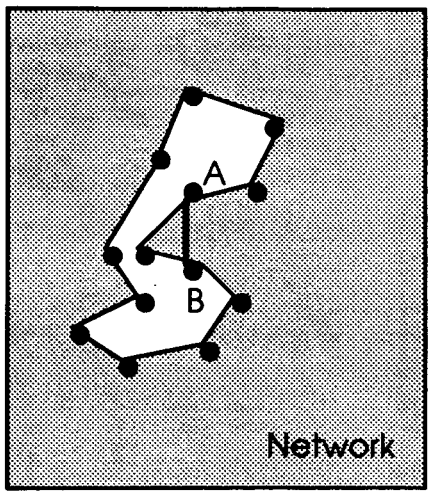

Figure B.3 An attempt to add a bond between vertices A and B fails because the new bond would intersect a bond already present in the network.

The bond to be added to the vertices labelled A, B in Fig. B.3 would intersect another bond and so the attempt is forbidden. The test used to prevent this move is shown below in Fig. B.4.

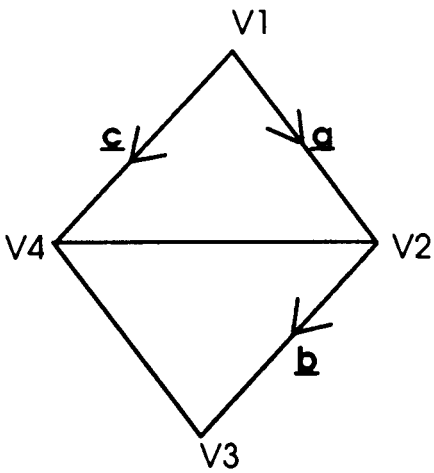

Figure B.4 Definition of bond vectors used in checking a bond add move. Vertices V1, V2, V3, are on the hole perimeter, vertex V4 is in the interior of the network.

The external vertices V1, V2, V3 lie on the hole perimeter, the vertex V4 is that internal vertex closest to V1. The vectors **a**, **b**, **c** are defined in Fig. B.4. An attempt to add a bond

between vertices V1 and V3 is accepted if $sign(\underline{a}.\underline{b}) \neq sign(\underline{a}.\underline{c})$. This test ensures that the hole perimeter is concave between the two vertices which are to be connected by the new bond. The Boltzmann weight is always unity for the bond add move because it is always energetically favourable to reduce the hole perimeter given a positive line tension.

The problem of keeping the perimeter of the hole from intersecting itself is a highly non-local one. Protuberances of the bulk network that project into the hole, such as those seen in Fig. 5.4, occur frequently when the hole is large because they are entropically favoured. After several attempts at finding an elegant, geometrical method of preventing the hole perimeter from intersecting itself, we finally used a lookup table containing the nearest neighbours of each vertex, and used it to check vertex moves for both internal and external vertices.

The lookup table contains a list of vertices within a fixed distance of each vertex. When an attempt is made to move a vertex, the code checks with the vertices on this list to ensure that its new position does not cause two vertices to intersect, or two bonds to cross. Two vertices are prevented from intersecting by requiring that the distance between their centres be greater than the hard-core vertex diameter a, and vertices are prevented from crossing neighbouring bonds by keeping the maximum tether length less than $s_0 < \sqrt{3}a$. We use the value $s_0 = 1.688a$, because the finite step size in the simulations could allow a vertex to pass through a bond if $s_0 = \sqrt{3}a$ exactly. The lookup table is updated every 10 sweeps, and this was found to be frequent enough to prevent any intersections occurring.

The order of execution of the various algorithms was found to be unexpectedly significant in the fluid network simulations. Initially, a fixed number of bond cut attempts were followed by a fixed number of bond add attempts. However, unless the bond add/cut moves were separated by a randomising process, such as the vertex moves, the hole only

oscillated about its initial state. The algorithms were ordered so as to remove these spurious oscillations. The order in which the various algorithms are executed is:

- Attempt to move each of the N vertices.
- Attempt to add/cut N bonds around the hole.
- Attempt to reconnect each internal bond to its "adjacent" vertices.
- Attempt to rescale the network area.

B.3.3 Autocorrelation function analysis

Similarly to the polymerised network, the sequences of values of the network area, hole inertia tensor eigenvalues and hole area generated in a simulation were inspected by eye to see if there was any secular trend. Most of the data sets showed no trend, but some had to be discarded because they had not reached equilibrium in the time allowed for the simulation. This suggests the presence of very long correlation times in the square-well network, which was confirmed when the autocorrelation functions of the observables were measured. Most simulations used configurations separated by 50,000 sweeps. We show the correlation times for some typical simulations at zero pressure in Table B.6 for a range of line tensions from $\beta\lambda a = 0.8$ to 1.5.

The correlation times for the network area and hole observables are within the standard 50,000 sweeps, except for line tensions near the critical value. The step size for vertex moves was between 0.15 and 0.25, and the area rescaling step size was set to 0.1 times the vertex move step size. The acceptance rate for vertex moves was in the range 30-60%, while that for area rescalings was in the range 20-60%. No significant variation in the network's properties with step size was found.

The correlation times for the networks under compression, shown in Table B.7, are much shorter than those for networks at zero pressure. We only show the data for positive pressure because the correlation times for negative pressure simulations are comparable. The correlation times for positive pressure simulations are always much less than the standard number of sweeps, and in most cases the correlation between configurations separated by 100 sweeps is essentially zero. We allow between 5000 and 50,000 sweeps between configurations for the positive pressure simulations. The largest correlation times

Line Tension	Step size	τ_1 (10^3 sweeps)	τ_2 (10^3 sweeps)	τ_3 (10^3 sweeps)	Vertex move	Box rescaling
1.4	0.2	5.6	5	5.6	0.41	0.29
1.25	0.20	43	47	46	0.41	0.28
1.2	0.2	120	121	132	0.43	0.34
1.0	0.2	95	55	74	0.48	0.50
1.0	0.2	110	150	120	0.48	0.49
0.8	0.15	120	100	90	0.49	0.53
1.5	0.15	5.6	6	5.7	0.51	0.25
1.5	0.25	2.5	2.6	2.6	0.32	0.13
1.3	0.25	49	44	48	0.33	0.13

Table B.6 Autocorrelation times for the hole eigenvalues τ_1, τ_2 and hole area τ_3 and acceptance rates for fluid networks at zero pressure, with $N = 196$ vertices (top of table), and $N = 400$ vertices (bottom of table), for various line tensions $\beta\lambda a$.

were found for pressures close to zero, showing that correlations in the square-well network under pressure decay more rapidly than the zero pressure networks. This result is also found for simulations of polymerised networks in Chapter 4: the Hookean spring networks have correlation times smaller by an order of magnitude than the equivalent square-well networks (unpublished data).

When the measured correlation time exceeds the allowed 50,000 sweeps, we use the estimated correlation time to reduce the number of configurations used in constructing the ensemble averages, thus creating a smaller, uncorrelated set of configurations from the original, correlated set. The standard error of the mean value correspondingly increases. Given a simulation with N configurations, in which τ is the measured correlation time (in sweeps), and ν is the number of sweeps between sample configurations in the original

Line Tension	βpa^2	No of points	τ_1 (10^3 sweeps)	τ_2 (10^3 sweeps)	τ_3 (10^3 sweeps)	Vertex move	Box rescaling
1.2	0.5	1000	1000	1000	1050	0.40	0.30
1.2	1	1000	270	220	220	0.38	0.29
1.2	2	1000	<200	<200	<200	0.35	0.22
1	1	1000	600	560	590	0.38	0.31
1	2	1000	<100	<100	<100	0.35	0.24
1	3	1000	<100	<100	<100	0.32	0.19
1	4	500	<200	<200	<200	0.52	0.33
0.8	1	1000	4200	5600	3800	0.41	0.32
0.8	2	388	870	940	950	0.22	0.14
0.8	3	644	<100	<100	<100	0.32	0.18
0.8	4	500	<500	<500	<500	0.29	0.14
0.8	6	1000	<100	<100	<100	0.23	0.10
0.8	8	500	<400	<400	<400	0.39	0.20

Table B.7 Autocorrelation times for hole eigenvalues τ_1, τ_2, and hole area τ_3, and acceptance rates for a fluid network with $N = 196$ vertices, subject to a line tension $\beta\lambda a$ and compressive pressure βpa^2. (<100 means that the correlation between two successive data points separated by 100 sweeps was negligible.)

simulation, the number of statistically independent configurations is approximately given by the formula

$$M = \frac{N}{\left(1+\frac{2\tau}{\nu}\right)}. \qquad \text{(B.5)}$$

Based on the measured correlation time, we recalculate the ensemble averages using the number of configurations defined by Eq. (B.5)[4]. This does not change the average values of observables significantly, but it does change the accuracy of the standard error defined by

$$S_N = \frac{\sigma_N}{\sqrt{N-1}} \tag{B.6}$$

where σ_N is the standard deviation of the set of sample configurations. When the data points are not truly uncorrelated we replace N in Eq. (B.6) by M determined from Eq. (B.5). We show in Table B.8 typical values of the network and hole areas for networks with 196 vertices, before and after the correction. It is seen that the result of this analysis is a moderate increase in the standard error of the ensemble averages for line tensions close to the transition. The errors change by less than a factor of 2 for networks in which the hole is small. Below the transition point, $\beta\lambda a = 1.25$, the errors increase by up to a

Line tension	N	M	Original $\langle A/a^2 \rangle$	Modified $\langle A/a^2 \rangle$	Original $\langle A_{hole}/a^2 \rangle$	Modified $\langle A_{hole}/a^2 \rangle$
1.4	200	167	290.1±0.3	290.2±0.5	4.4±0.4	4.6±0.5
1.25	715	179	300.0±0.5	300.0±0.9	12.5±0.7	11.9±1.3
1.2	321	107	332±3	331±4	58±4	58±6
1.0	400	69	575±5	569±13	375±5	369±13
0.8	400	67	690±6	679±15	505±6	493±15

Table B.8 Calculation of the standard error of ensemble averages using the original number of configurations N and the smaller number of data points M determined from Eq. (B.5) for a range of line tensions $\beta\lambda a$. The two observables are the total network area $\langle A/a^2 \rangle$ and the hole area $\langle A_{hole}/a^2 \rangle$, and the standard errors shown are calculated from Eq. (B.6).

[4]We use every N/M th point for constructing the averages instead of all N.

factor of 3. This partly reflects the large fluctuations in the hole size as the membrane disintegrates. The mean values of the observables are seen not to change very much as a result of this analysis.

As a further test of the accuracy of the results, we perform several simulations keeping 1000 configurations to calculate the ensemble averages. The results are shown in Table B.9 below. It is found that 400 configurations give an accuracy of better than 5% for most observables. The elastic constants are an exception. Because the compression and shear moduli are calculated from fluctuations in the box side lengths and area, their accuracy is intrinsically poorer than that of the quantities from which they are derived.

Line tension	System size	No of points	$\langle A \rangle / a^2$	$\beta K a^2$	$\beta \mu a^2$	$\langle A_{hole} \rangle / a^2$
1.3	196	711	293.3±0.4	2.6	0.004	9.7±0.6
1.3	196	1000	293.5±0.3	2.4	0.005	10.0±0.5
1.275	400	458	597.1±0.7	3.1	0.004	15.0±1.0
1.275	400	1000	599.2±0.6	1.4	0.003	17.6±0.9

Table B.9 Comparison of membrane area $\langle A/a^2 \rangle$, elastic constants $\beta K a^2$ and $\beta \mu a^2$ and hole area $\langle A_{hole}/a^2 \rangle$ obtained from simulations with approximately twice the usual number of configurations at two line tensions $\beta \lambda a$ for system sizes $N = 196, 400$ vertices.

We conclude that the statistical errors in the network area, average bond length and asymmetry are less than 5% for all values of the line tension. The compression modulus is accurate to 5% for line tensions greater than $\beta \lambda a > 1.3$. For line tensions $\beta \lambda a < 1.3$, the compression modulus is indistinguishable from zero to within statistical error. The shear modulus is always consistent with zero to within statistical error. The errors in the observables presented in Chapter 5 are usually less than the symbol size used in the figures, and we have omitted the error bars on the figures for clarity.

BIBLIOGRAPHY

Abidor, I. G., V. B. Arakelyan, L. V. Chernomordik, Y. A. Chizmadzhev, V. F. Pastushenko, M. R. Tarasevich. 1979. Electric breakdown of bilayer lipid membranes. I. The main experimental facts and their qualitative discussion. *Bioelectrochem. Bioenerg.* 6:37-52.

Alberts, B., D. Bray, J. Lewis, M. Raff, K. Roberts, J. D. Watson. 1989. Molecular Biology of the Cell. Garland Publishing, New York and London.

Bahadur, B. (Editor). 1991. Liquid crystals: applications and uses. Vols I-III. World Scientific, Singapore.

Barsky, S., M. Plischke, D. H. Boal. 1994. SFU report.

Baumgartner, A., J.-S. Ho. 1990. Crumpling of fluid vesicles. *Phys. Rev. A.* 41:5747-5750.

Binder, K. 1986. Monte Carlo Methods in Statistical Physics. Topics in Current Physics Vol. 7. Springer-Verlag, Berlin.

Binder, K. 1987. Applications of the Monte Carlo Method in Statistical Physics. Topics in Current Physics Vol. 36. Springer-Verlag, Berlin.

Bloom, M., E. Evans, O. G. Mouritsen. 1991. Physical properties of the fluid lipid-bilayer component of cell membranes: a perspective. *Q. Rev. Biophys.* 24:293-397.

Boal, D. H. 1991. Phases of attractive two-dimensional vesicles under pressure. *Phys. Rev. A.* 43:6771-6777.

Boal, D. H., M. Blair. 1991. Amphiphilic platelets at a liquid interface. *Phys. Rev. A.* 43:2840-2847.

Boal, D. H., M. Rao. 1992a. Scaling behaviour of fluid membranes in three dimensions. *Phys. Rev. A.* 45:R6947-6950.

Boal, D. H., M. Rao. 1992b. Topology changes in fluid membranes. *Phys. Rev. A.* 46:3037-3045.

Boal, D. H., U. Seifert, A. Zilker. 1992. Dual network model for red blood cell membranes. *Phys. Rev. Lett.* 69:3405-3408.

Boal, D. H., U. Seifert, J. C. Shillcock. 1993. Negative Poisson ratio in two-dimensional networks under tension. *Phys. Rev. E.* 48:4274-4283.

Boal, D. H. 1994. Computer simulation of a model network for the erythrocyte cytoskeleton. *Biophys. J.* 67:521-529.

Bretscher, M. S. 1973. Membrane structure: some general principles. *Science.* 181:622-629.

Brock, J. D., R. J. Birgeneau, D. Litster, A. Aharony. 1989. Liquids, Crystals and Liquid Crystals. *Physics Today.* July 1989. 52-59.

Caddock, B. D., K. E. Evans. 1989. Microporous materials with negative Poisson's ratios: I. Microstructure and mechanical properties. *J. Phys. D: Appl. Phys.* 22:1877-1882.

Camacho, C. J., M. E. Fisher, R. R. P. Singh. 1991. Semiflexible planar polymeric loops. *J. Chem. Phys.* 94:5693-5700.

Cardy, J. 1994. Mean area of self-avoiding loops. *Phys. Rev. Lett.* 72:1580-1583.

Chandrasekhar, S., B. K. Sadashiva, Ka, Suresh. 1977. Liquid crystals of disc-like molecules. *Pramana.* 9:471-480.

Chandrasekhar, S., G. S. Ranganath. 1990. Discotic liquid crystals. *Rep. Prog. Phys.* 53:57-84.

Coldwell, R. L., T. P. Henry, Chia-Wei Woo. 1974. Free energy of a system of hard spherocylinders serving as a model for liquid crystals. *Phys. Rev. A.* 10:897-902.

Cotter, M. A. 1977. Hard spherocylinders in an anisotropic mean field: a simple model for a nematic liquid crystal. *J. Chem. Phys.* 66:1098-1106.

de Gennes, P. G. 1979. Scaling concepts in polymer physics. Cornell University Press, Ithaca and London.

de Gennes, P. G., J. Prost. 1993. The physics of liquid crystals. Clarendon Press, Oxford.

Destrade, C., P. Foucher, H. Gasparoux, Nguyen Huu Tinh. 1984. Disc-like mesogen polymorphism. *Mol. Cryst. Liq. Cryst.* 106:121-146.

Deuticke, B., P. Lütkemeier, B. Poser. 1992. Tellurite-induced damage of erythrocyte membrane. Manifestations and mechanisms. *Biochim. et Biophys. Acta.* 1109:97-107.

Divigalpitiya, W. M. R., R. F. Frindt, S. R. Morrison. 1989. Inclusion systems of organic molecules in restacked single-layer molybdenum disulfide. *Science.* 246:369-371.

Duplantier, B. 1990. Exact fractal area of two-dimensional vesicles. *Phys. Rev. Lett.* 64:493.

Duro, M. C., J. A. Martín-Pereda, L. M. Sesé. 1988. Monte Carlo simulation on a system of hard cylinders at a very high packing fraction. *Phys. Rev. A.* 37:284-286.

Eppenga, R., D. Frenkel. 1984. Monte Carlo study of the isotropic and nematic phases of infinitely thin hard platelets. *Mol. Phys.* 52:1303-1334.

Ertel, A., A. G. Marangoni, J. Marsh, F. R. Hallett, J. M. Wood. 1993. Mechanical properties of vesicles. I. Coordinated analyses of osmotic swelling and lysis. *Biophys. J.* 64:426-434.

Evans, E. A. 1973. New membrane concept applied to the analysis of fluid shear- and micropipette-deformed red blood cells. *Biophys. J.* 13:941-954.

Evans, E., D. Needham. 1987. Physical properties of surfactant bilayer membranes: thermal transitions, elasticity, rigidity, cohesion and colloidal interactions. *J. Phys. Chem.* 91:4219-4228.

Evans, E., W. Rawicz. 1990. Entropy-driven tension and bending elasticity in condensed-fluid membranes. *Phys. Rev. Lett.* 64:2094-2097.

Evans, E. A., R. Waugh, L. Melnik. 1976. Elastic area compressibility modulus of red cell membrane. *Biophys. J.* 16:585-595.

Evans, E. A., R. Waugh. 1977. Osmotic correction to elastic area compressibility measurements on red cell membrane. *Biophys. J.* 20:307-313.

Evans, K. E., M. A. Nkansah, I. J. Hutchinson, S. C. Rogers. 1991. Molecular network design. *Nature.* 353:124.

Evans, K. E. 1991. Auxetic polymers: a new range of materials. *Endeavour, New Series.* 15:170-174.

Evans, K. E., K. L. Alderson. 1992. The static and dynamic moduli of auxetic microporous polyethylene. *Journal of Materials Science Letters.* 11:1721-1724.

Evans, K. E., B. D. Caddock. 1989. Microporous materials with negative Poisson's ratios: II. mechanisms and interpretation. *J. Phys. D: Appl. Phys.* 22:1883-1887.

Exerowa, D., D. Kashchiev, D. Platikanov. 1992. Stability and permeability of amphiphile bilayers. *Advances in Colloid and Interface Science.* 40:201-256.

Feng, S., P. N. Sen. 1984. Percolation on elastic networks: New exponent and threshold. *Phys. Rev. Lett.* 52:216-219.

Feng, S., M. F. Thorpe, E. Garboczi. 1985. Effective-medium theory of percolation on central-force elastic networks. *Phys. Rev. B.* 31:276-280.

Fisher, M. E. 1989. Fractal and nonfractal shapes in two-dimensional vesicles. *Physica D.* 38:112-118.

Fraser, D. P., M. J. Zuckermann, O. G. Mouritsen. 1990. Simulation technique for hard-disk models in two dimensions. *Phys. Rev. A.* 42:3186-3195.

Freeman, S. A., M. A. Wang, J. C. Weaver. 1994. Theory of electroporation of planar bilayer membranes: predictions of the aqueous area, change in capacitance and pore-pore separation. *Biophys. J.* 67:42-56.

Frenkel, D., B. M. Mulder, J. P. McTague. 1984. Phase diagram of a system of hard ellipsoids. *Phys. Rev. Lett.* 52:287-290.

Frenkel, D., B. M. Mulder. 1985. The hard ellipsoid-of-revolution fluid. I. Monte Carlo simulations. *Mol. Phys.* 55:1171-1192.

Frenkel, D. 1987. Computer simulation of hard-core models for liquid crystals. *Mol. Phys.* 60:1-20.

Frenkel, D. 1988. Structure of hard-core models for liquid crystals. *J. Phys. Chem.* 92:3280-3284.

Frenkel, D., H. N. W. Lekkerkerker, A. Stroobants. 1988. Thermodynamic stability of a smectic phase in a system of hard rods. *Nature.* 332:822-823.

Frenkel, D. 1991. Simulation of sub-molecular and supra-molecular fluids. *Physica A.* 176:54-62.

Frölich, J. 1985. Applications of field theory to statistical mechanics. Vol. 216. L. Garido, editor. Springer, Berlin.

Fromherz, P. 1983. Lipid-vesicle structure: size control by edge-active agents. *Chem. Phys. Lett.* 94:259-266.

Fromherz, P., C. Röcker, D. Rüppel. 1986. From discoid micelles to spherical vesicles: the concept of edge activity. *Faraday Discussions of the Chemical Society.* 81:39-48.

Glaser, R. W., S. L. Leikin, L. V. Chernomordik, V. F. Pastushenko, A. I. Sokirko. 1988. Reversible electrical breakdown of lipid bilayers: formation and evolution of pores. *Biochim. Biophys. Acta.* 940:275-287.

Glaus, U. 1988. Monte Carlo study of self-avoiding surfaces. *J. Stat. Phys.* 50:1141-1166.

Gompper, G., D. M. Kroll. 1992. Shape of inflated vesicles. *Phys. Rev. A.* 46:7466-7473.

Gompper, G., D. M. Kroll. 1995. Phase diagram and scaling behaviour of fluid vesicles. *Phys. Rev. E.* 51:514-525.

Hallett, F. R., J. Marsh, B. G. Nickel, J. M. Wood. 1993. Mechanical properties of vesicles. II. A model for osmotic swelling and lysis. *Biophys. J.* 64:435-442.

Hansen, J. P., I. R. McDonald. 1986. Theory of simple liquids. Oxford Univ. Press, New York.

He, M., P. Siders. 1990. Monte Carlo calculation of orientationally anisotropic pair distributions and energy transfer in a model monolayer. *J. Phys. Chem.* 94:7280-7288.

Helfrich, W. 1973. Elastic properties of lipid bilayers: Theory and possible experiments. *Z. Naturforsch.* 28:693-703.

Helm, C. A., J. N. Israelachvili, P. M. McGuiggan. 1992. Role of hydrophobic forces in bilayer adhesion and fusion. *Biochemistry.* 31:1794-1805.

Hwa, T., E. Kokufuta, T. Tanaka. 1991. Conformation of graphite oxide membranes in solution. *Phys. Rev. A.* 44:R2235-R2238.

Israelachvili, J. N. 1992. Intermolecular and surface forces. Academic Press, London.

Jansen, M., A. Blume. 1995. A comparative study of diffusive and osmotic water permeation across bilayers composed of phospholipids with different head groups and fatty acyl chains. *Biophys. J.* 68:997-1008.

Joós, B., Z. Zhou, M. S. Duesbery. 1994. Dislocation mediated healing of ideal and adsorbed monolayers with vacancy damage. *Phys. Rev. B.* 50:8763-8772.

Josefowicz, J. Y., N. C. Maliszewskyj, S. H. J. Idziak, P. A. Heiney, J. P. McCauley, Jr., A. B. Smith III. 1993. Structure of Langmuir-Blodgett films of disk-shaped molecules determined by atomic force microscopy. *Science.* 260:323-326.

Kaneko, E. (Editor). 1987. Liquid crystal TV displays: principles and applications of liquid crystal displays. Scientific Publisher, Tokyo.

Kantor, Y., M. Kardar, D. R. Nelson. 1986. Statistical mechanics of tethered surfaces. *Phys. Rev. Lett.* 57:791-794.

Kantor, Y., D. R. Nelson. 1987. Crumpling transition in polymerised membranes. *Phys. Rev. Lett.* 58:2774-2777.

Kas, J., E. Sackmann. 1991. Shape transitions and shape stability of giant phospholipid vesicles in pure water induced by area-to-volume changes. *Biophys. J.* 60:825-844.

Kashchiev, D., D. Exerowa. 1983. Bilayer lipid membrane permeation and rupture due to hole formation. *Biochim. Biophys. Acta.* 732:133-145.

Kelker, H. 1973. History of liquid crystals. *Mol. Cryst. Liq. Cryst.* 21:1-48.

Landau, L. D., E. M. Lifshitz. 1959. Theory of elasticity. Pergamon Press, Addison-Wesley Publishing Co. Inc., Reading, Massuchussetts.

Lasic, D. D. 1992. Mixed micelles in drug delivery. *Nature*. 355:279-280.

Lebwohl, P. A., G. Lasher. 1972. Nematic liquid crystal order-a Monte Carlo simulation. *Phys. Rev. A*. 6:426-429.

Lee, R. C., L. P. River, F-S. Pan, L. Ji, R. L. Wollmann. 1992. Surfactant-induced sealing of electropermeabilised skeletal muscle membranes *in vivo*. *Proc. Natl. Acad. Sci. USA*. 89:4524-4528.

Lee, R. C., A. Myerov, C. P. Maloney. 1994. Promising therapy for cell membrane damage. *Annals of the New York Academy of Sciences*. 720:239-245.

Leibler, S., R. R. P. Singh, M. E. Fisher. 1987. Thermodynamic behaviour of two-dimensional vesicles. *Phys. Rev. Lett*. 59:1989-1992.

Leibler, S. 1989. In Statistical mechanics of membranes and surfaces. Proceedings of the Jerusalem winter school for theoretical physics. Edited by D. R. Nelson, T. Piran, and S. Weinberg. World Scientific, Singapore.

Lekkerkerker, H. N. W. 1991. Ordering in supra-molecular fluids. *Physica A*. 176:1-15.

Levelut, A. M., 1979. Structure of a disk-like mesophase. *J. de Phys. Lett*. 40:L81-L84.

Lipowsky, R., M. Girardet. 1990. Shape fluctuations of polymerised or fluidlike membranes. *Phys. Rev. Lett*. 65:2893-2896.

Lipowsky, R. 1991. The conformation of membranes. *Nature*. 349:475-481.

Litster, J. D. 1975. Stability of lipid bilayers and red blood cell membranes. *Phys. Lett. A*. 53:193-194.

Litzinger, D. C., L. Huang. 1992. Phosphatidylethanolamine liposomes: drug delivery, gene transfer and immunodiagnostic applications. *Biochim. Biophys. Acta*. 1113:201-227.

Luckhurst, G. R., G. W. Gray. 1979. Molecular physics of liquid crystals. Academic Press, London.

McKenzie, D. S. 1976. Polymers and scaling. *Physics Reports*. 27:35-88.

Metropolis, N., A. W. Rosenbluth, M. N. Rosenbluth, A. H. Teller. 1953. Equation of state calculations by fast computing machines. *J. Chem. Phys*. 21:1087-1092.

Miyamoto, S., T. Maeda, S. Fujime. 1988. Change in membrane elastic modulus on activation of glucose transport system of brush border membrane vesicles studied by osmotic swelling and dynamic light scattering. *Biophys. J*. 53:505-512.

Mui, B. L-S., P. R. Cullis, E. A. Evans, T. D. Madden. 1993. Osmotic properties of large unilamellar vesicles prepared by extrusion. *Biophys. J*. 64:443-453.

Nanavati, C., V. S. Martin, A. F. Oberhauser, J. M. Fernandez. 1992. The exocytotic fusion pore modeled as a lipidic pore. *Biophys. J.* 63:1118-1132.

Needham, D., R. M. Hochmuth. 1989. Electro-mechanical permeabilisation of lipid vesicles. *Biophys. J.* 55:1001-1009.

Nelson, D. R., L. Peliti. 1987. Fluctuations in membranes with crystalline and hexatic order. *J. de Phys. (Paris).* 48:1085-1092.

Nelson, D., T. Piran, S. Weinberg. 1989. Statistical Mechanics of membranes and surfaces. World Scientific Publishing Co. Pte. Ltd., Singapore.

Nienhuis, B. 1982. Exact critical point and critical exponents of O(n) models in two dimensions. *Phys. Rev. Lett.* 49:1062-1065.

Onsager, L. 1949. *Annals of the New York Academy of Sciences.* 51:627.

Plischke, M., D. H. Boal. 1988. Absence of a crumpling transition in strongly self-avoiding tethered membranes. *Phys. Rev. A.* 38:4943-4945.

Popescu, D., C. Rucareanu. 1991. A model for the appearance of statistical pores in membranes due to selfoscillations. *Bioelectrochem. Bioenerg.* 25:91-103.

Powell, K. T., J. C. Weaver. 1986. Transient aqueous pores in bilayer membranes: A statistical theory. *Bioelectrochem. Bioenerg.* 15:211-227.

Rutkowski, C. A., L. M. Williams, T. H. Haines, H. Z. Cummins. 1991. The elasticity of synthetic phospholipid vesicles obtained by photon correlation spectroscopy. *Biochemistry.* 30:5688-5696.

Sackmann, E. 1990. Molecular and global structure and dynamics of membranes and lipid bilayers. *Can. J. Phys.* 68:999-1012.

Schreiner, W., K. W. Kratky. 1983. Influence of box shape on the hard-disk pressure at high fluid density. *Chemical Physics.* 80:245-251.

Somoza, A. M., P. Tarazona. 1990. Nematic and smectic liquid crystals of hard spherocylinders. *Phys. Rev. A.* 41:965-970.

Steck, T. 1989. In Cell Shape: Determinants, Regulation and Regulatory Role. W. Stein and F. Bronner, editors. Academic Press Inc., New York.

Stroobants, A., H. N. W. Lekkerkerker, D. Frenkel. 1987. Evidence for one-, two-, and three-dimensional order in a system of hard parallel spherocylinders. *Phys. Rev. A.* 36:2929-2945.

Tanford, C. 1979. Hydrostatic pressure in small phospholipid vesicles. *Proc. Natl. Acad. Sci. USA.* 76:3318-3319.

Tang, W., M. F. Thorpe. 1988. Percolation of elastic networks under tension. *Phys. Rev. B.* 37:5539-5551.

Taupin, C., M. Dvolaitzky, C. Sauterey. 1975. Osmotic pressure induced pores in phospholipid vesicles. *Biochemistry.* 14:4771-4775.

Thorpe, M. F., E. J. Garboczi. 1990. Elastic properties of central-force networks with bond-length mismatch. *Phys. Rev. B.* 42:8405-8417.

Tinh, Nguyen Huu, C. Destrade, H. Gasparoux. 1979. Nematic disc-like liquid crystals. *Phys. Lett. A.* 72:251-254.

Veerman, J. A. C., D. Frenkel. 1990. Phase diagram of a system of hard spherocylinders by computer simulation. *Phys. Rev. A.* 41:3237-3244.

Veerman, J. A. C., D. Frenkel. 1991. Relative stability of columnar and crystalline phases in a system of parallel hard spherocylinders. *Phys. Rev. A.* 43:4334-4342.

Veerman, J. A. C., D. Frenkel. 1992. Phase behaviour of disklike hard-core mesogens. *Phys. Rev. A.* 45:5632-5648.

Vertessy, B., T. L. Steck. 1989. Elasticity of the human red cell membrane skeleton. *Biophys. J.* 55:255-262.

Vieillard-Baron, J. 1974. The equation of state of a system of hard spherocylinders. *Mol. Phys.* 28:809-818.

Weaver, J. C. 1994. Molecular basis for cell membrane electroporation. *Annals of the New York Academy of Sciences.* 720:141-152.

Wesemann, J., L. Qin, P. Siders. 1989. Orientational ordering in a monolayer of hard oblate spheroids. *Langmuir.* 5:1358-1363.

Wilhelm, C., M. Winterhalter, U. Zimmermann, R. Benz. 1993. Kinetics of pore size during irreversible electrical breakdown of lipid bilayer membranes. *Biophys. J.* 64:121-128.

Wojcik, M., K. E. Gubbins. 1984. Thermodynamics and structure of hard oblate spherocylinder fluids. *Mol. Phys.* 53:397-420.

Wood, W. W. 1968. Monte Carlo calculations for hard disks in the isothermal-isobaric ensemble. *J. Chem. Phys.* 48:415-434.

Zarragoicoechea, G. J., D. Levesque, J. J. Weis. 1993. Monte Carlo simulations of polar discotic molecules. *Mol. Phys.* 78:1475-1492.

Zhelev, D. V., D. Needham. 1993. Tension-stabilized pores in giant vesicles: determination of pore size and pore line tension. *Biochim. Biophys. Acta.* 1147:89-104.

Zwanzig, R. 1963. First-order phase transition in a gas of long thin rods. *J. Chem. Phys.* 39:1714-1721.